PLASTIC DEFORMATION AND EFFECTIVE STRAIN HARDENING

COEFFICIENT OF IRRADIATED Fe-9WT%Cr ODS ALLOY BY NANO-

INDENTATION AND TEM

by

Corey Kenneth Dolph

A thesis

submitted in partial fulfillment

of the requirements for the degree of

Master of Science in Materials Science and Engineering

Boise State University

December 2015

BOISE STATE UNIVERSITY GRADUATE COLLEGE

DEFENSE COMMITTEE AND FINAL READING APPROVALS

of the thesis submitted by

Corey Kenneth Dolph

Thesis Title: Plastic Deformation and Effective Strain Hardening Coefficient of Irradiated Fe-9wt%Cr ODS Alloy by Nano-Indentation and TEM

Date of Final Oral Examination: 11 August 2015

The following individuals read and discussed the thesis submitted by student Corey Kenneth Dolph, and they evaluated his presentation and response to questions during the final oral examination. They found that the student passed the final oral examination.

Janelle Wharry, Ph.D.	Chair, Supervisory Committee
Richard Wright, Ph.D.	Member, Supervisory Committee
Yaqiao Wu, Ph.D.	Member, Supervisory Committee

The final reading approval of the thesis was granted by Janelle Wharry, Ph.D., Chair of the Supervisory Committee. The thesis was approved for the Graduate College by John R. Pelton, Ph.D., Dean of the Graduate College.

DEDICATION

For my son, Harrison. May a desire to understand lead you on a path of discovery.

ACKNOWLEDGEMENTS

A final, but special thanks goes to my family. Without the love and support of my wife, Christine, I have no idea where I would be or what I would be doing. I only know that it wouldn't be as productive, as fulfilling, or as much fun. To my parents, though my life has led down multiple paths, you have always loved and supported me. Without that support I would not be the man I am today. Thank you.

ABSTRACT

The objective of this study is to characterize changes in the yielding and effective

strain hardening coefficient of an oxide dispersion strengthened (ODS) alloy upon

exposure to irradiation. It is well known that irradiation produces a supersaturation of

defects, which alters the mechanical properties of a material. In order to engineer

materials for use in advanced nuclear reactors, the long-term effects of neutron irradiation

on mechanical performance must be understood. However, high-dose neutron exposure is

often simulated using ion bombardment. Unfortunately, ion irradiation results in a

shallow damage layer that prevents traditional bulk mechanical characterization methods

from being utilized. A technique with the ability to examine the thin film of irradiated

damage is required to provide insight into the changes in yield stress, elastic modulus,

and hardness. Nano-indentation experiments have thus become a powerful tool to

analyze ion irradiated materials, but a thorough understanding of the plastic deformation

that occurs during nano-indention is required to accurately interpret the results. In this

work, a coupled experimental and modeling approach resulted in an understanding of the

effects of irradiation on strain hardening in a model Fe-9wt%Cr ODS alloy. Nano-

indentation was performed on the alloy before and after irradiation, either with 5.0 MeV

Fe^{++} ions to 100 displacements per atom (dpa) at 400°C or with a fast neutron spectrum

to 3 dpa at 500° C. Nano-hardness measurements reported similar hardening between the

two conditions, which is supported by investigation of the microstructure. The size and

shape of the residual plastic zone beneath nano-indents was characterized using

transmission electron microscopy coupled with Automated Crystal Orientation Mapping

(ACOM-TEM) techniques. A model developed from finite element analysis, using the

spherical indenter approximation, was combined with the experimental results to

calculate the effective strain hardening coefficient that resulted from irradiation induced

defects. Results indicate a 39.2%, and 49.5% increase in strain hardening resulting from

respective ion and neutron irradiation conditions, and a 10.9% between the two

irradiations. The similar hardening yet slight variation in the effective strain hardening

coefficient is thought to be due to the slight difference in the nature of the damage

cascades developed under ion and neutron irradiation.

TABLE OF CONTENTS

LIST OF TABLES

LIST OF FIGURES

LIST OF ABBREVIATIONS

a	lattice parameter, contact radius
$\bar{a}$	indentation diagonal
a/R	indentation strain
A_C	contact area
APT	Atom Probe Tomography
ASTAR	Automatic crystal orientation mapping software from Nano-Megas
ATR	Advanced Test Reactor
AFM	Atomic Force Microscopy
α	conical half angle, or fit constant for Oliver Pharr method
α'	chromium-rich ferrite
b	Burgers vector
BCC	Body Centered Cubic
BCT	Body Centered Tetragonal
β	ratio of plastic zone radius to contact radius
c	plastic zone radius
$CAES$	Center for Advanced Energy Studies
CCT	Continuous Cooling Transformation diagram
C_f	compliance constant
C_X	concentration of X
D_X	diffusion coefficient of X
d	average diameter of obstacle
$d_{Xi,v}$	diffusivity of X through interstitial or vacancy exchange
$DBTT$	Ductile to Brittle Transition Temperature

$\dfrac{dP}{dh}$	contact stiffness
dpa	displacements per atom
E	elastic modulus of the sample, desired margin of error
E'	elastic modulus of the indenter
E^*	combined Elastic modulus
EDM	Electric Discharge Machining
ε_{mis}	misfit strain
ϵ_t	true strain
f	volume fraction
FCC	Face Centered Cubic
FEA	Finite Element Analysis
FIB	Focused Ion Beam
$F\text{-}M$	Ferritic-Martensitic
G	shear modulus
h	indentation depth
h'	adjusted indentation depth
h_c	contact depth
h_e	elastic unloading
h_f	final residual contact depth
h_i	initial depth of penetration
h_{max}	max depth of penetration
h_p	plastic depth
h_s	depth of the edge of the contact area penetrates into the sample at P_{max}
h_t	total indentation depth
H	indentation hardness
H_0	hardness due to statistically stored dislocations
INL	Idaho National Lab
ISE	Indentation Size Effect

IQR	Interquartile Range
K	strength coefficient, true stress at true strain of 0.1
m	fit constant for the Oliver Pharr method
M_F	martensite finish temperature
M_S	martensite start temperature
N	Number density of obstacle
N_X	the atomic fraction of X
n	strain-hardening coefficient, sample size
ODS	Oxide Dispersion-Strengthened
p	pressure
p_{ave}	average contact pressure
P	applied load
P_{max}	max load
PKA	Primary Knock on Atom
Q_1	first quartile
Q_3	third quartile
r	radius
$\boldsymbol{r}$	position of the element at the onset of the distortion
R	radius of spherical indenter
$RAFMs$	Reduced Activation Ferritic Martensitic steels
RIS	Radiation Induced Segregation
$\boldsymbol{\rho}, \rho$	position vector
ρ_s	statistically stored dislocation density
S	contact stiffness
SIA	Self-Interstitial Atom
$SRIM$	Stopping and Range of Ions in Matter
σ	standard deviation
σ_0	resistance to dislocation movement

σ_r	uniaxial stress
σ_t	true stress
σ_θ	circumferential stress
σ_{ys}	yield stress
T_m	melting temperature
TEM	Transmission Electron Microscopy
TMT	Thermo-Mechanical Treatments
TTT	Time-Temperature-Transformation
τ	theoretical strength
τ_{mis}	misfit hardening
UTS	Ultimate Tensile Stress
USE	Upper Shelf Energy
θ	face angle for a Berkovich probe
ν	Poisson's ratio of the sample
ν'	Poisson's ratio of the indenter
χ	gradient of chemical potential
XRD	X-Ray Diffraction
z	the direction from the surface of the sample into the bulk
$z_{\alpha/2}$	critical z score
z_{ys}	depth of plastic zone measured below the center of the indent

CHAPTER ONE: INTRODUCTION

The great challenge of our time is adjusting to the exponential population growth that has seen the number of humans on the planet expand from 1.5 billion to over 7.0 billion in just over the last 100 years [1]. As more and more people demand an ever increasing standard of living, the strain on exiting energy supplies has been the impetus for new and expanded avenues for renewed research into Generation IV nuclear reactors. Advancements in reactor design offer the promise of providing safer, and proliferation-resistant energy more efficiently and over a longer lifespan than existing technologies. The design challenge is that these advancements require operation at higher temperatures, higher doses, and more corrosive environments than current structural materials can endure.

Research has turned towards development of materials that can fulfill four design requirements:

1. Dimensional resistance to thermal and irradiation creep

2. Adequate strength, ductility, and fatigue resistance

3. Resistance to radiation damage such as irradiation hardening and embrittlement with high neutron exposure

4. Chemical stability with the other structural and fuel components.

One of the materials that has been proposed as a candidate material is ferritic martensitic (F-M) steel alloys. Additionally, the increased strength offered in oxide dispersion strengthened F-M alloys has made it a primary or secondary option for structural

components in gas, sodium, or lead cooled fast reactors, and super critical water reactors [2].

In this work irradiation hardening will be investigated in a Fe-9wt%Cr ODS alloy by examining the changes in tensile properties after exposure to a heavy ion or neutron flux. Background information on F-M and ODS alloys, irradiation effects, and nano-indentation is presented in Chapter 2. The third chapter provides a thorough discussion on the objective of this thesis. Chapter 4 offers the experimental techniques used to collect the data that is presented Chapter 5. A discussion of the results, and calculation of strain hardening coefficients are found in Chapter 6. The conclusions of this work make up Chapter 7.

CHAPTER TWO: BACKGROUND

2.1 Properties of Ferritic-Martensitic Steels

Ferritic-Martensitic steels are a leading candidate material being considered for cladding and structural components within the next generation of fission and future fusion reactors, because of their high operating temperatures, high creep rupture strength, weldability, reduced activation, and a long history of manufacturing experience. High chromium steels originated in the 1910's with applications for high temperature boilers, and turbine blades. When it was discovered that the high chromium and low carbon (<0.1%) steels did not rust the applications expanded from petrochemical and chemical processing plants to commercial applications such as knives and razors. In order to appreciate how F-M steels are engineered for nuclear applications, one must understand the basic structure of steel [3].

2.1.1 Phases of Steel

Steel is made by interstitially adding carbon to an iron matrix, with concentration of carbon combined with the processing temperature dictating the phase that is formed, as described by the iron-carbon phase diagram shown in Figure 2.1. The ferrite phase, commonly referred to as α-iron, is formed at low temperatures and low carbon concentrations, which result in a body centered cubic (BCC) structure. By adding more carbon, or processing at medium temperatures, a face centered cubic (FCC) structure known as austenite, or γ-iron, is formed. The delta ferrite phase is a low carbon concentration, and high temperature phase that has a BCC structure and is also known as

δ-iron. When the carbon concentration reaches 6.7 wt% a solid solution of cementite

(Fe_3C) is formed, which is why the iron-carbon phase diagram traditionally shows low

carbon concentrations. Prior to the formation of the solid solution phases, transitional

phases occur made up of combinations between the initial and final structures.

When γ-iron is cooled through the eutectoid at 738° C an α ferrite and cementite

solution is formed, which depending on the rate of cooling can be either pearlite or

bainite. When the solution is slowly cooled a structure with alternating α-iron and

cementite layers known as pearlite is formed. The mechanical properties of pearlite has

fall between ferrite and cementite. If the solution is cooled quicker, then bainite is

formed instead of pearlite, with bainite having a finer microstructure, due to the limited

diffusion that occurs, resulting in a stronger, yet less ductile material. The cooling rates

required for the formation of pearlite and bainite are described in the time-temperature-

transformation (TTT) diagram shown in Figure 2.2, which also shows how the martensite

phase of steel can be produced.

The rate of quenching of austenite required for the formation of martensite is so

rapid that it is considered a diffusionless process, where the atoms in the FCC structure of

γ-iron quickly shift to body-centered tetragonal (BCT) positions, resulting in a non-

equilibrium condition, where the carbon atoms take up interstitial locations as shown in

Figure 2.3. The high activation energies required for diffusion makes the martensitic

phase stable even at elevated temperatures, and the low number of slip systems for BCT

geometries cause martensite to be the hardest phase of steel. Untreated martensite is

often too brittle be used for many engineering applications, because the volume

expansion that accompanies the FCC to BCT transition results in a large internal stress

field. To prevent this, martensite is tempered below 650°C, allowing the internal stresses

to be relieved by the formation of cementite phases. The final microstructure consists of

small uniformly distributed cementite phases that are within an α-iron matrix, resulting in

a material that has similar hardness to martensite caused by the small cementite phases,

but increased ductility due to the ferrite phase [4].

2.1.2 Hardening Mechanisms

The theoretical crystal strength for a perfect crystal with no dislocations is given

by:

$$\tau = (G/2\pi) \qquad\qquad \textbf{Equation 2.1 } [5]$$

where τ is the theoretical strength, and G is the shear modulus. The theoretical crystal

strength for iron is 13.2 GPa, but when it is experimentally measured the strength is only

27.5 MPa [5]. The observed reduction of yield strength, by three orders of magnitude, is

a result of the strain fields associated with defects creating localized regions where the

energy required for plastic deformation is reduced by the tensile and compressive fields

that develop when dislocations are present. These fields are shown in Figure 2.4. When

the conditions are kinetically favorable, the defects walk their way through the crystal

lattice, where they interact with the existing strain fields and arrange themselves in a way

that minimizes the energy of the system. This as illustrated in Figure 2.5, which

describes the movement of an tensile strain field associated with an edge dislocation in a

crystal to a region of compressive strain surrounding a larger substitutional defect [4],

[5].

The development of F-M steels for nuclear applications has been driven by the

need for a material with a high creep resistance when at elevated temperatures and in

harsh reactor environments. Creep is the time-dependent deformation that occurs at low stress and high temperatures, with the two low stress mechanisms being Nabarro-Herring creep, and Coble creep. Both are diffusional mechanisms, where Nabarro and Herring theorized that the diffusion of vacancies travel from regions of the grain boundaries in tension to regions in compression, and Coble creep describes the diffusion of atoms or ions along grain boundaries. As the stress level increases and if the temperatures is reaches half of the melting temperature, T_m, then a dislocation limited phenomenon, described by Weertmann, where edge dislocations climb over obstacles resulting in elongation of the material.

In many cases the dislocation creep mechanism is prominent, which allows for increasing the creep resistance of a material by creating obstacles were defects can become pinned. This will lower the creep rate and can be accomplished through a variety of strengthening mechanisms [4], [5].

2.1.2.1 Boundary Strengthening

In polycrystalline materials, neighboring grains are rarely aligned with the same crystal orientations. This makes it difficult for dislocations to pass from one grain to another due to the large energies required to shift the dislocation movement to the corresponding slip plane of the adjacent grain. As the movement of dislocations is restricted the material becomes harder, stronger, and more brittle. The smaller the grain size the more likely a dislocation is to be restricted by a grain boundary, and the effect of grain size on yield strength is described by the Hall-Petch equation:

$$\sigma_y = \sigma_0 + k_y d^{-1/2}$$
Equation 2.2 [4]

where d is the average grain diameter, σ_0 is the overall resistance to dislocation movement, and k_y is the locking parameter for the material. Recent work into nano-crystalline materials have shown increased yield strength with decreasing grain size, but the amount of increase varies from the predicted change in yield strength by the Hall-Petch relationship, suggesting an altered stress relationship as the nano-scale [4], [5]

2.1.2.2 Solution Strengthening

When impurity atoms go into solution as substitutional or interstitial defects, their position is such that the total lattice energy is minimized. The compressive and tensile strain fields associated with defects, shown in Figure 2.4, interact with the localized strain fields produced by the impurity atom. The impurity strain field is either compressive or tensile based on the relative atomic sizes of the solute and solvent atoms. If the impurity atom is smaller than the host atom, then the strain field places the surrounding atoms in tension as the bonds are stretched the extra distance. In order to reduce the energy of the system, the impurity atom will eventually diffuse into a compressive field caused by a dislocation, with the net result being a reduction in the overall stress field. A larger atom would diffuse to a dislocation tensile field, which also reduces the overall stress field, and result in a harder crystal. This final position of a larger impurity atom interacting with an edge dislocation is shown in Figure 2.5 [4].

2.1.2.3 Precipitation Strengthening

Once the solubility limit of the matrix is exceeded by the solute concentration, a second-phase will nucleate out of the material and form precipitates. The presence of these additional phases restrict dislocation motion, with the amount of strengthening that

is experienced being highly dependent on the coherency of the precipitate with the matrix, as measured by the misfit strain, ε_{mis}:

$$\varepsilon_{mis} = (a_{precipitate} - a_{lattice})/a_{lattice}$$

<div align="right">**Equation 2.3** [5]</div>

with a being the lattice parameter. In coherent precipitates the structure of the obstacle is similar to that of the matrix, allowing dislocations to cut through the particle under an applied shear stress. A diagram of this condition is shown in Figure 2.7. The resistance the dislocation experiences as it passes through the precipitate hardens the materials as such:

$$\tau_{mis} \propto G\varepsilon_{mis}^{\frac{3}{2}}(rf)^{1/2}$$

<div align="right">**Equation 2.4** [5]</div>

where τ misfit hardening, G is the shear modulus, r is the radius, and f is the volume fraction of the precipitates within the matrix. In this case, the newly created interfacial energy is small, and contributes little strengthening to the alloy. However, if this occurs when the precipitates have an ordered lattice structure, the interfacial energy is accompanied by the formation of an antiphase domain boundary. The additional energy required to overcome the antiphase domain boundary results in additional strengthening described by:

$$\tau_{mis} \propto \gamma^{3/2} \left(\frac{rf}{G}\right)^{1/2}$$

<div align="right">**Equation 2.5** [5]</div>

where γ is the antiphase domain boundary energy. The combined effect of Equation 2.4 and Equation 2.5 results in a significant hardening observed in alloys containing ordered precipitates

In the case of incoherent precipitates, or a large distance between precipitates, the dislocations are unable to cut through and instead they are forced to bow around the obstacle until the stored energy is enough to break apart the two ends of the dislocation line. The end result is an Orowan loop remaining around the precipitate, with the two newly formed ends of the dislocation line re-combining to create a single dislocation on the other side. This process, shown in Figure 2.8, slows the movement of dislocations, much more than cutting through a coherent precipitate, limiting the deformation [5].

2.1.2.4 Dispersion Strengthening

When designing materials for use at elevated temperatures, or when working with materials that do not precipitate phases that are thermodynamically stable, strengthening can be accomplished by mechanically adding small particles into the matrix during processing. Al_2O_3, TiO_2, and Y_2O_3 are all common oxides that are added to strengthen metal alloys when they operate near their melting temperatures. When these particles are uniformly dispersed in the matrix, as depicted in Figure 2.9, they obstruct dislocation motion in the same way that a precipitate grown out of solid solution would. In addition they also prevent larger grain growth by restricting recrystallization, preventing a reduction in strength as described by the Hall-Petch relationship.

These materials can be difficult to process due to the additional steps required for uniform particle size and homogeneous dispersion, and the amount of strengthening achieved for each dispersion is less than that achieved by other mechanisms. However, the high operating temperature of next generation nuclear reactors is an impetus for oxide dispersion strengthened (ODS) steels being considered as a material for reactor

components, where the majority contributor of the strength of the alloy is provided by the presence of a network of evenly distributed oxide particles [5], [6].

<u>2.1.2.5 Strain Hardening</u>

When a material is plastically deformed the number of dislocations increase, and are more likely to interact with each other either through attraction or repulsion, depending on the orientation of the individual strain fields. If the dislocations attract one another they will annihilate. If they repel one another, then they hinder each other's movements, and on average the dislocation interactions are repulsive, resulting in materials with large the dislocation densities being strengthened .

The stress vs. strain curve for a single crystal, Figure 2.10, demonstrates how work hardening progresses through three distinct stages for a given material. In Region I the strain hardening rate (slope) is low due to the limited interactions of low density dislocations. Once a uniform dislocation distribution is developed Region II begins, and dislocation pile up occurs causing a large increase in the strain hardening rate. Eventually the applied stress is so large that the dislocation interactions are easily overcome, which results in the lower strain hardening rate of Region III. This process is known as strain hardening, cold working, or work hardening, and can be represented as percent cold work (%CW) where A_0 is the original area and A_d is the area after plastic deformation [4].

$$\% \, CW = \left(\frac{A_0 - A_d}{A_0} \right) \times 100 \qquad \textbf{Equation 2.6} \, [4]$$

This phenomenon can be represented as a stress strain curve for a material, where after the initial elastic deformation there is an increase in material strength with increasing strain. The shape of this curve can be described by a single equation developed by Hollomon:

$$\sigma_t = K\epsilon_t{}^n \hspace{4cm} \textbf{Equation 2.7} [7]$$

where σ_t is the true stress, ϵ_t is the true strain, K is a strength coefficient that is defined to be the true stress at a true strain of 1.0, and n is the strain-hardening coefficient which has a value between 0.1 and 0.5 for most metals. It has also been shown that the UTS occurs when the true strain is equal to the strain-hardening coefficient, necking will onset when the slope of the stress strain curve is equal to the true stress, and that the Hollomon model is most accurate for metals that have a strain-hardening coefficient between 0.1 and 0.3 [5], [7], [8].

2.1.3 Ferritic-Martensitic Steels

The history of ferritic-martensitic (F-M) steels begins in 1912 with the first reported use of high chromium (Cr) steel being a 12wt% Cr and 2-5wt% Mo steel blade developed for use in steam turbines. The following year 'stainless steel' was developed when it was noticed that steels containing 13wt% Cr and 0.2wt% C did not rust, with the applications originally being as cutting edges due to the ability of the martensite to hold an edge. Although high Cr steels began being used in industry in the 1930's, it was not until the jet age that a material with a high corrosion resistance, and a high operating temperature was required for use. This led to the development of high Cr steels with enhanced UTS, and creep rupture strength at temperatures of 550°C, and a desire to reduce both air pollution and operation costs of energy production in the 1990's pushed the development of a steel with a creep rupture strength of 100 MPa at 10^5 hours while operating at 600° C [3].

2.1.3.1 Processing

Depending on the processing techniques, and alloying concentrations utilized, high Cr steels can be fully martensite, martensite and ferrite, martensite and austenite, or a combination of all three phases. Prior to quenching, a fully austenitic structure, or a combined austenite and δ-ferrite structure is engineered using a combination of alloy additions and heat treatments. In 12wt% Cr steels the alloying elements C, N, Ni, Mn, Cu, and Co promote the growth the austenite phase, while Cr, Mo, Nb, V, W, Si, Ti, and Al stabilize ferrite grains [3]. Chromium also promotes the formation of the ferrite phase, and if the concentration is too high then austenite will not precipitate out, and the concentration of martensite will be limited [9].

Which elements are used depends on desired mechanical properties, and the type of operating environment the material will be exposed to [3]. A study by K. Hashimoto et al in 1983, found that for operation at high temperatures stabilizing elements should be added to replace carbon, and limit the carbide growth. As the carbides get larger, the precipitation hardening effect lowers as the precipitates coalesce into larger features, and strengthening elements are striped out of solid solution, removing some of the solid solution hardening. It was recommended that the concentration of carbon be less than 0.2wt% [10]. Abe, Araki, and Noda in 1991, and Shikakura et al in 1991 looked into the effect the W has on the final alloy, and found that it slows the recrystallization rate, and added to the long term thermal stability of the $M_{23}C_6$ precipitates that form during the tempering treatment [11], [12]. The mechanical effects are not always the most important factor in determining which elements to use. For example, although nickel is

an austenite forming element it doesn't provide as much strengthening as carbon, but

nickel is the preferred choice in nuclear applications as it is more difficult to activate [3].

As the combination of alloying elements is altered it is possible to predict the final

phases that will be present based on nickel and chromium equivalents. Equation 2.8 and

Equation 2.9 are valid for 12wt% Cr alloys, and are used along with a Schaeffler-

Schneider diagram, shown in Figure 2.11, to predict the microstructure that will result

post processing.

$$Ni_{equivalent}(wt\%)$$

Equation 2.8 [3]

$$= (\%Ni) + (\%Co) + 0.5(\%Mn)$$

$$+ 0.3(\%Cu) + 30(\%C) + 25\ (\%N)$$

$$Cr_{equivalent}(wt\%)$$

Equation 2.9 [3]

$$= (\%Cr) + 2(\%Si) + 1.5(\%Mo)$$

$$+ 5(\%V) + 1.75\ (\%Nb) + 0.75(\%W)$$

$$+ 1.5(\%Ti) + 5.5(\%Al) + 1.2(\%Ta)$$

$$+ 1.2(\%Hf) + 1.0(\%\ Ce) + 0.8(\%Zr)$$

$$+ 1.2(\%Ge)$$

Relationships like these are verified against experimental results, and similar

equations are developed for each type of material, with the relationships for a 9wt% Cr

steel being found in *High-Chromium Ferritic and Martensitic Steels for Nuclear*

Applications, by Klueh and Harries.

Although these are powerful tools, in actuality the percentage of austenite that

transforms to martensite during cooling depends not only on the on the alloying elements,

but also on the processing time and temperatures. Two temperatures of interest for high

chromium steels are the martensite start, M_S, and martensite finish, M_F, temperatures. Both of these temperatures are lowered by the addition of alloying components, and can prevent a full martensite conversion, leaving residual austenite in the matrix that increases toughness while reducing hardness. The martensite start temperature can be estimated as:

$$M_S(°C) = 635 - 474[(\%C) + 0.86(\%N)$$

Equation 2.10 [3]

$$- 0.15(\%Nb + \%Zr))$$

$$- 0.066(\%Ta + \%Hf)] - 17(\%Cr)$$

$$+ 33(\%Mn) + 21(\%Mo) + 17(\%Ni)$$

$$+ 39(\%V) + 11(\%W)$$

The rapid quenching process associated with F-M steels results in low carbon martensite laths whose hardness is a strong function of the carbon and nitrogen content. Prior to tempering, a double austenitizing treatment is applied to create uniformity between the prior austenite grains and the martensite structure, increasing the creep rupture strength.

To reduce brittleness, a tempering step is preformed below the α-iron to γ-iron transition temperature, which is altered by the alloying elements present, to prevent reaustenitization of the material. Table 2.1 shows the effect of different alloying elements on the transition temperature, with the ferrite to austenite transition temperature ranging from 870° to 960°C for reduced activation steels. The evolution of the microstructure throughout the tempering process is as follows:

- When T <350°C the M_3C (Fe_3C) precipitates form and grow using a branching dendritc structure to Widmanstätten ribbons. The precipitates

become chromium enriched, and M_7C_3 can form. The growth of these precipitates slows the rate of tempering.

- When $T \approx 450° - 500°C$ the Cr_2CN (M_2X) needles begin to form on dislocations in the martensitic laths, which slows the rate of tempering.

- When T is between 500° and 550°C the precipitates grow in size, resulting a drastic softening effect.

- When $T > 550°C$ the M_7C_3 and M_2X precipitates transform to $M_{23}C_6$ precipitates which are rich in chromium. This slows the rate of softening, and results in a reduction in dislocation density in the quenched martensite.

- When $T \geq 650°C$ the $M_{23}C_6$ precipitates found at the martensite lath boundaries coarsen.

- When $T \geq 750°C$, the grains within the martensitic laths become equal subgrains that may still have dislocations present. The $M_{23}C_6$ precipitates have removed the majority of carbon from solution as they continue to grow.

The rate of growth of the M_3C, M_2X, M_7C_3, and ultimately the $M_{23}C_6$ precipitates is heavily influenced by the alloying element concentration. Low concentrations of nitrogen, 0.02 to 0.03%, results in the preferential growth of Cr_2N (M_2X) over M_7C_3, which initially increases secondary hardening and overaged hardness by leaving higher concentrations of carbon in the matrix that drives the formation of additional precipitates, and raising the volume fraction of precipitates, which increases the overall hardening. Nickel accelerates precipitate growth, which lowers the tempering resistance [3], [13].

The final structure of both reduced activation and conventional high chromium martensitic steels contain martensitic laths with dislocations characterized with a Burgers vector of $1/2a_0<111>$, and $M_{23}C_6$ precipitates found both on prior austenite/ferrite grain boundaries, and within the martensite laths. The precipitates within the lath structure are finer than the precipitates found on the grain boundaries. M_2X precipitates are also found within the martensite laths. This structure is shown in Figure 2.12 [3].

2.1.3.2 Effect of Chromium on Material Properties

The measured hardness, yield strength, and UTS in F-M steels trend with the chromium concentration within the alloy. As more chromium is added in solid solution, increased hardness is observed, with additional hardening observed if other solid solution strengthening alloys such as tungsten have been added [13]. Similar trends with the yield strength and UTS have been reported for F-M steels that have evolved to have higher creep-rupture strengths such as: T9, T91, HT9, HCM12, and HCM12A steels, which have chromium contents of 9wt%, 9wt%, 12wt%, 12wt%, and 12wt%, respectively. The mechanical properties are observed to reduce in magnitude as the testing temperature increases [13], [14]. The processing differences for the above mentioned steels are shown in Figure 2.13.

2.1.4 Oxide Dispersion-Strengthened Steel

Future fission and fusion reactors will have high operating temperatures to reach high operational efficiencies. The application of reduced activation ferritic martensitic steels (RAFMs) at temperatures greater than 823K is prevented due to the deterioration of the tensile characteristics that make these materials a popular candidate for cladding and support materials [3], [15], [16]. In an effort to extend the operating window for RAFMs,

engineers turned to an idea from the 1960's where oxide particles of yttrium, titanium, and oxygen were mechanically dispersed within the matrix of the steel to strengthen the alloy (see Section 2.1.2.4). The first generation of oxide dispersion-strengthened (ODS) steels were plagued with anisotropic dispersion of the oxides and poor fracture toughness that prevented their use in the current fleet of operational reactors [14], [16]. Recent advances in alloying chemistry and the addition of thermo-mechanical treatments (TMT) have allowed the development of an ODS alloy with isotropic properties and improved fracture toughness in high and medium chromium content alloys. The diameter of the oxide has also been reduced to tens of nano-meters to provide additional strengthening, as shown using Atom Probe Tomography (APT) in Figure 2.14 [3], [17].

2.1.4.1 Processing

The components for ODS alloys, including the Y_2O_3 powder, are prepared using a planetary ball mill, for 48 – 60 h, in an inert atmosphere to mechanically mix and fine the high purity, 99.5% – 99.9%, process powders. Once all the powders have a uniform particle size distribution, promoting a homogeneous structure, they are sealed in a stainless steel can and degassed under vacuum to prevent oxidation. The alloy is then forged using either hot extrusion or hot isostatic pressing to consolidate the powders. Finally a tempering heat treatment is applied to reduce the internal stresses, and the sample is allowed to air cool [15]–[20]. The final phases present are determined based on the iron-chromium phase diagram, shown in Figure 2.15, and the CCT diagram shown in Figure 2.16.

The non-uniform oxide dispersion is addressed in medium chromium content ODS alloys, 9 to 11wt% Cr, by replacing the molybdenum with tungsten additions and

limiting the concentrations of titanium and oxygen, which promotes the homogenous dispersion of the oxides as $Y_2Ti_2O_7$ for larger oxides and a non-stoichiometric cluster of Y-Ti-O for oxides approximately less than 17nm [9], [21]. Tungsten also has the added benefit of producing less active fission daughters following neutron absorption. This aids in making the ODS steel a reduced activation alloy. The tungsten addition does not result in an homogeneous microstructure in higher chromium content alloys, and a separate approach is required to take advantage of the higher creep rupture strengths associated with ODS alloys containing greater than 12wt% Cr [3].

Forging the alloy affects the anisotropy of the crystal structure, with hot extrusion adding directionality to the grains while hot isostatic pressing creates a uniform grain distribution [16]–[19], [22], [23]. After the tempering step thermo-mechanical treatments (TMT) are performed to work harden, adjust grain size, or add increased fracture toughness to the material. The poor ductility and fracture toughness associated with high Cr ODS alloys comes from their tendency to intergranularly crack at high temperature [16]. The grain boundary bonding can be strengthened with the addition of low temperature TMTs that promote inter-diffusion through the grain boundaries while not coarsening the microstructure. Processes such as hot pressing, hot rolling, or hydrostatic extrusion have been shown to increase the upper shelf energy and improve the brittle to ductile transition temperature [16], [17].

2.1.4.2 Mechanical Properties

Studies by Li et al. in 2011 and Toualbi et al. in 2012 confirm that introducing fine oxide particles into RAFMs increases the hardness, yield strength, and ultimate tensile strength (UTS), as well as improving the high temperature creep properties of the

alloys. Across all temperatures an increase in the UTS and yield strength between 1.5x and 2.0x was observed, which supported the similar increase in hardness measured using Vickers indentation [15], [22]. This increase in strength was accompanied by only a slight decrease in ductility, as measured through total elongation, suggesting that a higher stress limit is possible. It is also noted that the UTS and yield strengths reported for CLAM and JLF-1 RAFMs at their operational limit of approximately 823K are similar to the UTS and yield strength of the ODS around 923K, suggesting an increased operating temperature. A higher limit for operating temperature was also predicted based on creep studies that found a temperature increase of approximately 100K resulted in the ODS having a similar creep rupture strength as traditional RAFMs [15].

The application of ODS has been limited due to its low fracture toughness at high temperatures, which is approximately one-third to one-fifth of that for traditional RAFMs. However, the additional processing step of hot rolling after the forging of the alloy has been shown to improve the high temperature fracture toughness to the same value as that found in HT9 [16], [17]. In addition to increasing the fracture toughness, the hot rolling step reduces grain size, raising the yield strength and UTS of the alloy, but reducing ductility due to the increased dislocation density associated with the microstructure [17].

2.2 Irradiation Effects

Materials designed for use in the high damage and high temperature environment found in advanced fission and fusion reactors must be mechanically stable under those conditions. Constant bombardment by high energy neutrons creates damage cascades within the material, or regions characterized by interstitial and vacancy defect clusters, as

shown in Figure 2.17. This departure from thermodynamic equilibrium generates chemical potential gradients that act as the impetus for irradiation induced hardening and embrittlement.

In the initial stage an energetic incident particle interacts with a lattice atom, and if enough kinetic energy is transferred, the lattice atom is knocked out of its position, becoming the primary knock on atom, PKA. The transferred kinetic energy causes the PKA to travel through the lattice where it elastically and coulombicly interacts with other atoms forming additional knock on atoms. If their initial energy is greater than 20 keV, these knock on atoms create sub cascades enlarging the depletion zone. This process continues until all the atoms have exhausted enough kinetic energy to where they no longer can displace lattice atoms, and come to rest at interstitial locations within the matrix. These displaced atoms are still too energetic to become stable defects, and their vibrational interactions create a thermal spike capable of generating a localized region of molten material. The thermal energy is dampened by interactions with the surrounding atoms, and stable point defect clusters are formed as the molten zone cools. Defect clusters form via one of two mechanisms, where areas of high defect density arising from the ballistic collisions allow interstitials or vacancies to combine as they cool, or diffusion clustering is promoted by the localized thermal spike. The entire process from formation of PKA to stable defect cluster occurs within 10^{-11} seconds of the original collision. The majority of newly created interstitials and vacancies will recombine and never nucleate to form clusters, but the clusters that do form give rise to the irradiation induced phenomenon described below [24]–[26].

2.2.1 Radiation Induced Segregation (RIS)

At high temperatures the irradiation induced vacancy and interstitial defects random walk through the matrix toward defect sinks such as: grain boundaries, interfaces, dislocation loops, and voids creating areas that are relatively enhanced in some alloying elements and depleted in others [3], [24]. Figure 2.18 describes the concentration gradients that develop in a binary alloy due to this radiation induced segregation, or RIS. As vacancies migrate towards a defect sink, a balancing flow of atoms develops in the opposite direction. If one of the elements is more likely to switch locations with a vacancy, based on the solute-point defect binding energies, then that element will have a higher rate of depletion at the boundary. This process is known as the inverse Kirkendall mechanism [3].

The removal of atoms from the sink, due to vacancy exchange, is countered by the arriving interstitial flux, which is unique for each alloying element. The undersized elements have an easier time diffusing through the alloy, and thus make up a larger percentage of the total interstitial flux. The inverse Kirkendall mechanism and interstitial fluxes describe the overall concentration changes found at defect sinks for the specific elements within the material as:

$$\Delta C_A = \frac{N_A N_B d_{Bi} d_{Ai}}{\chi(d_{Bi} N_B D_A + d_{Ai} N_A D_B)} \left(\frac{d_{Av}}{d_{Bv}} - \frac{d_{Ai}}{d_{Bi}} \right) \Delta C_v \qquad \textbf{Equation 2.11 } [24]$$

where C_X is the concentration of element X, N_X is the atom fraction of X, $d_{Xi,v}$ is the diffusivity of X through interstitial flux or vacancy exchange respectively, D_X is the diffusion coefficient of X, and χ describes the chemical potential gradient within the binary alloy. The bracketed second term in Equation 2.11 determines if the species will become enriched or depleted at defect sinks. When it is positive depletion is predicted, as

the rate of gain through interstitials is smaller than the loss rate through vacancy exchange. If the opposite is true, the area will become enriched [24].

The inverse Kirkendall model has been shown to accurately describe RIS in austenitic alloys where the contributions from the vacancy flux dominate the interstitial flux contributions at all temperatures [27]–[29], but until recently the RIS mechanism in F-M alloys has been less understood. Early experiments into the Cr behavior in F-M steels contradicted each other over whether or not enrichment or depletion was observed at defect sinks [30]–[39]. Recent systematic studies have shown light on the subject by demonstrating that the RIS behavior of the alloying species, particularly of Cr, depends on the irradiation temperature, bulk Cr concentration, and grain boundary orientation [40].

In the BCC system Cr is the fastest diffusing element via both vacancy and interstitial transport, causing RIS to be a more complicated balance of the two mechanisms [41]–[43]. At low temperatures the interstitials diffuse easier through the matrix, resulting in Cr enrichment at grain boundaries, while at high temperatures vacancy diffusion begins to dominate, and Cr depletion is observed. Another factor is that the migration energy for self-interstitial atoms (SIA) in iron decreases as the Cr concentration increases. Therefore a larger percent of the interstitials flowing toward defect sinks are Fe. This limits the amount of Cr interstitials diffusing towards the grain boundary, and restricts the level of Cr enrichment in higher Cr alloys. This dependence has not been observed in Fe-Cr model alloys, which implies the minor alloying elements play a role in the RIS mechanism for Cr by adjusting the relative size of the Cr atoms in solution [32], [36], [40], [44], [45]. The orientation of the boundaries determines the

effectiveness of the local defect to act as a prefect sink, with higher misorientation angles resulting in increased Cr enrichment due to the high degree of order limiting the rate of defect absorption in low angle grain boundaries [40], [46], [47].

2.2.2 Irradiation Induced Precipitates

Radiation induced segregation creates deviations from thermodynamic equilibrium within the damage cascade, which drives the formation and growth of precipitates within the alloy [40]. As a solute becomes enriched at a sink, the concentration can exceed the solubility limit causing a new phase to precipitate out of solution. This enrichment can be caused by the collection of undersized solute atoms at grain boundaries and dislocation loops, or the depletion of the oversized atoms leaving a higher localized concentration [24]. At higher temperatures and irradiation doses radiation induced precipitates with a similar crystallographic structure to the matrix exhibit increased stability [38].

The precipitates that form in F-M steels are Cr-rich ferrite ($\alpha^{'}$), M_6X (η), Chi (χ), G, Laves, Sigma (σ), M_3P, and MP where M can be a number of alloying components, and X is either C or Ni [3], [40], [48]. $\alpha^{'}$ is a BCC phase that has been observed to nucleate in alloys ranging from 6wt.% to greater than 14wt.% Cr, with the kinetics describing nucleation and growth determined by concentration, temperature, and dose [24], [49]–[51]. Alloys with a large concentration of $\alpha^{'}$ suffer from increased embrittlement at high temperatures. M_6X is a diamond cubic precipitate that has been observed to grow out of the $M_{23}C_6$ or M_2X precipitates in tempered F-M alloys with >0.3wt% Ni, either from thermal aging or under irradiation. It is enriched in silicon, chromium, nickel, and phosphorous [3], [52]. The χ phase is a BCC structure that is rich

in iron, silicon, nickel, molybdenum, and phosphorus. It is found in high chromium

steels that are irradiated to high dpa when there are high concentrations of molybdenum

[3]. The G phase is a FCC silicide that begin as nickel, silicon, and manganese clusters at

low dosage [3], [40]. Laves phases, of the form $Fe_2(Mo,Nb)$, nucleate and grow in F-M

steels when exposed to the high process temperatures during thermal aging, and will

homogeneously develop within the grain structure when alloys are exposed to irradiation

over 650° C [3], [38], [40]. Neklyudov and Voyevodin reported that at high doses, ~150

dpa, the Laves phases will begin to dissolve at rates proportional to temperature [38].

The M_3P phase is a phase transformation that typically requires a temperature above 750°

C under normal conditions, but occurs at lower temperatures during irradiation due to the

lower activation energy required for diffusion [48]. The σ, and MP are minor phases that

have been observed in high chromium alloys [3].

2.2.3 Dislocations and Loops

At irradiation temperatures, $T<0.3T_m$, interstitials are more mobile than vacancies,

and the interstitial defects created within a damage cascade form clusters, most of which

are mobile, that interact with other defect clusters to grow or annihilate based on the type

of cluster interactions, and the emission and adsorption rates of interstitials and

vacancies. In BCC iron the stable configurations for the clustering of self-interstitial

atoms, SIAs, is for them to be arranged as <111> or <110> crowdions or <110>

dumbbells, with the <111> crowdions on the {110} plane being the most energetically

favorable [24], [53]–[55]. Crowdions and split dumbbells are groups of m number of

atoms that are aligned in the <111> direction where if m is odd it is known as a

crowdion, and if m is even it is known as a split dumbbell [54]. Thermodynamics

dictates that once a critical number of defects combine in a cluster it becomes energetically favorable for a dislocation loop to grow, becoming a stable feature in the microstructure, and continuing to expand with increasing irradiation exposure [24], [56], [57].

In F-M steels two types of dislocation loops form, <100> dislocation loops on the {100} habit plane that are sessile until approximately 500° C, and $\frac{1}{2}$<111> glissile loops. For the $\frac{1}{2}$<111> loops the actual habit plane is still under investigation, with simulations predicting either habit planes of {110} or {111} depending on initial cluster size, while TEM characterization has only verified the {111} habit plane [53], [58]–[61].

There is also disagreement on the formation mechanism of <100>{100} loops. An earlier study concluded that both loop types nucleated from $\frac{1}{2}$<110> faulted loops that are exposed to shear in either the $\frac{1}{2}[00\bar{1}]$ or $\frac{1}{2}[0\bar{1}0]$ directions [53], [62], [63], but studies have failed to locate the initial faulted loops raising doubt about the original mechanism [59]. A more recent Molecular Dynamics study presented a theory where the <100>{100} loops are formed when small $\frac{1}{2}$<111> clusters, created during the collapse of the damage cascade, interact with each other. Initially the <100> loops are most stable on the {110} habit plane, but shift to the {100} plane once a critical loop size of approximately 70 atoms is reached. The $\frac{1}{2}$<111> loops form via the biased interstitial absorption of interstitials by $\frac{1}{2}$<111> clusters [53], [58], [59], [62], [64].

The type of loop present has significant impact on the mechanical properties of the material, because the <100>{100} sessile loops have a greater resistance to dislocation motion. The ratio of $\frac{1}{2}$<111> loops to <110> loops depends on the irradiation

temperature and dose, where at low temperature and low dose $\frac{1}{2}$<111> loops are relatively

immobile resulting in an abundance of small $\frac{1}{2}$<111> loops. As the temperature increases

to 400° C, or at large doses, then the $\frac{1}{2}$<111> loops migrate through the material and

annihilate at dislocation lines, grain boundaries, or point defects. The <100>{100} loops

are still immobile and continue to grow resulting in their prominence. If the material is

irradiated at higher than 500° C then the <100>{100} loops become mobile, and both

types annihilate at defects, reducing the overall dislocation loop density [58]–[60]. This

phenomenon is limited with increasing Cr content as RIS leads to enriched Cr

concentration in both loop structures, reducing loop mobility [65].

2.2.4 Voids and Void Swelling

Voids occur within irradiated materials only within the narrow temperature range

between $0.3T_m$ and $0.5T_m$. This is due to the high recombination rate of mobile

interstitials with immobile vacancies and the excessive thermal vacancy concentrations

negating irradiation effects, respectively. However, this temperature band consists of

typical reactor operating temperatures, and this leads to part of the attractiveness of F-M

alloys for nuclear applications, which originated with their increased resistance to void

swelling [3], [36], [60], [66]. Multiple mechanisms have been proposed to explain the

reduced swelling associated with F-M steels based on solute trapping, dislocation loop

structure, and existing dislocation network [3].

Solute trapping is based on weak interactions that bind interstitials to

substitutional species, such as Cr. This interaction slows the rate that interstitials diffuse

to sinks, increasing the probability of vacancy recombination [3], [36], [66]. The Burgers

vector of the dislocation loops present does not have a first order effect on the amount of

swelling induced by irradiation, but the <100> loops have a bias towards interstitials

resulting in a residual concentration of vacancies that are not annihilated. The excess

vacancies interact with the neutral $\frac{1}{2}$<111> loops at a higher rate than the depleted

interstitial flux, initially leading to recombination, and eventually void growth [3], [60].

RAFM alloys develop higher dislocation densities than austenitic alloys during

processing, increasing the availability of neutral sinks, which retard the formation of the

interstitial dislocation loops required to unbalance the vacancy to interstitial defect ratio.

Thus creating an initial population of interstitial defects that must be overcome prior to

initiating void growth [3].

2.2.5 ODS Stability

The addition of Y-Ti-O nanoparticles into the matrix of RAFM steels to provide

strengthening also offers added defect sinks that slow the accumulation of irradiation

damage [67]. These effects depend on the oxides remaining insoluble while exposed to

irradiation, where the possibility exists that a collision event will knock an atom out of

the oxide and into the matrix. Once in solution, it can diffuse back towards the

precipitate, diffuse farther into the matrix, or precipitate back out forming a new oxide.

Contradictory experimental results has led to uncertainty in oxide stability within the

ODS community [40], [68]. Multiple studies have conducted irradiations using neutrons,

ions, and electrons, which ranged in temperature from 300 – 700° C, and concluded that

the oxides dissolve, or break into smaller oxides with increased number density. In these

studies dose increases were accompanied by a decrease in the average oxide size [68]–

[72]. Multiple studies, under similar irradiation conditions, report stable size and density

of the oxide particles [67]–[69], [71], [73]–[75]. Still another study reported Oswald

ripening leading to an increase in oxide size, and decrease in the number density of

particles [72].

The leading theory for precipitate stability is a balance between ballistic ejection

and recombination via back diffusion. Higher dose and dose rate lead to increased oxide

dissociation, but if the irradiation temperature overcomes the activation energy required

for diffusion then the reduction in size is opposed by a flow of atoms back to the

precipitate. Higher dose rates limit the time for back diffusion and promote dissolution,

while the PKA energy determines how likely it is for an oxide atom originating in a to

recoil into solution within the matrix [68]–[72], [76].

 However, a study by Allen et al. reporting decreasing oxide size at higher

temperatures [70], and a study by Lescoat where he described a dependence on initial

particle size , highlight the need for further investigation [71].

2.2.6 Irradiation Induced Hardening

The microstructural changes previously discussed result in the irradiation induced

hardening of the alloy. The general response of an irradiated F-M alloy is shown in

Figure 2.19 where the hardening is associated with increases in the yield strength and

ultimate tensile strength, while the loss of ductility is shown by less total elongation.

This hardening is highly temperature and dose dependent. When irradiation temperatures

are less than $\approx 0.35 T_m$ the formation of interstitial and vacancy loops obstruct dislocation

motion, driving the observed hardening. Raising the irradiation temperature to between

0.35 and $0.40 T_m$ results in a dislocation network developed from loop interactions and the

nucleation of new precipitates, causing hardening to occur. When irradiation

temperatures are greater than $0.40 T_m$ the annealing of defects and the coarsening of

precipitates mitigate the hardening effects. Irradiation hardening is observed at low damage levels, and the defect structure can quickly reach saturation noted by the yield strength and ultimate tensile strength remaining constant as dose increases [3].

The dose and temperature dependence has been reported on in many studies, such as the work on HCM12A where one sample was irradiated at approximately $0.26T_m$ with protons at 400° C to 3, 7, and 10 dpa, and another was irradiated at approximately $0.32T_m$ 500° C to 3 dpa [77]. At 400° C low dose hardening was observed, and saturation occurred around 5 dpa. The amount of hardening at 500° C was less than that associated with the lower temperature irradiations [78]. Work on T-91, HT9, EM10, and Eurofer97-steel under neutron irradiation between 300 and 500° C reported similar results with increasing yield strength and a reduction in elongation percent due to irradiation, but increased temperatures limited the effect [14], [79], [80].

2.2.7 Irradiation Embrittlement

The easy crack propagation low fracture toughness of ODS allows has been the main characteristic that has prevented its use in current technologies, with a value of <100 MPa $\sqrt{m}$ above approximately 200°C [16]. Charpy V-notch testing provides insight into the ductile to brittle transition temperature (DBTT) and the upper shelf energy (USE) that combine with the fracture toughness to develop operation temperatures that prevent catastrophic brittle fracture. The increased flow stress, established during irradiation by the maturity of dislocation networks and precipitates, causes an increase in the DBTT of approximately 150° C and a decrease in USE in F-M steels. This effect is amplified by the production of He with shifts of 200° C reported. Similar to irradiation induced hardening, the shift in DBTT is limited at increased irradiation temperature, and

becomes saturated at high doses [3], [14], [78], [80]. The shift in DBTT has a minimum in F-M steels with a Cr content of 9wt% [25].

Limited data is available on the embrittlement of ODS alloys, but a 1998 study by Kuwabara et al. examined the Charpy impact properties under neutron irradiation. Although a shift between the brittle lower shelf energy (LSE) and the ductile USE existed, the LSE was 65% of USE which suggested limited brittle behavior. This was supported with SEM imaging depicting ductile failure at low temperatures [81]. The addition of thermomechanical treatments during processing such as, isothermal annealing, and controlled rolling have been shown to improve grain bonding, and reduce the ease of crack propagation [16].

2.2.8 Simulating Neutron Irradiation

Neutron irradiation experiments are complicated by sample activation, and slow damage rates leading to high cost and exposure times that last for months or years. The neutronic dose rate depends only on the collisions between neutrons and nuclei, modelled as hard sphere interactions. Based on the limited interaction potential, the transfer of energy between the neutron and the lattice atoms involves a long mean free path creating uniform damage profiles that are slow to evolve. Neutron interactions also create unstable isotopes that split apart through gamma, alpha, or beta radiation requiring careful handling to minimize the activation of equipment and reduce the health hazard to material handlers [24], [55].

In an effort to reduce cost and lag time, ion irradiations are often used to simulate neutron damage. The electrically charged ions provide Coulombic interactions with the electron clouds of target atoms. These collisions are modeled with various interatomic

potentials based on atomic size or kinetic energy, and have an increased radius of effect due to the long range nature of Coulomb's force. The higher the energy of the ion the more likely it is to interact through electronic forces, greatly increasing the dose rate. As the energy is lost neutronic interactions become more probable and the dose rate decreases. This shift in interaction probabilities results in a non-uniform damage profile, as shown in Figure 2.20. The dose is highly dependent on initial energy, ionic charge, and size of the incident particle [24].

Irradiation with ions has drawbacks that must be accounted for during the analysis of experimental data. The shallow depth of penetration of the heavy ions requires surface analysis techniques to account for the non-liner damage profile, while proton irradiations can be assumed uniform on the micron scale that is used for analysis [24], [31], [78]. The nature of the damage cascade is also different, with neutron and heavy ion irradiations resulting in a single large damage cascade containing complex defect networks, while proton and electron irradiations create multiple smaller cascades or a single Frenkel pair respectively [24]. To account for these changes temperature shifts can be considered that develop similar dose rates based on irradiation particle and allow for comparison between irradiation types [26], [78], [82]. Another difference arises when an incident ion exhausts all its energy and comes to rest as an interstitial within the lattice of the target. These implanted ions can alter to local chemistry of the alloy, resulting in precipitation or segregation changes within the material [24], [82].

2.3 Nano-Indentation

The need for harder, stronger, or smaller devices has driven the growth of nano-scaled materials. The desire to measure the mechanical properties at the nano-scale has led to the growth of nano-indentation as an experimental technique.

A diagram depicting a typical transducer found in a nano-indenter is shown in Figure 2.21. The center plate is held in the original position by leaf springs, and during an indentation a DC bias voltage is applied to the bottom plate attracting the center plate, and driving the indenter probe into the sample. The applied voltage is monitored and used to calculate the indentation depth or load based on a calibration of the transducer [83].

2.3.1 Process

Nano-indentation experiments provide a way to measure the hardness and Young's Modulus of materials when the sample size, or region of interest, prevent the use of traditional testing methods. The apparatus is controlled using one of two modes of operation, load control or depth control. For operation in load control a maximum force is selected, and the transducer indents the probe tip into the sample until the set point is reached. Controlling the equipment in depth control entails monitoring the extension of the transducer and then adjusting the applied load until the user specified maximum displacement is reached the loading process ends. Generally operation is recommended in load control as the voltage is easier to monitor than the depth, but investigation of different samples for comparison requires the test be carried out in displacement control to account for indentation size effects [84]. In either mode of operation, the set points are selected to ensure the development of a mature plastic zone [85], [86].

Once the max force or displacement is reached, the tip is held at that load/depth to allow for creep or thermal drift effects to be accounted for. Creep is identified by an increase in depth caused by crystal slip occurring while the sample is under the applied stress. Thermal drift may be seen as either an increase or decrease in depth, and is a result of the expansion and contraction of the equipment due to temperature variations. The hold length is customized for each sample until these two effects reach an equilibrium, and the sample can be unloaded [83], [85].

Unloading of the sample releases the elastic stress within the sample, and the response provides insight into the elastic modulus. The load and displacement are recorded throughout the test process, with a typical graph shown in Figure 2.22. If the deformation is entirely elastic then the loading curve is indistinguishable from the unloading curve, but for elastic plastic contact, the area between the curves represents the energy required for plastic deformation. The unloading curve is analyzed to calculate the contact area and the contact stiffness of the specimen, which in turn are used to calculate the mechanical properties of the sample [85].

2.3.2 Tip Geometries

There are an unlimited number of tip geometries, with customizable probes offered for specialized testing, but the most common tips are: the flat punch, the spherical, the conical, the Vickers, and the Berkovich probes. To understand the derivations that follow, an understanding of the spherical, conical, and Berkovich geometries is required. To guide the reader, a summary of the tips and their uses is listed in Table 2.2. In addition to the applications listed, the spherical and conical geometries are used to model the contact response of the more complicated Berkovich probe, where

the spherical indenter describes the elastic deformation that occurs prior to penetrating

deeper than the tip radius, and the conical indenter has traditionally been used to model

the plastic zone, and associated stress fields of pyramidal geometries [87].

The Berkovich probe is a three sided pyramid, which is preferred in nano-scale

testing because it is easier to grind the faces to a sharp point. However, it is not possible

to produce the theoretical infinitely sharp tip, and current processes allow for the

manufacture of a Berkovich probe with a tip radius of 50-150 nm. The tip radii is further

reduced by preferentially selecting the probes with smaller geometric imperfections. To

limit frictional forces the Berkovich has an angle of 142.3° between each face, with that

angle also being chosen as it gives the same area to depth ratio as the older Vickers

geometry, allowing for easier comparison of indentation data [85], [87], [88].

2.3.3 Data Fitting

Nano-hardness is a ratio of the peak load to the contact area, as defined by:

$$H = \frac{P_{max}}{A_C}$$
                                                                    Equation 2.12 [89]

where H is the nano-hardness, P_{max} is the maximum load, and A_C is the contact area

between the sample and the probe at maximum load. The small scale of nano-indentation

test prevents direct measurement of the contact area, and an intimate knowledge of tip

geometry and contact depth is required for an accurate estimate. The contact stiffness is

described as the instantaneous slope of the unloading curve, $\frac{dP}{dh}$, where h is the

indentation depth, and it plays a key role in determining the contact depth. It is

calculated using a fitted model that describes the load and displacement data [85], [89].

Initially Doerner and Nix presented a fitting method derived from modeling the

tip geometry of a flat punch, which has a constant contact area throughout indentation,

resulting in a linear unloading curve. This linear relationship matched experimental observations at the time, which were mainly on ceramic materials. Elastic materials have a large linear region during unloading, which allowed Doerner and Nix to approximate the curve using the upper third of the data. The linear fit was then used to calculate an extrapolated depth which was used with a geometric factor to calculate the contact area for the specific tip [89]. When using the linear method, the unloading curve is described as:

$$P = 2aE^*h$$ **Equation 2.13** [85]

With a being the contact radius, and E^* being the combined elastic modulus, or elastic modulus of the entire system.

As more materials were examined, the limitations of the linear method were discovered, and Oliver and Pharr developed a method using a power law fit to describe the unloading curve:

$$P = \alpha(h - h_f)^m = \alpha h_e{}^m$$ **Equation 2.14** [89]

where α is a material constant, and m is a constant that ranges between 1.2 and 1.6 depending on how well the material maintains the geometry of the probe tip after unloading. For a perfectly conical indent m is equal to 2.0. The power law fit method provides a contact stiffness that changes throughout the unloading process, which is confirmed by a dynamic technique that measures contact stiffness during testing [89]. This more accurate model is the preferred method for fitting the unloading curve, and is used to calculate the contact area, hardness, and elastic modulus, as described below [89].

2.3.4 Contact Mechanics

     The first mathematical description of a material's elastic response to indentation was developed by Hertz in the 1890's, where he described the contact between two elastic spheres. In the case where one sphere is much much larger than the other, the model describes the contact of a spherical indenter with a radius, R, applied to an infinite half space. This model applies to the elastic deformation that results from a pyramidal indenter, when the contact depth is less than the radius of curvature of the indenter tip. Hertz described the contact radius of the spherical indenter as a function of spherical radius as follows:

$$a^3 = \frac{3}{4}\frac{PR}{E^*}$$ **Equation 2.15** [85]

where the combined modulus, E^*, depends on the elastic modulus of the sample, E, the elastic modulus of the system, E', and the Poisson's ratios, v, v', of the specimen and the indenter respectively:

$$\frac{1}{E^*} = \frac{1-v^2}{E} + \frac{1-v'^2}{E'}$$ **Equation 2.16** [85]

     Equation 2.15 can be rearranged for load, and substituted into the definition of pressure, $p = P/A_C$, where the contact area for a circle is πa^2, to derive an expression relating the indentation stress to the indentation strain, a/R. The indentation stress is assumed to be the same as the average contact pressure.

$$p_{ave} = \left[\frac{4}{3}\frac{E^*}{\pi}\right]\frac{a}{R}$$ **Equation 2.17** [85]

For elastic deformation, the maximum shear stress is, $\tau_{max} \approx 0.47 p_{ave}$, and the von Mises yielding criteria is, $\tau \approx 0.5\sigma_{ys}$, which causes the calculated the contact pressure required for plastic flow to be $p_{ave} \approx 1.1\sigma_{ys}$.

The development of the plastic zone will be discussed at length in a later section, but it can be shown that as the load increases the plastic zone expands, bringing about a constant contact pressure, which is the criteria for the fully developed plastic zone that is required for an accurate nano-hardness measurement. The evolution of the deformation from elastic contact to fully developed plastic zone is described in in Figure 2.23. Region 1 is characterized by elastic contact, where the average indentation stress changes linearly with indentation strain. Region 2 describes the transition between elastic and plastic deformation, where the mean contact pressure begins to transition away from its linear dependence on indentation strain. The third region evolves into a fully developed plastic zone, with the indentation strain no longer depending on the applied load. It is this state that allows for the indentation hardness, H, of a material to be calculated using Equation 2.12 [85].

Once a penetration depth deeper than the tip radius has been achieved, the spherical model is no longer valid, and the contact surface is modeled as a conical indenter. For complex pyramidal geometries this assumption simplifies the contact mechanics allowing for a mathematical description of the indentation process, and according to the Saint-Venant's Principle it will not alter the induced strain field [90].

To accurately model a pyramidal indenter as a cone, the contact area to depth ratio must be conserved, which is accomplished by adjusting sharpness of the cone, or the conical angle, α. For a Berkovich probe, the contact area is described as:

$$A_C = 3\sqrt{3}h_c^2 tan^2\theta \qquad \qquad \textbf{Equation 2.18 } [85]$$

with h_c being the contact depth, which is equal to the depth where plastic deformation begins, and is also known as the plastic depth. The contact area for a conical indenter can be shown to be:

$$A_C = \pi h_c^2 tan^2 \alpha \qquad\qquad \textbf{Equation 2.19 } [85]$$

By equating Equation 2.18 and Equation 2.19 and substituting the face angle for a Berkovich probe, $\theta = 65.27°$, it is possible to solve for the conical half angle, and an expression for contact area. In this case, $\alpha \approx 70.3°$, and the contact area reduces to:

$$A_C = 24.5 h_c^2 \qquad\qquad \textbf{Equation 2.20 } [85]$$

This allows for a mathematical description of the loading curve, once a fully developed plastic zone has formed:

$$P = E^* \left[\frac{1}{\sqrt{\pi}tan\alpha} \sqrt{\frac{E^*}{H}} + \left[\frac{2(\pi - 2)}{\pi} \right] \sqrt{\frac{\pi}{4}} \sqrt{\frac{H}{E^*}} \right]^{-2} h^2 \qquad \textbf{Equation 2.18 } [85]$$

Notice that the load is proportional to the square of the displacement [85].

The unloading of the indenter tip results in an entirely elastic recovery of the strained sample; excluding the plastically deformed region, which remains permanently deformed. As the load is decreased the sample is again modeled as a conical indenter contacting an infinite half space, with the load described as:

$$P = \frac{\pi a}{2} E^* acot\alpha \qquad\qquad \textbf{Equation 2.19 } [85]$$

where $acot\alpha$ is equal to the contact depth h_c. The contact depth is related to the indentation depth as shown in Figure 2.24, and mathematically as:

$$h = \left(\frac{\pi}{2} - \frac{r}{a}\right) h_c \qquad \text{Equation 2.23 [85]}$$

with r being a radius of interest. Combining Equation 2.22 and Equation 2.23, and

looking directly below the indent, $r = 0$, allows for a description of the load

displacement curve:

$$P = \left(\frac{2E^*}{\pi} tan\alpha\right) h^2 \qquad \text{Equation 2.24 [85]}$$

where again the unloading proportional to the square of the displacement. The shape is

slightly altered from loading condition due to the differing constants in Equation 2.21 and

Equation 2.24 caused by the entirely elastic recovery associated with unloading [85],

[90], [91].

Determination of the elastic modulus requires calculation of the contact stiffness

from the unloading curve, and a series of mathematical substitutions (detailed in [85]) to

develop a relationship for the contact depth which is shown here as:

$$h_c = h_t - \left[\frac{2(\pi - 2)}{\pi}\right] \frac{P_{max}}{dP/dh} \qquad \text{Equation 2.22 [85]}$$

As shown in Equation 2.16 the modulus that is measured during indentation is not of the

sample alone. To isolate the modulus of the sample the combinde modulus is calculated

as:

$$E^* = \frac{dP}{dh} \frac{1}{2} \frac{\sqrt{\pi}}{\sqrt{A}} \qquad \text{Equation 2.23 [85]}$$

and Equation 2.16 is used to solve for E.

2.3.5 Development of Plastic Zone

In his 1950 text, "The Mathematical Theory of Plasticity," Hill describes the

formation of the semi-spherical plastic zone that develops during wedge indentation.

Describing the plastic deformation in terms of r/c, where r is the position of an element at the onset of distortion, and c is the radius of the plastic zone, allows for investigation of the relationship of between stress and strain in terms of deformation velocity. Scaling the deformation shows that the geometry does not change in shape as time progresses, it only changes in size. A detailed derivation of the deformation mechanics is available in [92], and concludes that material equal distance from the origin will be radially deformed by the plastic stress field, resulting in the characteristic half circle appearance of the plastic zone as shown in Figure 2.25.

The points ABDEC describe the plastic zone, where AC is the region of the surface that has experienced pile up, AB describes the contact between the sample and the indenter, and BDEC is a slip line. By solving for different boundary conditions, Hill shows that the velocity varies along β slip lines, and there is constant displacement from the origin along α slip lines. As the load increases, yielding occurs in semi-spherical shells adjacent to the previously deformed material. This process causes the continuous growth of the plastic zone with ever increasing size, but consistent shape.

The observed extension of the plastic zone beyond the tip of the indenter is associated with sear stresses that result from a fully developed plastic zone around the indent. As the probe is indented deeper the region around the tip is already plastically deformed, and in order to accommodate the stress, the material is sheared parallel to the edge of the plastic elastic boundary creating an extended plastic zone whose shape is characteristic of the material and independent of indenter geometry as distance from the indenter increases [90], [92], [93].

The characteristic shape of the plastic zone allows for quick understanding of the elastic plastic property of the material. If the expanded plastic zone remains entirely contained beneath the contact radius of the indenter then elastic effects are the dominate feature in the deformation. However, if the plastic zone spreads out from under the indenter as is the case for Figure 2.25, then plastic deformation dominates and the elastic effects are secondary. This curvature can be predicted by looking at a ratio of the Young's modulus to the uniaxial stress. When $E/\sigma_r \leq 110$, then the elastic strains greatly impact the development of the plastic zone. [94].

When predicting the size of the plastic zone the complex stresses that develop, due to the indenter shape, make the mathematics convoluted. A simplifying approximation has historically been used to model the plastic deformation as an expanding spherical cavity with the geometry depicted in Figure 2.26 and the yielding criteria of:

$$\sigma_\theta - \sigma_r = \sigma_{ys} \qquad \textbf{Equation 2.27 } [94]$$

[92], [94]–[96]. The elastic-plastic boundary is assumed to be an elastic compressible core, leading to the following relationship between expanding core radius, R, and the developing plastic zone radius, c:

$$\frac{dR}{dc} = \frac{3(1-v)Y(\epsilon)c^2}{ER^2} - \frac{2(1-2v)Y(\epsilon)R}{Ec} \qquad \textbf{Equation 2.28 } [94]$$

where $Y(\epsilon)$ is the uniaxial strain hardening law that combines with Hooke's law to describe the elastic and plastic deformation for a material.

$$\sigma = \begin{pmatrix} E\epsilon \\ Y(\epsilon) = K\epsilon^n \end{pmatrix} \qquad \textbf{Equation 2.29 } [97]$$

The plastic region is described in terms of a strength coefficient, K, and the strain hardening coefficient, n.

Work by Hill and Johnson showed that for an elastic perfectly plastic material with no strain hardening, $n = 0$, and $K = \sigma_{ys}$, the solution of Equation 2.28 is:

$$\frac{c}{R} = \left(\frac{2E}{3\sigma_{ys}}\right)^{1/3} \qquad \textbf{Equation 2.30 [92]}$$

$$c = \left(\frac{3P}{2\pi\sigma_{ys}}\right)^{1/2} \qquad \textbf{Equation 2.31 [98]}$$

in terms of elastic modulus or applied load, respectively [92], [94]–[96], [98], [99].

When accounting for stain hardening effects, Equation 2.28 no longer has a direct solution. Instead the internal pressure of the cavity, p_{cav}, along with a series of mathematical approximations, is used to relate the size of the plastic zone to the mechanical properties. The general form for the internal pressure is:

$$p_{cav} = \frac{2}{3}\sigma_{ys} + 2\int_{R}^{c} Y(\epsilon)\frac{d\rho}{\rho} \qquad \textbf{Equation 2.32 [94]}$$

and is utilized in a 2006 study by Mata to describe the plastic zone size for a fully plastic material in terms of nano-hardness, yield stress, and the Young's modulus by relating the geometries of a spherical and a conical indenter to create identical plastic zones.

$$\frac{H}{\sigma_r} = f\left[\frac{2}{3}\right]\left(\frac{\epsilon_{ys}}{0.1}\right)^n + \Theta(n) + M(n)\left(\frac{z_{ys} + 1.217a_s}{a_s/0.635}\right)^{P(n)} \qquad \textbf{Equation 2.33 [94]}$$

In this relationship σ_r is the uniaxial stress at a characteristic strain of 0.1, which Tabor proposed, and verified in [100], [101] for sharp indenters, leads to the following predictive relationship for hardness regardless of material:

$$\sigma_r = \frac{H}{2.7} \qquad \textbf{Equation 2.34 [94]}$$

Other research has shown that Tabor's approach cannot accurately predict the stress strain relationship, and fails to apply for all materials [102], [103]. The applicability of Equation 2.34 in terms of predicting material properties requires further investigation over a range of indentation parameters.

The terms $\Theta(n)$, $M(n)$, and $P(n)$ are functions that depend on the strain hardening coefficient:

$$\Theta(n) = 2.5968 + \frac{0.5097}{n} \qquad \textbf{Equation 2.35 [94]}$$

$$M(n) = -2.2778 - \frac{0.5479}{n} \qquad \textbf{Equation 2.36 [94]}$$

$$P(n) = -3.0615\,n - 0.005 \qquad \textbf{Equation 2.37 [94]}$$

the contact radius, a_s, is defined by a spherical indenter whose radius equals the contact radius and total penetration depth of a conical indenter, shown in Figure 2.27 and geometrically equal to:

$$\frac{a_s}{R} = \frac{2\,tan\theta}{1 + tan^2\theta} = 0.635 \qquad \textbf{Equation 2.38 [94]}$$

The term z_{ys} is the depth of the plastic zone directly below the indenter. A diagram depicting how the plastic zone radius depends on the terms in Equation 2.33 and Equation 2.38 is shown in Figure 2.28.

Using finite element analysis, FEA, Mata was showned that Equation 2.33 can be applied to Berkovich indentation when three factors are met. First $f = 1.101$, and describes the projection factor, or geometry, for a Berkovich probe. The conical half angle used to describe the contact radius is equal to 70.3°. Finally the contact radius is

measured to be the length from the center of the indent to the edge of the pyramid measured 25° from the corner of the probe, as shown in Figure. 2.29 [94].

<u>2.3.5.1 Plastic Zone Imaging</u>

Bright field TEM imaging can be used to observe the induced plastic zone after nano-indentation due to the development of strain contrast, dislocations, stacking faults, or other deformation [104]. The plastic zone can be imaged either through a cross section of the sample that is obtained through the use of a Focused Ion Beam, FIB, or through top down imaging parallel to the beam. In the latter case, a dislocation "disk" is imaged that provides information on the dislocation nucleation mechanics, and size of plastic deformation [105], [106]. Cross sectioned images are the most common method of plastic zone imaging, and give a clear picture of depth, and radius of the induced plastic deformation [107]. Both methods of TEM imaging show plastic deformation that is not spherical as predicted by Hill and Johnson, but varies in shape based on the slip mechanisms within the crystal [106], [108].

Plastic deformation has also been measured through crystal orientation maps developed using Electron Backscatter Diffraction, EBSD. The resolution of EBSD is limited compared to TEM, but comparative studies between the two techniques provide strong agreement in plastic zone size and shape [107], [109].

Independent of imaging technique, single crystal samples or, samples with a large grain structure, are commonly imaged to limit contrast within the sample. Imaging the plastic zone in polycrystalline materials is made more difficult by the complex dislocation network that develops during indentation, and the variations in crystal orientation between adjacent grains. A study by Bose and Klassen presented work on

such a material that estimated the size of the plastic zone by observing dislocation contrast within grains, and the reshaping of grain boundaries to accommodate the indentation stresses. A TEM image from their study is presented in Figure 2.30 for comparison to those collected in this work [110].

2.3.6 Developed Stress Fields

The stress field developed by a pyramidal indenter is initially elastic, but transitions to plastic when the contact radius becomes larger than the tip radius of the indenter. The initial elastic response can be modeled as the contact between two semi-infinite half spheres, which was developed by Hertz under the following assumptions:

1. The displacement and stresses are defined by the differential equations for elastic bodies, with the stress being nominal at large distances from the area of contact.

2. The contact is frictionless.

3. The contact pressure at the surface is equal and opposite within the region of contact, and zero outside of it.

4. The contact region is described by a distance of separation of zero within the contact area and greater than zero away from the contact area.

5. The force of interaction between the indenter and the surface is described by the integral of the pressure distribution within the area of contact.

These assumptions allowed Hertz to describe the stress fields developed based on the pressure distribution, and were adapted by Boussinesq to describe the elastic stresses under point contact. Timoshenko and Goodier presented the relationships in polar coordinates [90]:

$$\sigma_r = \frac{P}{2\pi}\left[(1-2v)\left[\frac{1}{r^2} - \frac{z}{r^2(r^2+z^2)^{1/2}}\right] - \frac{3r^2z}{(r^2+z^2)^{5/2}}\right] \qquad \textbf{Equation 2.39 [90]}$$

$$\sigma_\theta = \frac{P}{2\pi}\left[(1-2v)\left[-\frac{1}{r^2} + \frac{z}{r^2(r^2+z^2)^{1/2}}\right]\right. \qquad \textbf{Equation 2.40 [90]}$$

$$\left. + \frac{z}{(r^2+z^2)^{3/2}}\right]$$

$$\sigma_z = -\frac{3P}{2\pi}\frac{z^3}{(r^2+z^2)^{5/2}} \qquad \textbf{Equation 2.41 [90]}$$

$$\tau_{rz} = -\frac{3P}{2\pi}\frac{rz^2}{(r^2+z^2)^{5/2}} \qquad \textbf{Equation 2.42 [90]}$$

The strains can be calculated from the polar form of Hooke's law:

$$\epsilon_r = \frac{\sigma_r - v(\sigma_\theta + \sigma_z)}{E} \qquad \textbf{Equation 2.43 [90]}$$

$$\epsilon_\theta = \frac{\sigma_\theta - v(\sigma_r + \sigma_z)}{E} \qquad \textbf{Equation 2.44 [90]}$$

Once the contact radius becomes larger than the tip radius of the indenter the sample begins to deform plastically, and the spherical tip approximation no longer applies. Work by Chiang, Marshall, and Evans related the plastic stress fields to a ratio of the volume of the plastic zone to the volume of the indenter, β, which can be expressed in terms of the plastic zone and contact radii. For a Berkovich probe β has been shown to be:

$$\beta = \frac{c}{a} = \left(\frac{b}{\bar{a}}\right)\left(\frac{\sqrt{2}\pi}{\cot(\theta/2)}\right)^{1/3} \qquad \textbf{Equation 2.45 [111]}$$

where $\bar{a}$ and θ are the indentation diagonal, and the face angle respectively. During loading the radial and tangential stresses for the developing plastic zone and the elastically stressed regions of the sample were shown to be [111]:

$$\frac{\sigma_r^{pl}}{p} = \left(\frac{3\ ln(r/a)}{1+3\ \ln(\beta)}\right) - 1, \qquad (\beta > \frac{r}{a} > 1)$$

Equation 2.46 [111]

$$\frac{\sigma_t^{pl}}{p} = \frac{3\left[\ln\left(\frac{r}{a}\right) + 1/2\right]}{1+3\ \ln\beta} - 1, \qquad (\beta > \frac{r}{a} > 1)$$

Equation 2.47 [111]

$$\frac{\sigma_r^{el}}{p} = \frac{-\beta^3}{(r/a)^3(1+3\ \ln\beta)}, \qquad \left(\frac{r}{a} > \beta\right)$$

Equation 2.48 [111]

$$\frac{\sigma_t^{el}}{p} = \frac{\beta^3}{2(r/a)^3(1+3\ \ln\beta)}, \qquad \left(\frac{r}{a} > \beta\right)$$

Equation 2.49 [111]

After the load has been removed the stress relationships become:

$$\frac{\sigma_r^{pl}}{p} = \left(\frac{3\ ln(r/a)}{1+3\ \ln(\beta)}\right) - 1 + \frac{1}{(r/a)^3}, \qquad (\beta > \frac{r}{a} > 1)$$

Equation 2.50 [111]

$$\frac{\sigma_t^{pl}}{p} = \frac{3\left[\ln\left(\frac{r}{a}\right) + 1/2\right]}{1+3\ \ln\beta} - 1 - \frac{1}{2(r/a)^3}, \qquad (\beta > \frac{r}{a} > 1)$$

Equation 2.51 [111]

$$\frac{\sigma_r^{el}}{p} = \frac{1}{(r/a)^3} - \left[1 - \frac{\beta^3}{1+3\ \ln\beta}\right], \qquad \left(\frac{r}{a} > \beta\right)$$

Equation 2.52 [111]

$$\frac{\sigma_t^{el}}{p} = \frac{1}{2(r/a)^3}\left[\frac{\beta^3}{1+3\ \ln\beta} - 1\right], \qquad \left(\frac{r}{a} > \beta\right)$$

Equation 2.53 [111]

Around the same time, Yoffe [93] developed a model describing the stress state by modeling pyramidal indenters using a conical geometry. He developed relationships depicting the elastic stress field that develops to support the load resulting from the hemispherical plastic zone:

$$\sigma_r = \frac{P}{2\pi r^2}(1 - 2v - 2(2 - v)cos\theta)$$

Equation 2.54 [93]

$$+ \frac{B}{r^3}4\big((5 - v)cos^2 - (2 - v)\big)$$

$$\sigma_\theta = \frac{P}{2\pi r^2}\frac{(1-2v)cos^2\theta}{(1+cos\theta)} - \frac{B}{r^3}2(1-2v)cos^2\theta$$

Equation 2.55 [93]

$$\sigma_\phi = \frac{P(1-2v)}{2\pi r^2}\left(cos\theta - \frac{1}{1+cos\theta}\right)$$

Equation 2.56 [93]

$$+ \frac{B}{r^3}2(1-2v)(2-3cos^2\theta)$$

$$\tau_{r\theta} = \frac{P(1-2v)}{2\pi r^2}\frac{sin\theta cos\theta}{1+cos\theta} + \frac{B}{r^3}4(1+v)sin\theta cos\theta$$

Equation 2.57 [93]

$$\tau_{r\phi} = \tau_{\theta\phi} = 0$$

Equation 2.58 [93]

where B is a constant that describes the size and shape of the plastic zone, and has been

shown to be:

$$B = 0.2308\frac{Ea^3}{\pi}f$$

Equation 2.59 [90]

where f is the densification factor, where a perfectly dense material would have a value

of 1, and the factor decreases with density [93]. In the case of ODS alloys the reported

density that results from processing is within 0.5% of the theoretical density, and f can

be estimated as 1 [18], [90].

2.3.7 Finite Element Analysis

Numerical modeling, has become an invaluable tool to verify nano-indentation

experiments, due to the intricate contact mechanics. Assuming an isotropic material that

experiences strain hardening, it is possible to express the stress and strain relationship in

the form of Equation 2.29, where the strength coefficient is:

$$K = \sigma_{ys}\left(\frac{E}{\sigma_{ys}}\right)^n$$

Equation 2.60 [112]

The load and contact depth are dependent variables that are functions of Young's

modulus, Poisson's ratio, yield strength, strain hardening exponent, total indentation

depth, and the indenter half angle. Performing dimensional analysis leads to:

$$P = Eh_t^2 \Pi_\alpha \left(\frac{\sigma_{ys}}{E}, \nu, n, \theta \right)$$
Equation 2.61 [113]

$$h_c = h \Pi_\beta \left(\frac{\sigma_{ys}}{E}, \nu, n, \theta \right)$$
Equation 2.62 [113]

where

$$\Pi_\alpha = \frac{P}{Eh_t^2}$$
Equation 2.63 [113]

$$\Pi_\beta = \frac{h_c}{h_t}$$
Equation 2.64 [113]

Using FEA it is possible to evaluate the shape of the loading curve, described by the

dimensional analysis results, to determine the yield stress, strength coefficient, hardness,

Young's modulus, and determine the strain-hardening exponent depending on what

parameters are known, as well as the effects of sink-in, pile-up, and friction [94], [100]–

[103], [112]–[114].

2.3.8 Indentation Size Effect

Indentation size effect, ISE, describes the phenomenon where nano-hardness

increases as the indentation depth decreases. The theory of geometrically necessary

dislocations explains this effect as the large strain gradients associated with small indents

create dislocations as the material shifts to accommodate the strain. These geometrically

necessary dislocations interact with the statistically stored dislocations, which result from

homogeneous strain, to alter the flow stress. Nix and Gao provide the mathematical

foundations of this model, and show that ISE can be predicted as:

$$\frac{H}{H_0} = \sqrt{1 + \frac{h^*}{h}}$$

Equation 2.65 [115]

where H_0 is the hardness associated with the intrinsic dislocation network, and h^* is the length dependence of hardness:

$$H_0 = 3\sqrt{3}\alpha Gb\sqrt{\rho_s}$$

Equation 2.63 [115]

$$h^* = \frac{81}{2}b\alpha^2\tan^2\theta\left(\frac{G}{H_0}\right)^2$$

Equation 2.64 [115]

where b is the Burgers vector, α is constant equal to 0.5, ρ_s is the statistically stored dislocation density, and θ is the angle between the sample's surface, and the edge of the indenter. ISE is more pronounced in materials with low intrinsic dislocation densities [84], [115]–[117].

At indentation depths shallower than the radius of curvature of the indenter probe ISE does not follow the Nix and Gao model due to errors caused by deviations from ideal indenter geometry, surface roughness, and uncertain plastic deformation [115], [116].

2.3.9 Strain Hardening Coefficient

Work by Robertson et al. demonstrated that it is possible to determine the elastic modulus, yield strength, and strain hardening exponent through indentation with both a Berkovich and cube-corner probe [97]. Following in the footsteps of Bucaille et al. [102], it was demonstrated that by solving for the representative stress and strain for each probe geometry, a universal strain hardening exponent and yield stress could be calculated. This study investigated the equivalent strain hardening, which described all the radiation induced hardening, experienced by an ODS alloy that was irradiated to 100 dpa at 500° C, and 100 dpa at 600° C by comparison to the original as received condition.

The measured yield stress and strength hardening coefficient were 1300 MPa and 0.26 for

the as received condition, 1340 MPa and 0.27 for irradiation at 500° C, and 1510 MPa

and 0.32 for irradiation at 600° C. In this work Robertson attributes the majority of the

change in equivalent strain hardening exponent to the dissolution of the oxide particles

during irradiation. In a matrix with a high density of oxides, dislocations cannot cut

through the ODS particles due to the misfit strain. Instead, they bypass the oxides via the

Orowan mechanism, which leaves loop debris that deflect dislocations due to irradiation

into alternate slip planes, thus reducing the strain hardening exponent. As the oxide

density decreases less irradiation induced defects are scattered, and less slip planes are

active during plastic deformation. This causes a larger increase in the equivalent strain

hardening exponent [97].

2.3.10 Sources of Error

Indentation experiments have been used to determine the mechanical properties of

materials for over a century, and accurate determination of the hardness, elastic modulus,

strain hardening coefficient, fracture toughness, yield strength and residual stress of a

sample requires knowledge of five experimental parameters: frame compliance, contact

area, initial contact, the nature of pile-up, and contact stiffness. The importance of each

of these parameters will be discussed below to provide insight into the limitations of

nano-indentation experiments [85].

2.3.10.1 Frame Compliance

When performing an indentation experiment it is not only the sample that is

exposed to a compressive force. The testing apparatus responds to the load as well. The

amount of flex within the equipment is known as the frame compliance, and must be

accounted for when determining the actual depth of penetration. The compression of the

load frame, indenter shaft, and sample mount are combined to describe the compliance

constant, C_f, which is used to adjust the measured depth to the actual penetration depth as

follows:

$$h' = h - PC_f$$
<div align="right">**Equation 2.68** [85]</div>

where h' is the adjusted depth. In practice the frame compliance is accounted for when

the system is installed by the technician, and the experimenter does not have to correct it

as long as the system is calibrated. Instead, it is important to know this limitation exists

when determining how to mount the sample, because if the adhesive is not properly

chosen it will contribute to an error in the compliance calibration [85].

2.3.10.2 Determining Contact Area

As previously discussed, micro-indentation experiments leave impressions on the

sample that allow for the contact area to be optically analyzed, but as advances in

processing techniques require indentations be done on the nano-scale, this method is no

longer feasible. Instead, atomic force microscopy (AFM) or laser imaging is required to

adequately measure the contact area of a nano-indent. These are time intensive and

expensive techniques which dictate that the area be estimated using a function derived

from probe geometry, as described in Section 2.3.4.

Unfortunately real world probes are not idea geometries and contain flaws. This

results in a tip area calibration being required each time a probe is used for the first time.

A best fit curve is applied to the results from the calibration, described in [85], and for a

Berkovich probe the corrected tip area is usually of the form:

$$A_c = 24.5h_c^2 + C_2h_c^1 + C_3h_c^{1/2} + C_4h_c^{1/4}$$ **Equation 2.69** [85]

where C_2, C_3, and C_4 are constants that correct for geometrical errors. Once the depth of contact is determined, Equation 2.69 is used to estimate the contact area and calculate the hardness of the sample [85].

2.3.10.3 Determining Surface Contact

The accuracy of the contact depth measurement depends on exact location of the surface of the sample. The point where the tip comes into contact with the surface acts as a zero point for the displacement measurement, and is monitored by looking for a large change in the force or depth signals. In practice, it is found when a user inputted set point is reached. Care must be taken to not set the force set point too high, because it is possible to have the indenter press into the sample prior to reaching the origin set point. It is possible to correct for this by adjusting the initial amount of penetration, h_i [85]:

$$h' = h + h_i$$ **Equation 2.70** [85]

2.3.10.4 Pile-up and Sink-in

The material properties of the specimen can also contribute to measurement errors if pile-up or sink-in occurs. While an indent is being performed, plastic deformation can cause the surface adjacent to the indent to elevate above the original surface height in order to accommodate the stress field. The opposite is also possible, where the sample buckles under the indenter and the surface is no longer in contact with the tip. Diagrams for sink-in and pile-up are presented Figure 2.31. In the first case, the elevated material takes on some of the load from the indenter, and causes the indent to not be as deep. This results in an artificially high hardness that requires AFM imaging or a contact area function calibration to be performed on a material with a similar E/H ratio for correction.

However, both of these solutions are time and money intensive, so it is recommended in ISO 14577 that the effects be ignored and the hardness and modulus values are referred to as 'indentation' hardness or 'indentation' modulus [85].

2.3.10.5 Contact Stiffness

In practice Equation 2.25, and Equation 2.26 slightly differ from the measured values, and a correction factor, β, is used to adjust the contact stiffness. For a Berkovich indenter Dao et al. estimated that $\beta = 1.096$ from experiments, and Cheng estimated $\beta = 1.14$ using finite element analysis. A value of $\beta = 1.034$ is commonly used, but it is accepted that the true value is higher and there is no agreement on what the true value of β is [85]. When applying the correction factor, Equations 2.22 and 2.23 take the following forms:

$$h_c = h_t - \frac{1}{\beta}\left[\frac{2(\pi - 2)}{\pi}\right]\frac{P_t}{dP/dh}$$

Equation 2.71 [85]

$$E^* = \frac{1}{\beta}\frac{dP}{dh}\frac{1}{2}\frac{\sqrt{\pi}}{\sqrt{A}}$$

Equation 2.72 [85]

2.3.10.6 Considerations for Ion Irradiated Materials

Nano-indentation is a technique that is often used because the experiments are straight forward, and the non-destructive nature of the testing. Complications arise when surface topography alters the contact area for a tip, and if the sampled region of an indent is not properly understood. The dose profile, radiation effects, and indentation size effect must be accounted for when ion irradiated materials are nano-indented, and are summarized in Figure 2.32 [84].

When an indent is performed to a specific penetration depth, the hardness and modulus that are reported do not represent just the properties at that depth. Instead, the

properties reflect the entire region that was effected by the developed plastic zone. As a rule of thumb, Hosemann has reported this to be approximately five times the indentation depth. In a uniform sample the extended sampling volume does not cause complications, but due to the shallow dose profiles associated with ion irradiations the sample volume must be well understood when performing the analysis. The non-linear damage profile associated with ion irradiation, shown in Figure 2.20 and Figure 2.32, prevents associating a hardness measurement with a specific dose. Instead a range of doses is required to describe the change in hardness [84].

During irradiation experiments, the surface of the sample can discolor due to oxidation, and sputtering results in a rough surface topography. If the shallow nano-indents to not penetrate deep enough these surface effects cause large standard deviations in the nano-hardness and modulus. The incident ions also become deposited in the sample once their kinetic energy has been exhausted leading to localized altering of physical chemistry. If care is not taken when selecting either an ion that limits local chemistry changes, such as an Fe ion in steel, or in evaluation area, these localized changes will be measured within the samples volume [84].

The indentation size effect is a well studied phenomenon in which the hardness of a material increases with decreasing size. There are multiple theories that attempt to explain this hardening, with the geometrically necessary dislocations theory being the most promising, and this theory is discussed in depth in Section 2.3.8. This effect results in varying hardness values as a function of depth, which dictates that the indentation results must be analyzed at specific depth intervals to normalize the indentation size effects for various conditions [84].

Table 2.1 Effect of Alloying Components on the Reaustenitization Temperature, from [3]**.**

Element	Change in Transition Temperature (°C) per mass percent
Ni	-30
Mn	-25
Co	-5
Si	+25
Mo	+25
Al	+30
V	+50

Table 2.2. A characterization of common geometries for indenter probes and their uses, from [87].
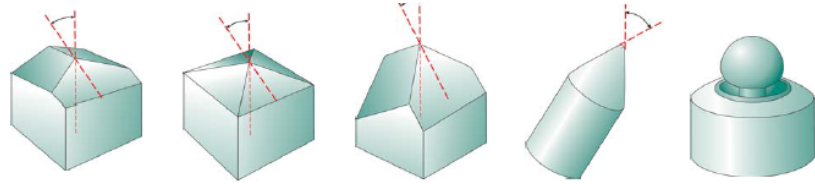
	Berkovich	Vickers	Cube-Corner	Cone (angle ψ)	Sphere (radius R)
Features					
Shape	3-sided pyramid	4-sided pyramid	3-sided pyramid w/ perpendicular faces	Conical	Spherical
Applications	Bulk Materials, Thin Films, Polymers, Scratch Testing, Wear Testing, MEMS, Imaging	Bulk Materials, Films and Foils, Scratch Testing, Wear Testing	Thin Films, Scratch Testing, Fracture Toughness, Wear Testing, MEMS, Imaging	Modeling, Scratch Testing, Wear Testing, Imaging, MEMS	MEMS
Available as Traceable Standard	Yes	Yes	Yes	No	No
Parameter					
Centerline-to-face angle, α	65.3°	68°	35.2644°	—	—
Area (projected), A(d)	$24.56d^2$	$24.504d^2$	$2.5981d^2$	πa^2	πa^2
Volume-depth relation, V(d)	$8.1873d^3$	$8.1681d^3$	$0.8657d^3$	—	—
Projected area/face area, A/A_f	0.908	0.927	0.5774	—	—
Equivalent cone angle, ψ	70.32°	70.2996°	42.28°	ψ	—
Contact radius, a	—	—	—	$d \tan \psi$	$(2Rd-d^2)^{1/2}$

Figure 2.1: Iron-Iron Carbide phase diagram, showing how the concentration of carbon and the processing temperature dictate the phases of steel that are formed, from [118]**.**
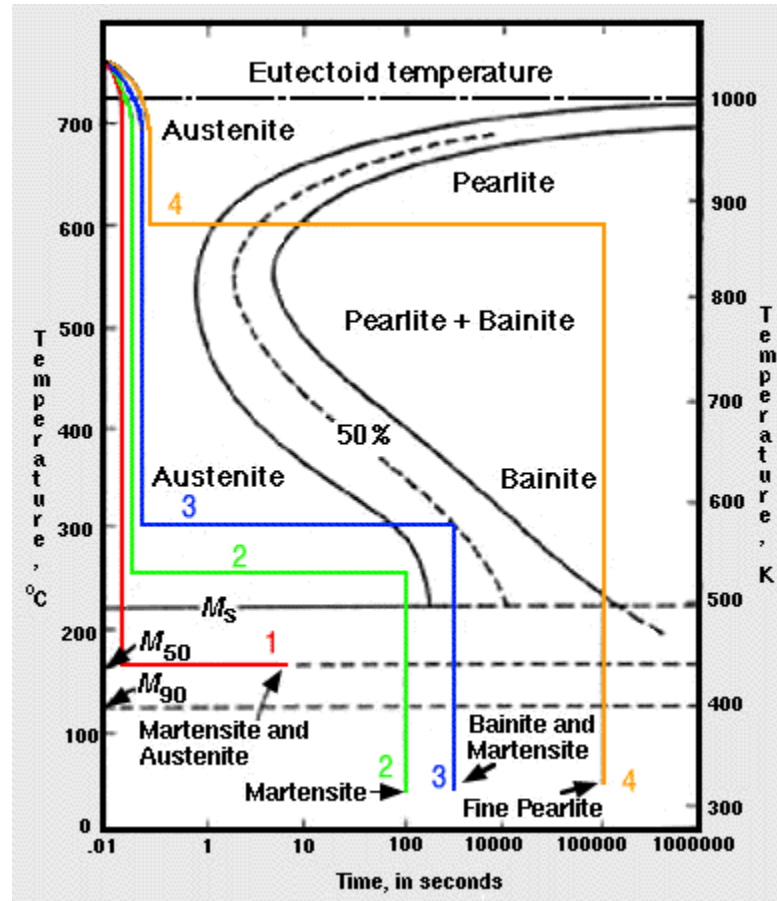
Figure 2.2: A time-temperature-transformation (TTT) diagram showing four different cooling paths through the eutectoid found at T = 738 °C. Path 1 results in a 50% martensite and austenite solution. Path 2 results in a complete martensite transformation. Path 3 results in a bainite and martensite solution. Path 4 results in a complete pearlite microstructure, from [119]**.**
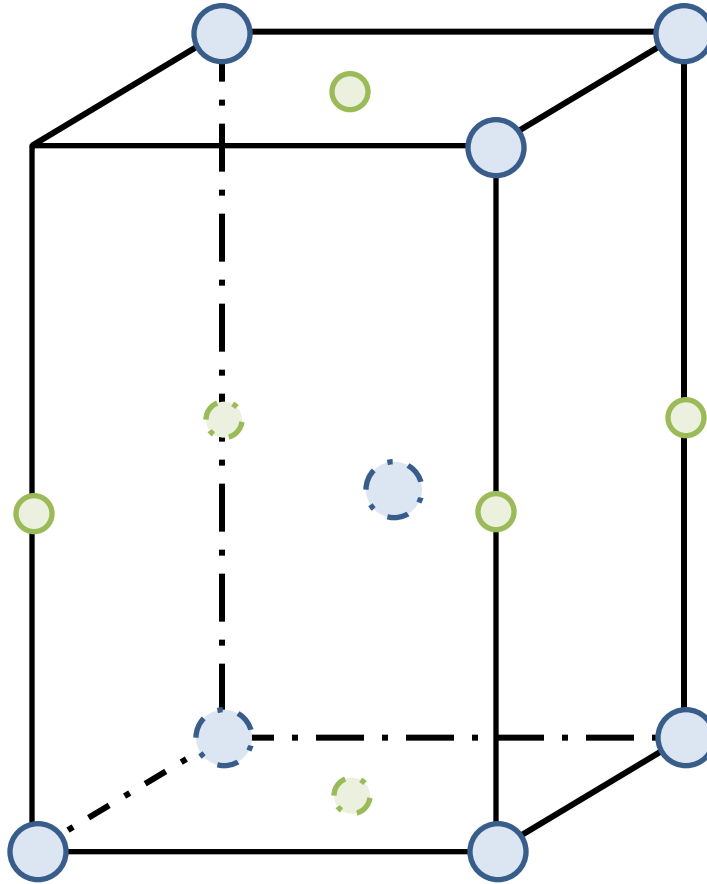
Figure 2.3: A body centered tetragonal (BCT) unit cell showing the location of the iron atoms (blue), and the possible positions for the carbon interstitials (green) for martensite, adapted from [4].
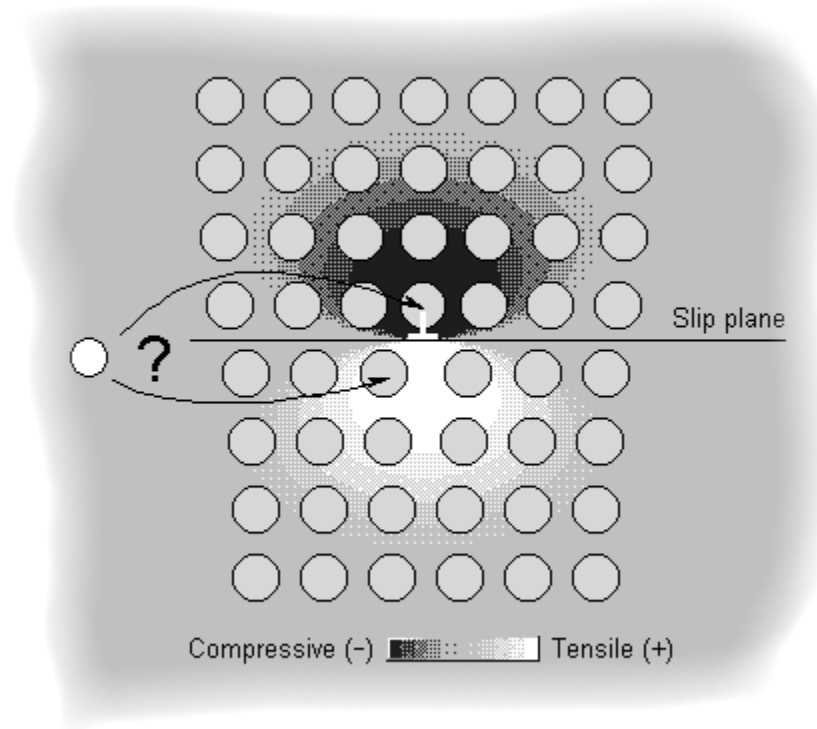
Figure 2.4: **A cross section of an edge dislocation showing the associated compressive and tensile strain fields causes by the insertion of an extra half plane of atoms. These stress fields reduce a materials yield strength, but can be reduced by the inclusion of substitutional or interstitial impurity atoms in solid solution, from [120].**
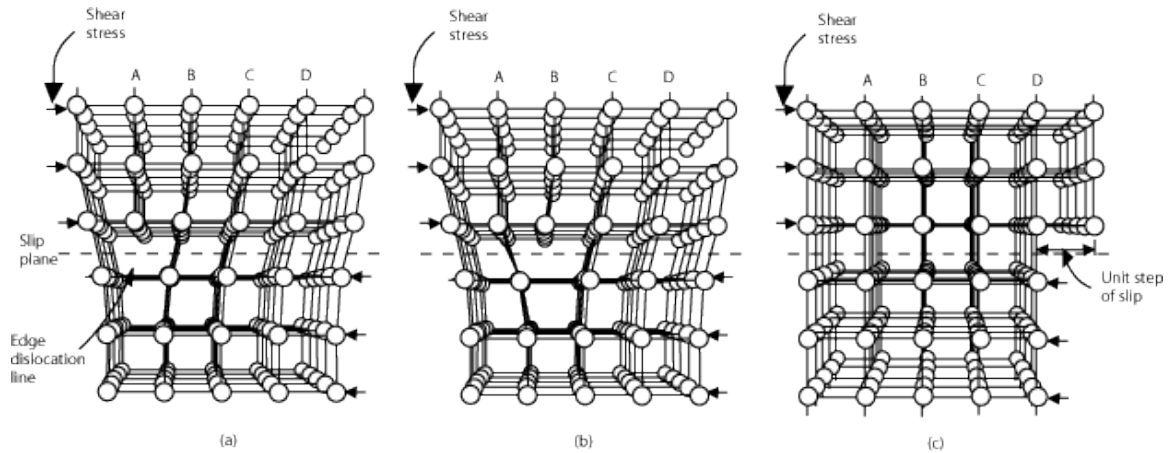
Figure 2.5: A depiction of a cross section of an edge dislocation. In a perfect lattice the energy required to cause plastic deformation must be enough to break all the bonds restricting movement in the slip direction. A dislocation allows plastic deformation to occur more easily, because the dislocation can move through a single bond at a time, from [121].
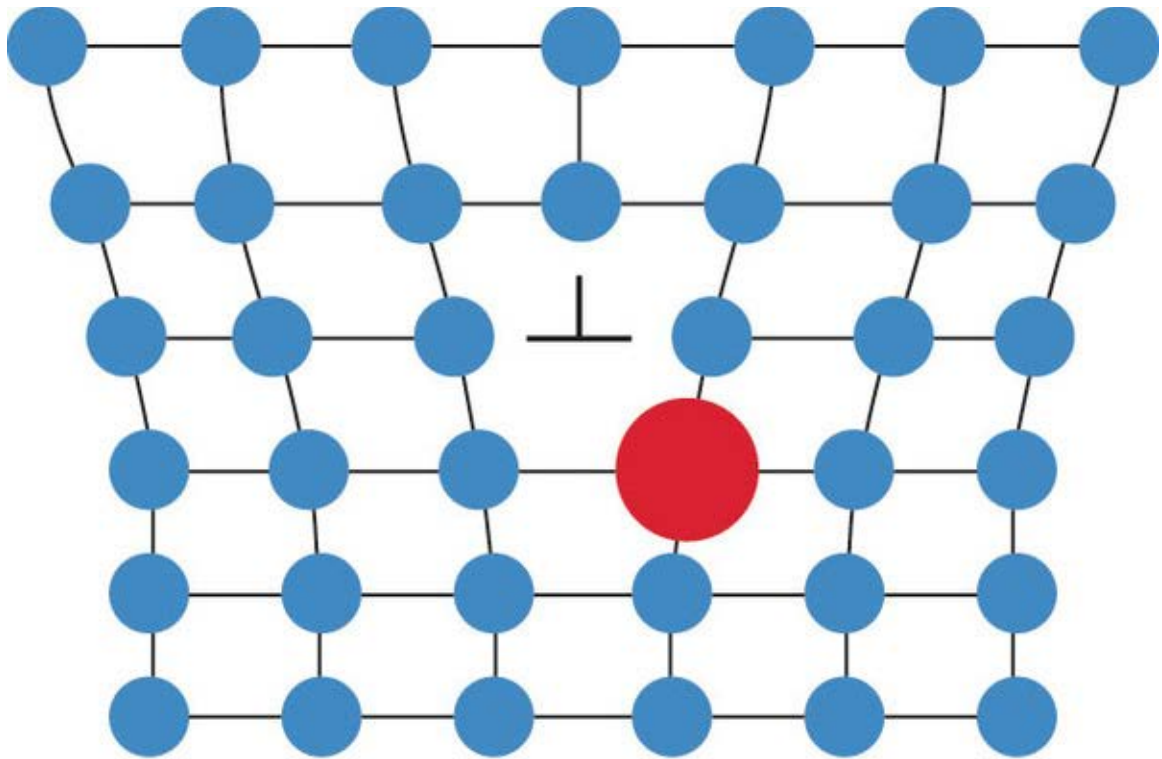
Figure 2.6: The equilibrium position of a large substitutional defect and an edge dislocation, resulting in a reduction in total strain energy of the lattice. A smaller defect atom would come to rest in the compressive strain field associated with the edge dislocation. In this case the overall strain field is again reduced, which makes it more difficult for a dislocation to move, adapted from [122].
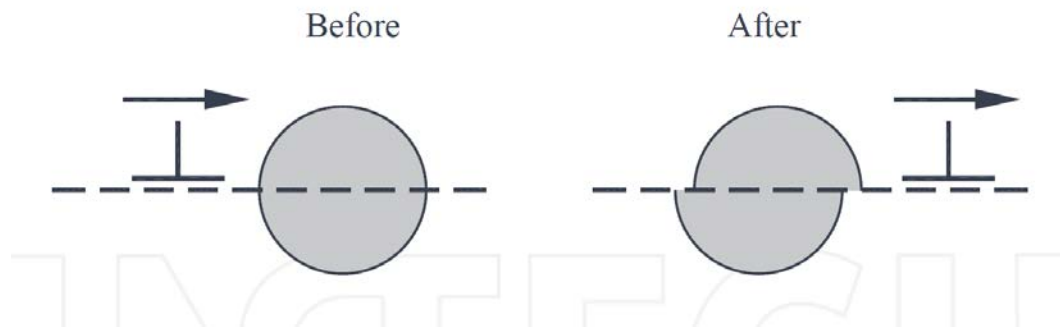
Figure 2.7: The interaction of a dislocation and a precipitate results in a resistance to movement which depends on the strain mismatch. If the precipitate and matrix have a small mismatch then the dislocation cuts through the coherent precipitate with little hardening of the material, from [123].

a) Approach situation

L

Force τb per unit length

b) Sub-critical situation

c) Critical situation

τbL

τb

c) Escape situation

τb
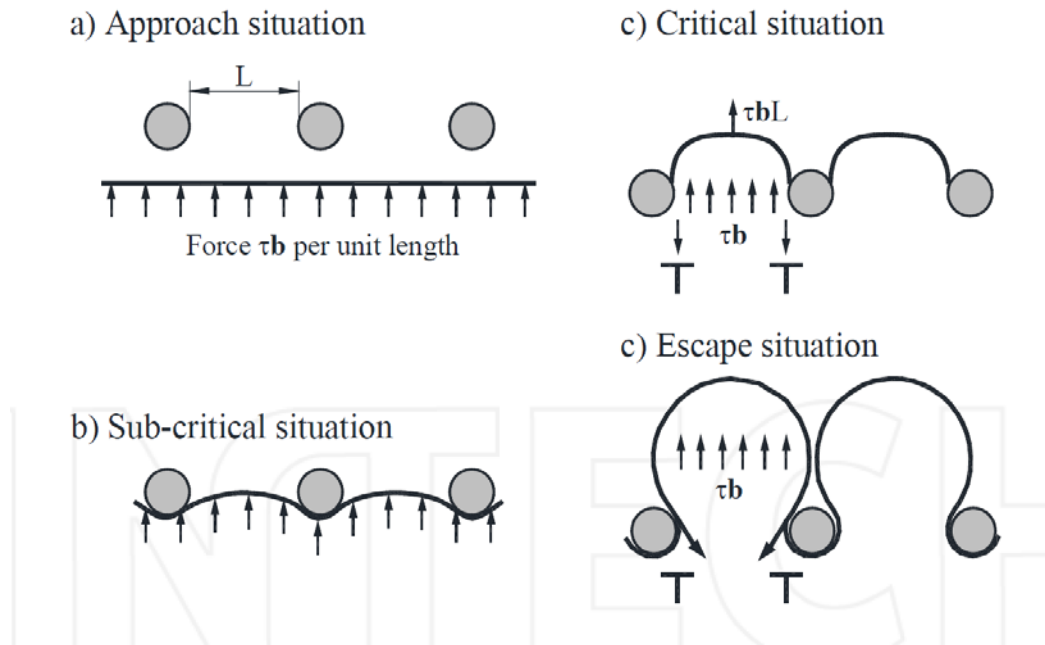
Figure 2.8: The strain mismatch prevents the dislocation from traveling through an incoherent precipitate. Instead, the dislocation bows around the obstacle until the energy applied is enough to break the dislocation line, and leave an Orownan loop and the reformed dislocation on the other side, from [123].
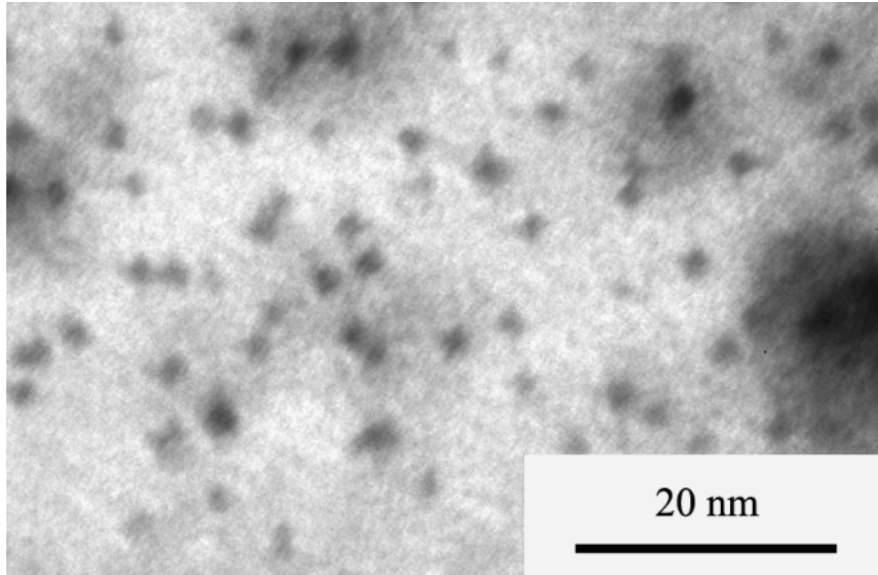
Figure 2.9: A bright field TEM image of the uniform distribution of Yi-Ti-O particles in a 14 Cr ODS steel, from [124]**.**
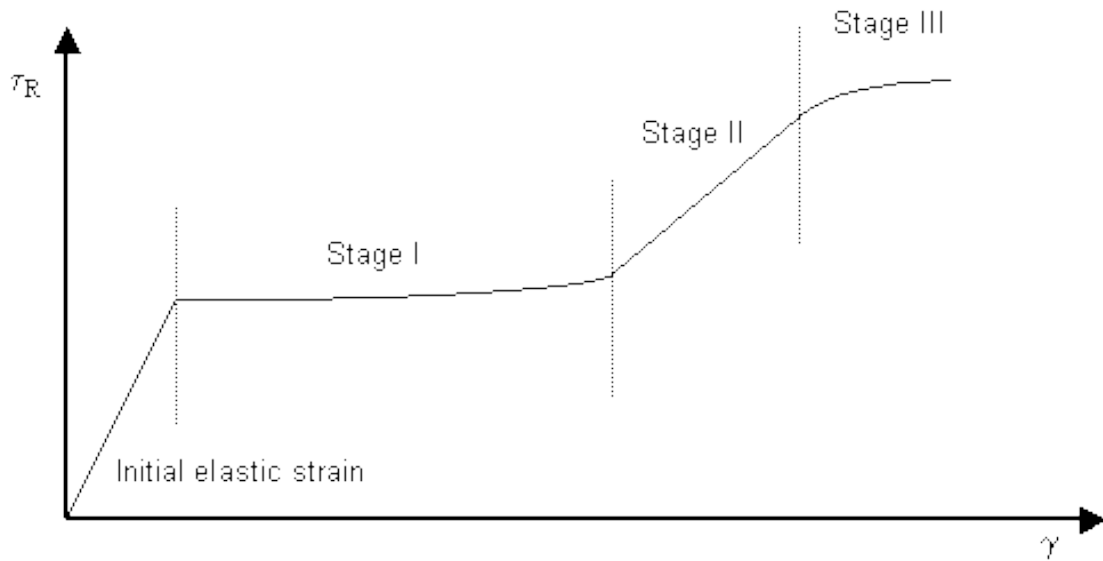
Figure 2.10: Stress vs. strain curve for a single crystal showing the three regions of plastic deformation. Region I has a low dislocation density with few interactions. In Region II the dislocations begin to interact through annihilation or repulsion, resulting in an increasing rate of strain hardening. Region III is characterized by large stresses that allow the repulsive forces associated with the dislocation interactions to be easily overcome, from [125].
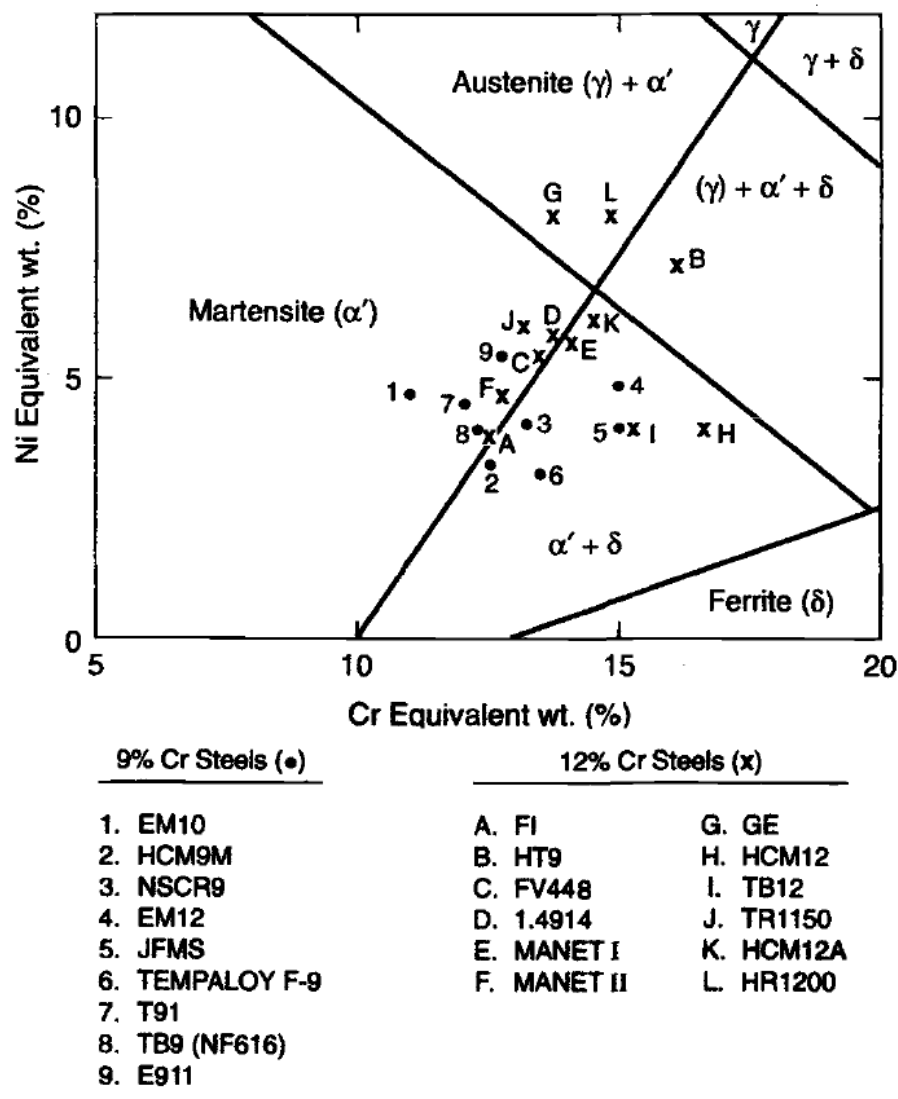
Figure 2.11: Schaeffler-Schneider diagram for 12wt%Cr and 9wt% Cr steels showing the final phases present in the material based on the estimated nickel and chromium equivalents calculated using Equation 2.8 and Equation 2.9 respectively, from [3].

Figure 2.12: Bright field TEM images of a reduced-activation 9 Cr-2WVTa steel showing the grain structure and precipitate formation after tempering, from [3].
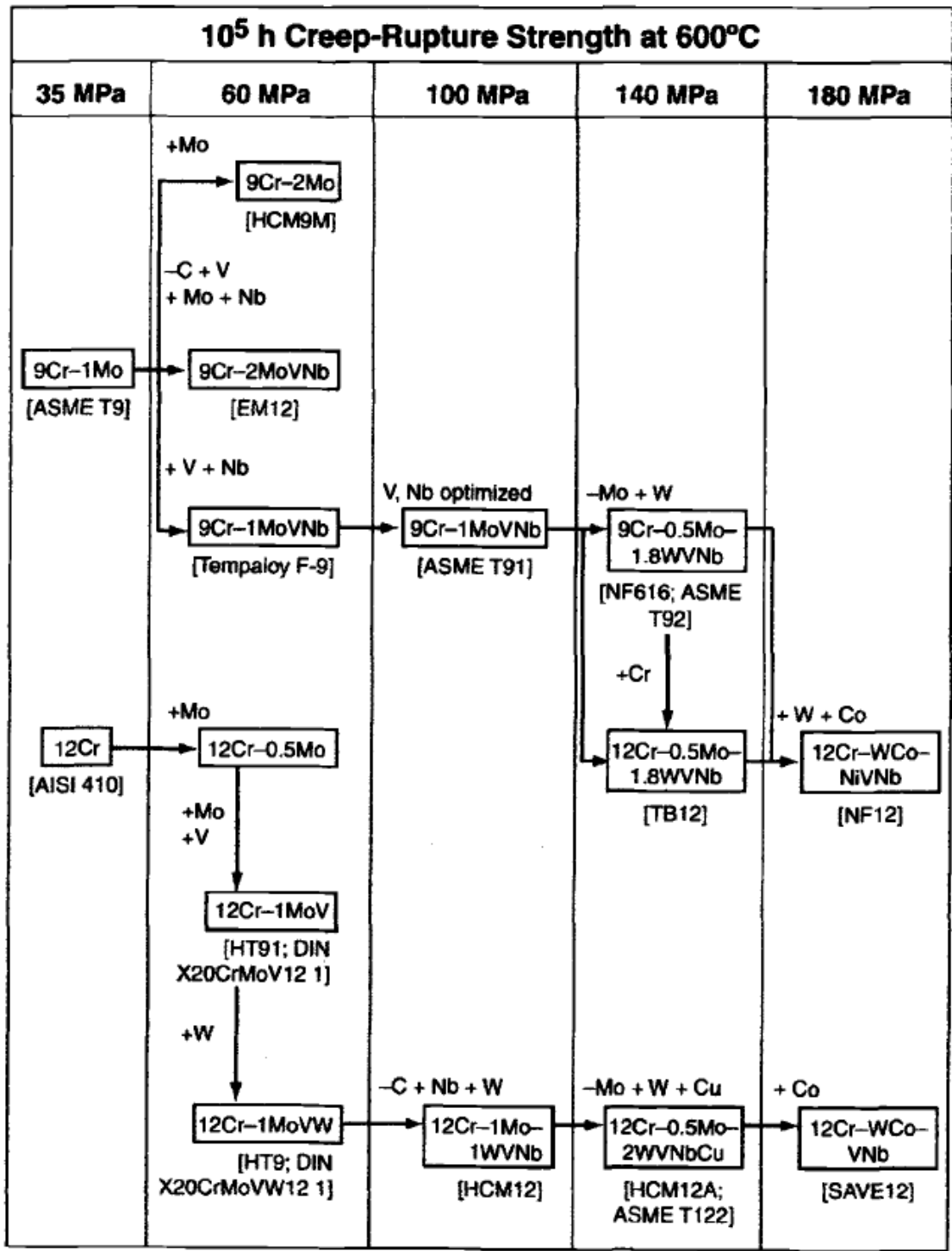
Figure 2.13: **The evolution of ferritic martensitic (F-M) steels in an effort to increase the creep rupture strength, from** [126]**.**
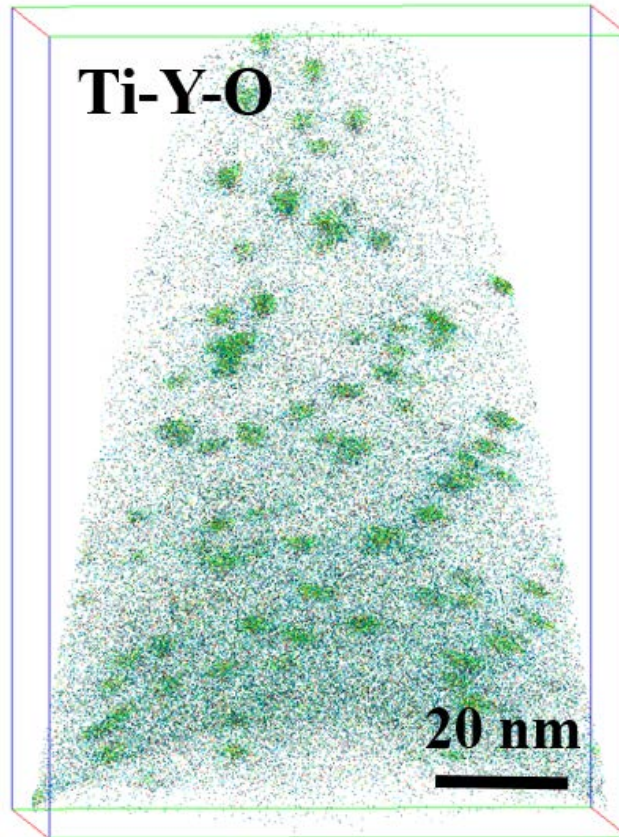
Figure 2.14: Ti-Y-O clusters in ODS alloy showing the reduced oxide size achieved using modern processing techniques, from [6]**.**
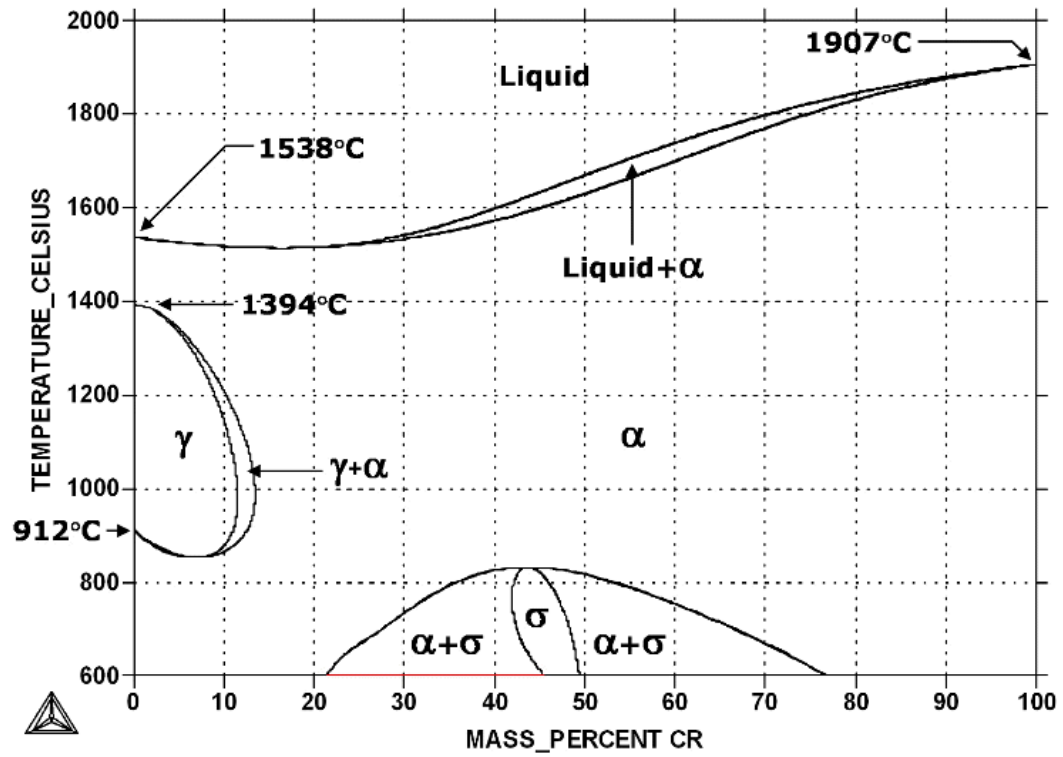
Figure 2.15: The Iron-Chromium phase diagram describing the phases that develop in stainless steels based on the chromium content, from [77]**.**
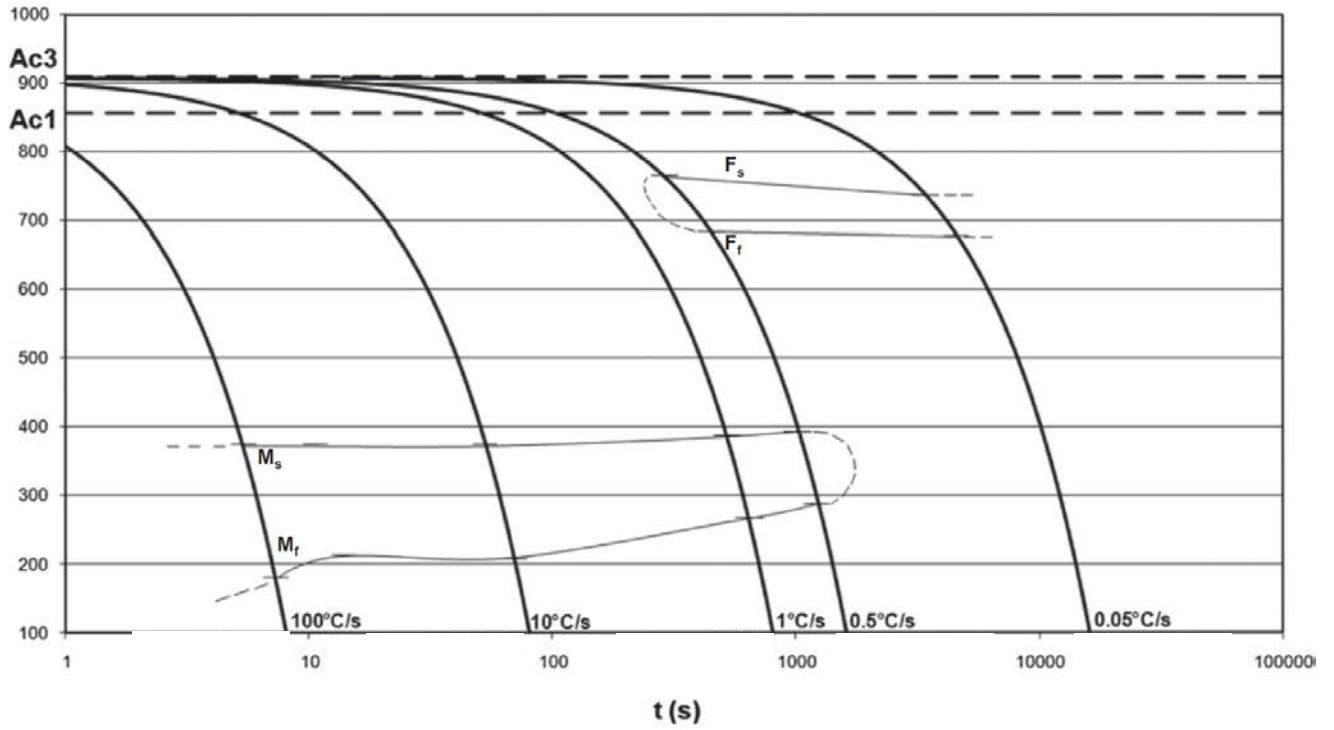
Figure 2.16: CCT diagram depicting the cooling rates required to form martensite, ferrite, or a microstructure that contains both phases based on the martensite start (M_s) and finish (M_f) temperatures and the ferrite start (F_s) and finish (F_f) temperatures, from [22].
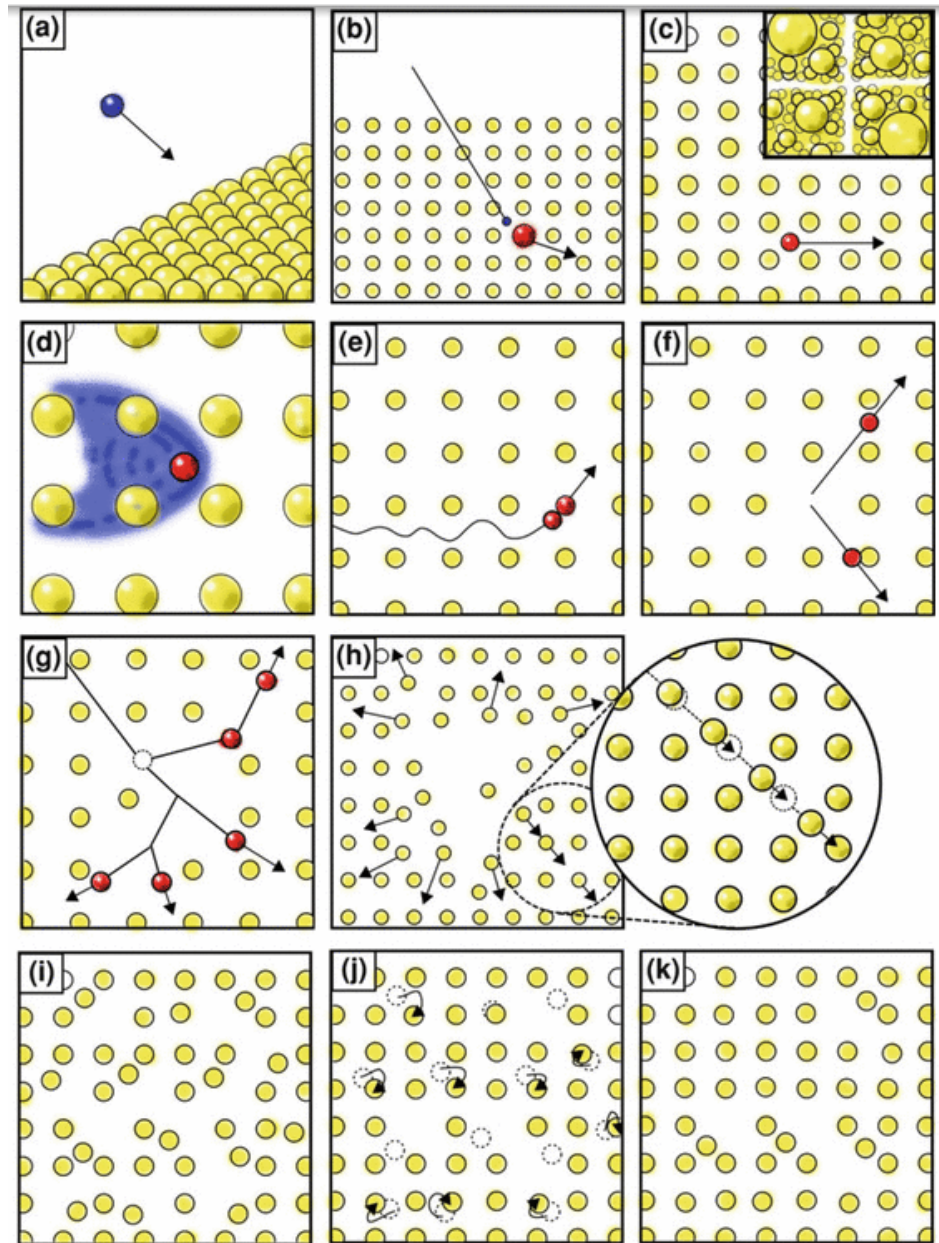
Figure 2.17: **The formation of a damage cascade starting with the incident particle approaching the lattice (a), and creating a primary knock on atom (PKA) that travels through the material (b), (c). Through coulombic interactions (d) or collisions (e) the PKA interacts with the atoms in the lattice creating Frankel pairs until its kinetic energy has been exhausted and it comes to rest in the material (f), (g). The majority of the vacancies and interstitials will recombine (h)-(j) adding to the self-healing properties of the metal, but some will diffuse to defect sinks leaving a damage cascade within the material (k), from [127].**
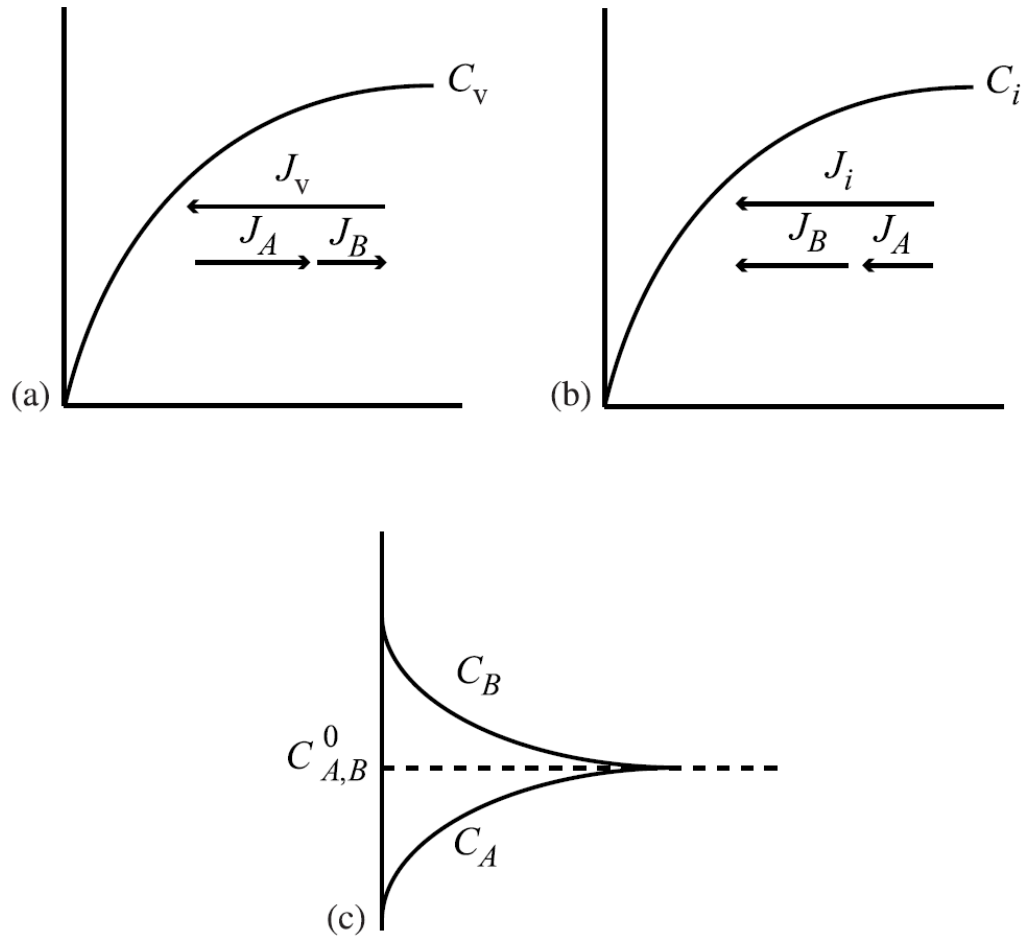
Figure 2.18: Radiation induced segregation (RIS) in a binary alloy described through the inverse Kirkendall mechanism, which describes the enrichment or depletion of an element (c) based on the vacancy flux (a) and the interstitial flux (b) and the flow of the individual element species within each, from [24]**.**
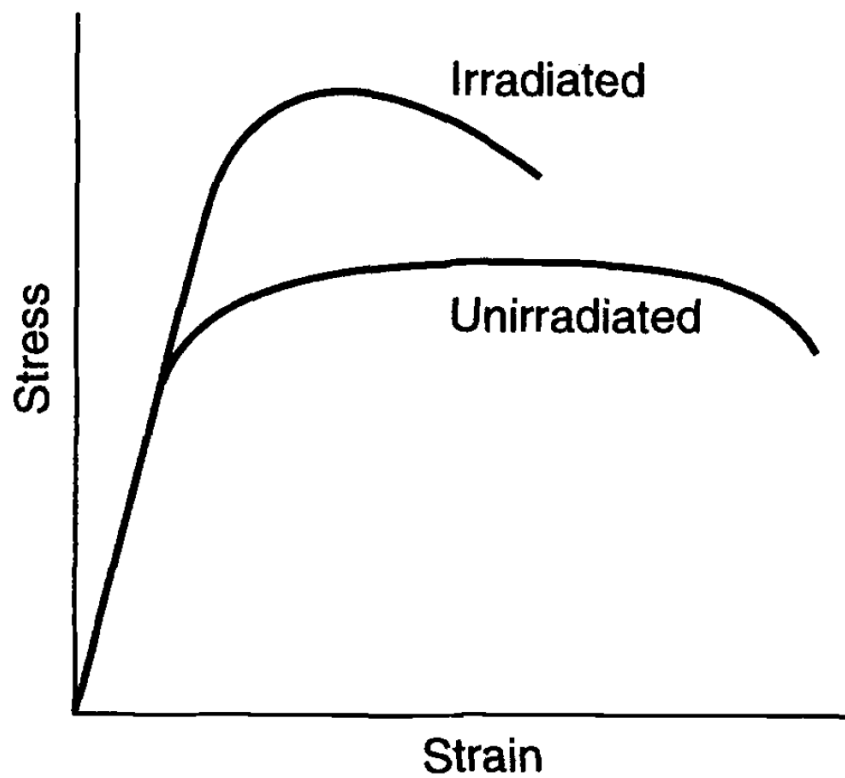
Figure 2.19: The typical stress-strain response in irradiated metals where the yield strength and ultimate tensile strength increase, while the total elongation decreases, from [3]**.**
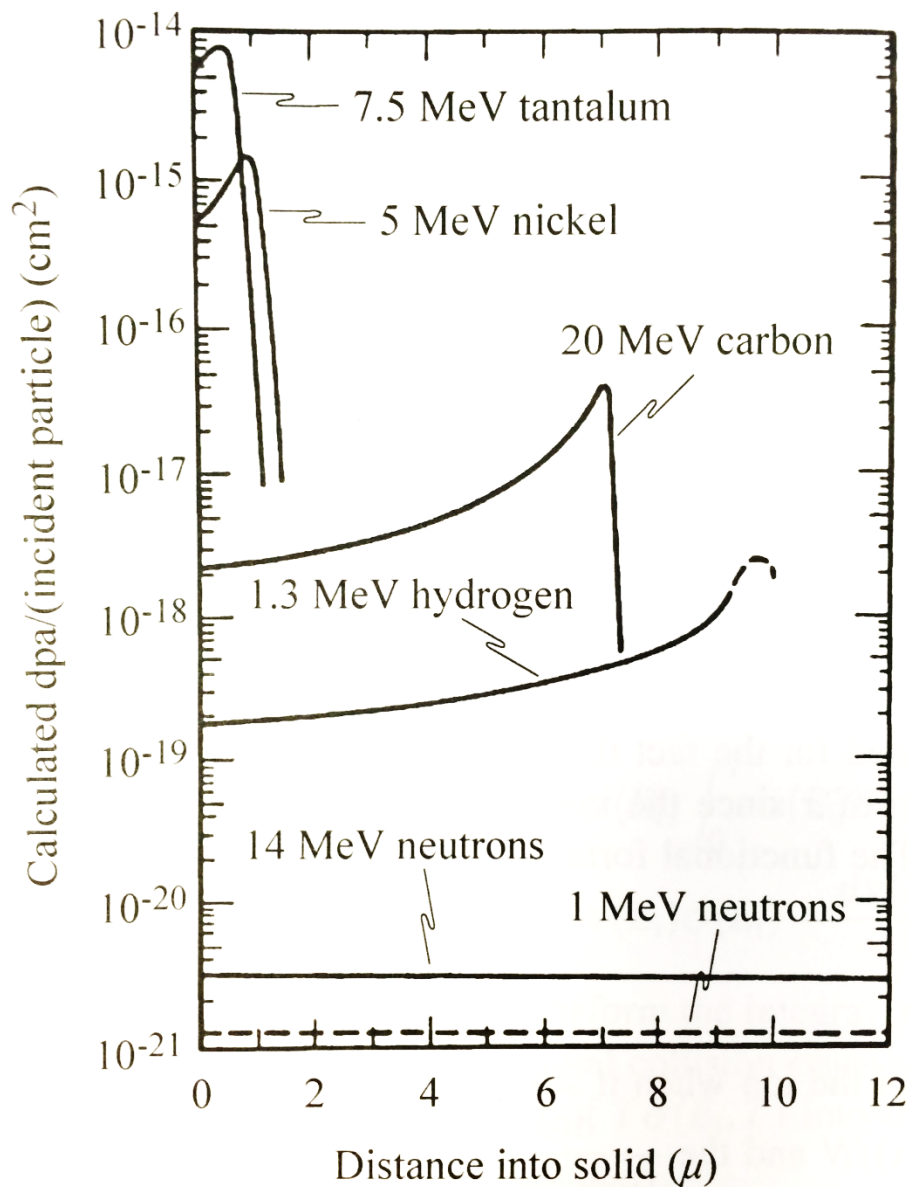
Figure 2.20: Damage profiles for a variety of incident particles in nickel. Notice the heavier the ion the shallower the damage layer, and the uniform nature of neutron irradiations. Proton irradiations are often approximated as uniform based on the relatively constant damage profile as compared to heavy ion irradiations, from [24].
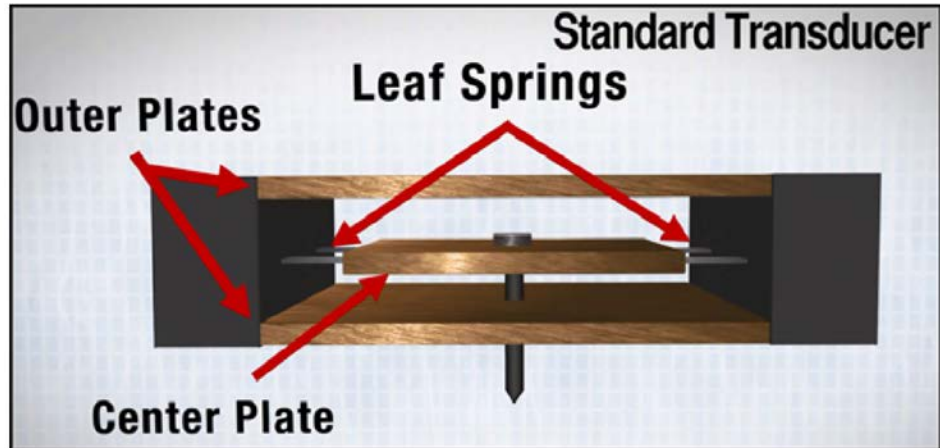
Figure 2.21: A schematic depicting a typical nano-indenter showing the center plate, and outer plates. During indentation a large DC bias voltage is applied to the bottom plate, which attracts the center plate, and attached indenter probe. The applied force is calculated from the calibration of the transducer and the applied voltage. When the desired force or displacement is reached then the voltage is removed, and the leaf springs return the center plate to its original position, from [83]**.**

Figure 2.22: The load displacement curve resulting from nano-indentation, where A, B, and C are the origin, max depth, and residual displacement respectively. h_r is the residual depth of the impression. h_e is the elastic unloading. h_p is the depth of penetration measured from h_s. h_s is a measure of the depth that the edge of the contact area of the indenter penetrates into the sample at maximum load, P_{max}. h_t is the depth from the sample surface at P_{max}. dp/dh is the contact stiffness. Taken from [91].

(a)

(b)

Figure 2.23: **An indentation stress vs. indentation strain diagram for a spherical indenter showing the transition from elastic deformation to a fully developed plastic zone, from** [85]**.**
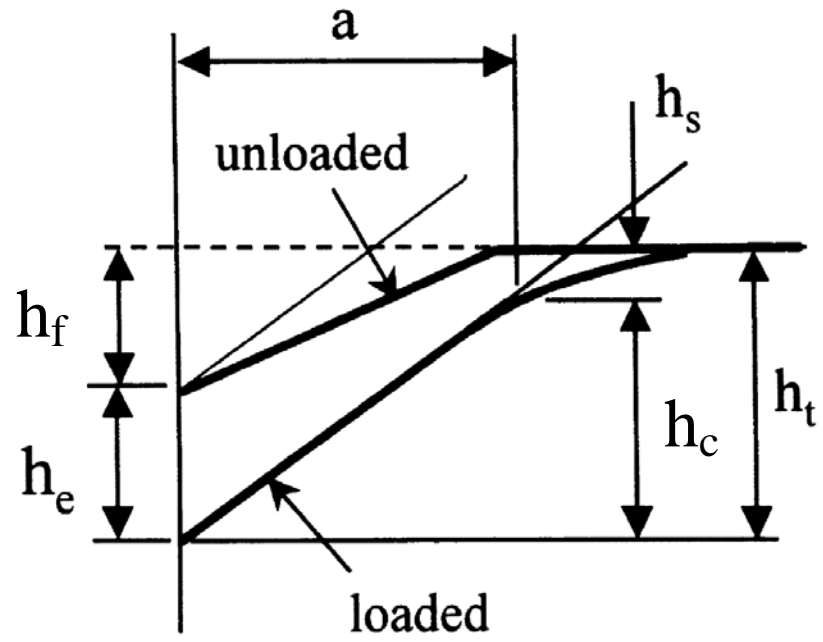
Figure 2.24: **A diagram of a loaded and unloaded indenter depicting the regions of interest as described in Figure 2.22, from [91].**
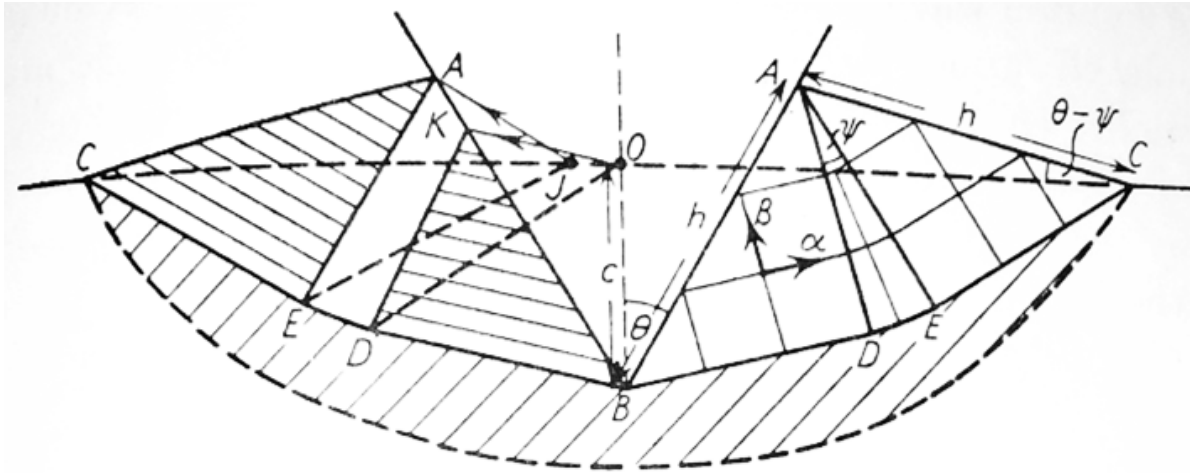
Figure 2.25: **A diagram of the radial plastic zone that develops during indentation showing the slip lines on the right, and the distortion on the left, from [92].**
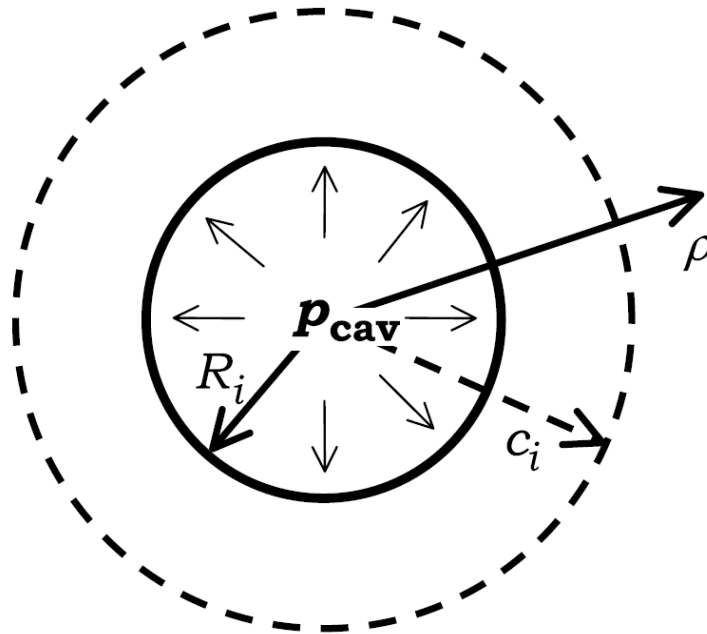
Figure 2.26: The spherical cavity used to model the plastic zone that develops underneath an indent, where p_{cav} is the internal pressure, R_i is the cavity or indenter radius, and c_i is the plastic zone radius, from [94].

$$R=a_s\left(\frac{1+\tan^2\theta}{2\tan\theta}\right)$$
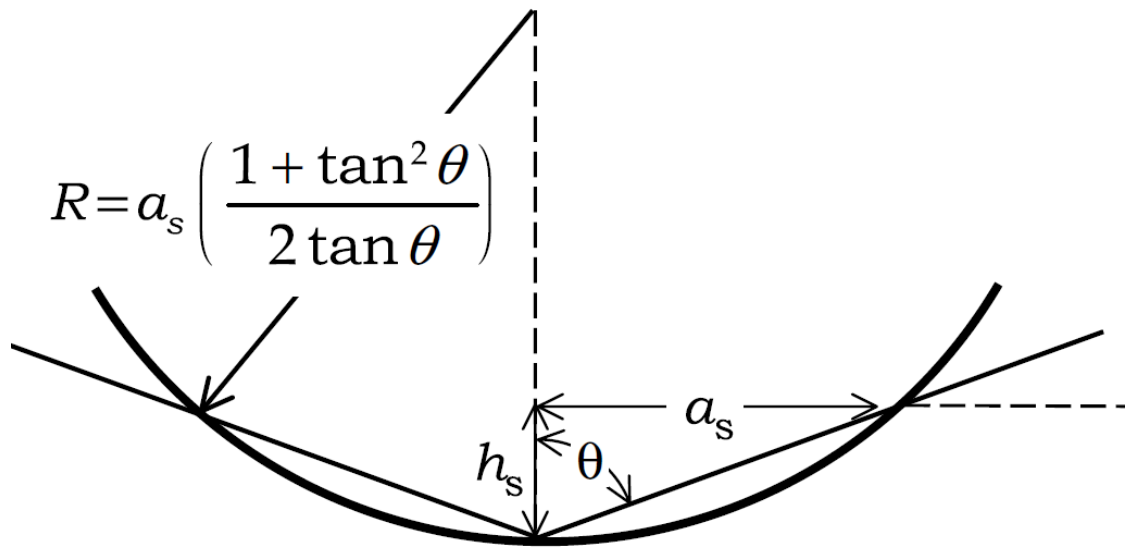
Figure 2.27: A cross section image showing the geometrical relationship where a spherical indenter develops the same plastic zone as a conical indenter, from [94].

$$R = \frac{a_s}{0.635}$$

a_s

h_s

z_{ys}

$$c = z_{ys} + R - h_s$$
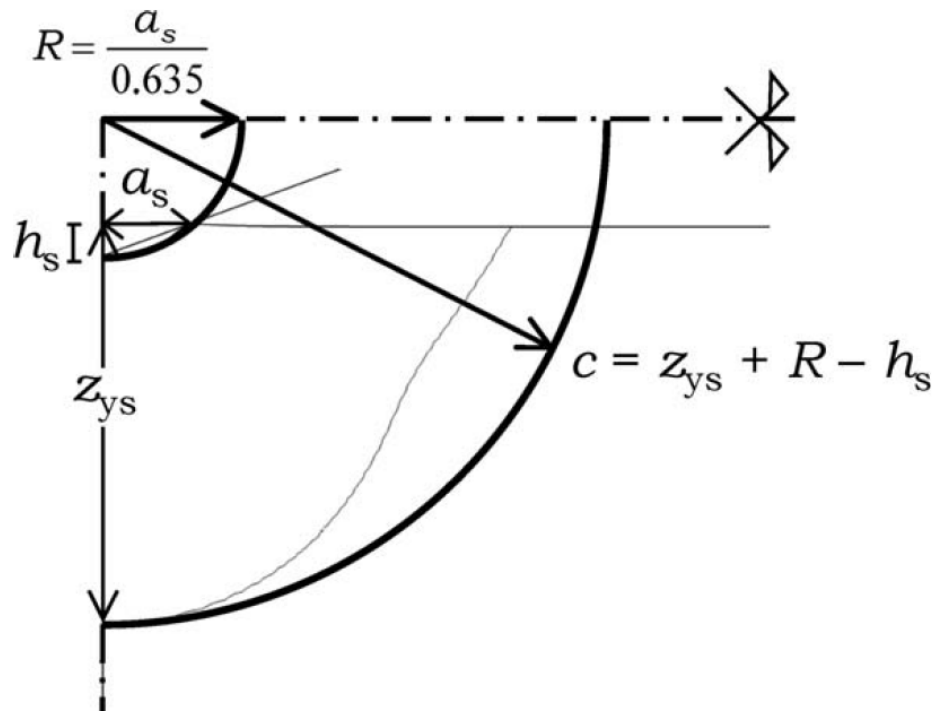
Figure. 2.28: **A diagram depicting how the radius of the plastic zone, c, relates to the contact radius of a spherical indenter, c, the depth directly below the indent, z_{ys}, and the total indentation depth, c. Notice the shape of the plastic zone does not directly follow the plastic zone radius, from [94].**
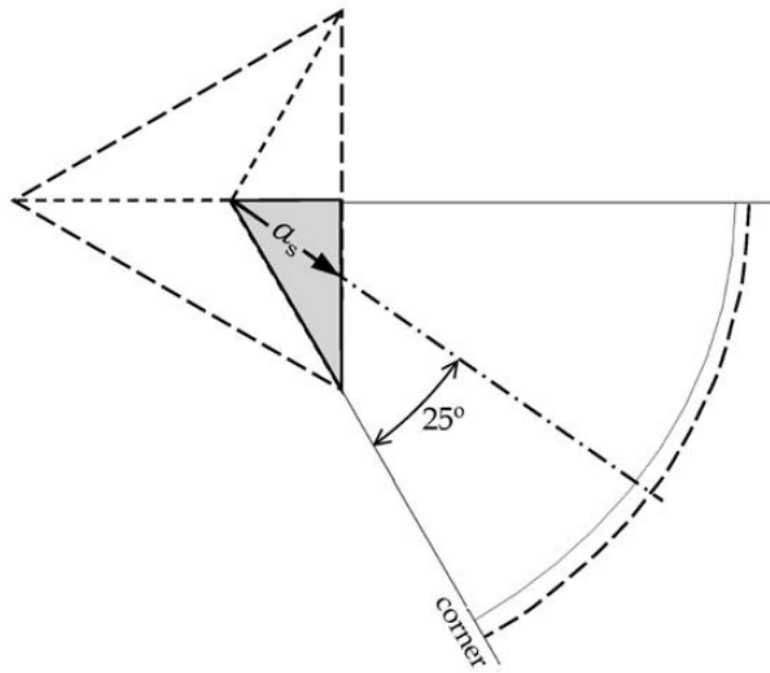
Figure 2.29: A diagram depicting how to measure the contact radius of a Berkovich indentation when evaluating Equation 2.33 and Equation 2.38, from [94].
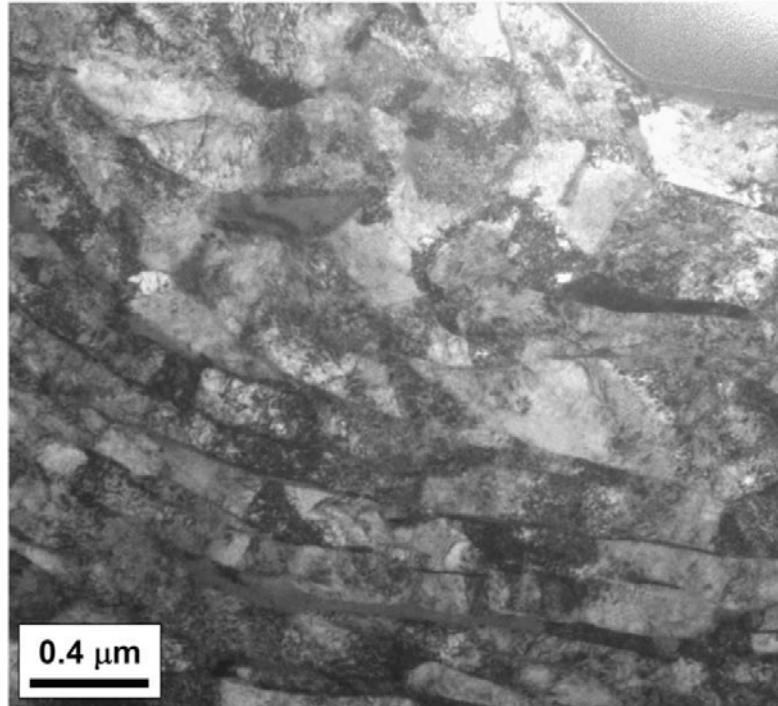
Figure 2.30: A TEM image of the indented plastic zone developed in a polycrystalline Zr-2.5%Nb alloy, from [110]**.**

Sinking-in

Piling-up
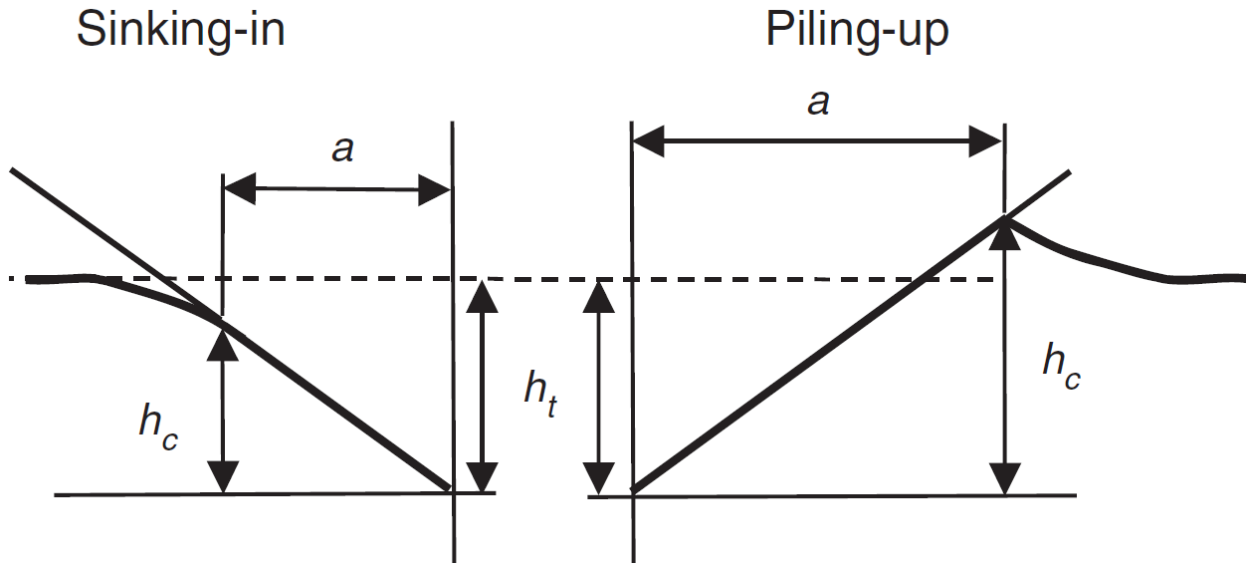
Figure 2.31: A diagram depicting sink-in and pile-up. In sink-in the material buckles under the applied load, and falls out of contact with the tip, while in pile-up the plastic strain field causes the material to be pushed up higher than the original surface of the sample. If sink-in or pile-up occurs then the measured properties will be altered by the load being spread over a smaller, or larger contact area respectively, from [85].
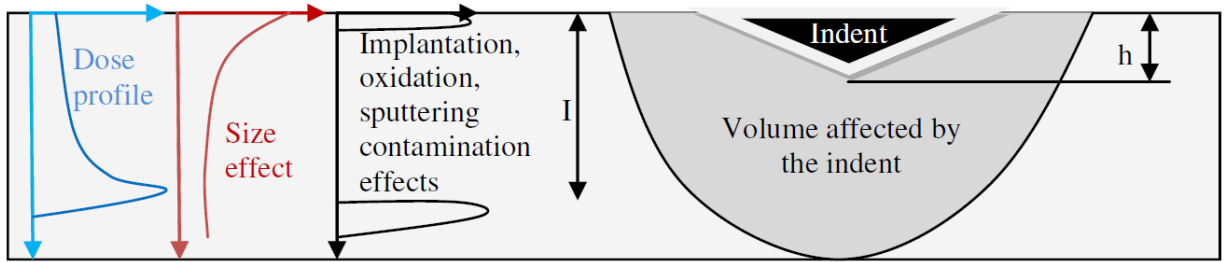
Figure 2.32: Nano-indentation and irradiation effects that must be considered when performing nano-indentation on the ion irradiated samples, from [84]**.**

CHAPTER THREE: OBJECTIVE

The objective of this work is to gain an understanding of how exposure to irradiation alters the mechanical properties of ODS alloys. Experimental work utilizing nano-indentation and TEM imaging will be combined with Mata's spherical indentation model, to calculate an equivalent strain hardening coefficient, which will be used to evaluate the extent of irradiation damage to the alloy. The outcome of this study is three-fold. One, an understanding of how the properties are altered with exposure to irradiation will speak to the appropriateness of utilizing ODS alloys for future reactor designs. Two, knowledge of the plastic zone developed during nano-indentation will provide insight into the suitability of nano-indentation to evaluate the irradiation hardening. Three, discernment of the strain field that develops from nano-indention will provide access to another tool that can be used to evaluate the hardening attributed to the oxides within the matrix, and the irradiation induced precipitates.

A comparison between the tensile properties measured in this study and those measured using methods found in previously published works will used to assess the validity this proposed method. The results of multiple studies were presented in a previous section that show how FEA has become a research standard for investigating the indentation stress field, and that the strain hardening coefficient can be measured through by using multiple tip geometries during nano-indentation. It is hypothesized that nano-indentation using only a single tip geometry can be combined with TEM imaging to predict the same information.

CHAPTER FOUR: EXPERIMENTAL

Chapter four presents the experimental methods used to perform this study. This section will contain discussion of the fabrication of the alloy, irradiation techniques, nano-indentation, and the methods used to for plastic zone imaging.

4.1 ODS Fabrication

The Fe-9wt%Cr oxide dispersion strengthened steel sample originated in lot M16 from the Japan Nuclear Cycle Development Institute, which would become the Japan Atomic Energy Agency in 2005. The chemical composition of the alloy is described in Table 3.1 where the elements were analyzed as follows: The carbon and sulfur were analyzed using infrared absorption, the silicon, phosphorus, and boron were analyzed using absorption spectrophotometry, the manganese, nickel, chromium, titanium, tungsten, and yttrium were analyzed using inductively coupled plasma mass spectrometry, and the oxygen, nitrogen, and argon were analyzed using the inert gas fusion method. The extra oxygen (Ex. O) is the amount of oxygen originally in the Y_2O_3 powder that does not end up in the final oxygen concentration in the steel [128].

Steel rods, of 24 mm in diameter and 60 mm in length, were produced from high purity powders of Fe, Cr, C, W, Ti, Y_2O_3, Fe_2Y, and Fe_2O_3. After ball milling in an attrition-type mill at 220 rpm for 48 hrs in an Ar atmosphere, the powders were degassed at 673 K at 0.1 Pa. They were then hot-extruded at 1473 K and forged at 1423 K. The alloy was heated to 1323 K for one hour and then air cooled to room temperature. The

heat treatment finished with a temper of one hour at 1073 K, again followed by air

cooling to room temperature [128], [129].

4.2 Irradiations

This study compares three irradiation conditions: as received, ion irradiated, and

neutron irradiated. The as received sample was sectioned from the 9wt%Cr ODS alloy

and contains no further treatments, excluding mechanical and chemical polishing. Ion

irradiation took place at 400° C to 100 dpa, while the neutron irradiation was performed

at 500° C to 3 dpa over a period of almost a year.

4.2.1 Ion Irradiation

4.2.1.1 Sample Preparation

A 20mm x 2mm x 2mm bar was cut from the ODS bulk sample using electric

discharge machining (EDM), which uses high frequency sparks to section the material

without any work hardening. The sample was then mechanically polished from 320 to

4000 grit silicon carbide paper. The residual damage layer was removed via

electropolishing in a 10% Perchloric acid, and 90% methanol solution for 20 seconds at -

40° C and a potential of 35 V. A magnetic stirring bead is used to create turbulence that

removes the oxygen bubbles from the surface of the sample, and prevent pitting. Baths in

acetone and then methanol are used to halt the acid reaction, and a ultrasonic bath in ethyl

alcohol removes any surface debris [130].

4.2.1.2 Irradiation Parameters

Irradiation with 5.0 MeV Fe^{++} ions was done at a vacuum less than 10^{-7} torr using

the General Ionex Tandetron accelerator at Michigan Ion Beam Laboratory. The sample

was mounted on an electronically isolated copper stage that was attached to the

accelerator beam line. The temperature was held at 399.3° ± 4.4° C, while the sample

was irradiated at a dose rate of approximately 10^{-3} displacements per atom (dpa) per

second until the target of 100 dpa was reached at a depth of 600 nm, as measured via the

beam current. Temperature was monitored using thermocouples that were spot-welded

onto the sample and fed into a 2D infrared thermal pyrometer that recorded the

temperature at a frequency of 0.1 Hz during the irradiation. Heat control was provided

by an indium liquid filled shim that was placed between the sample and the stage that was

combined with resistance heating and air cooling to provide a constant irradiation

temperature.

4.2.1.3 Irradiation Damage

The peak damage location, peak ion deposition depth, and the ion stopping range,

were originally calculated using the Stopping and Range of Ions in Matter (SRIM)

2013™ program with the detailed calculation from full damage cascades, and were 1.24,

1.38, and 1.92 μm, respectively. The peak damage is 255 dpa, but at a depth of 600nm

from the surface, an approximately linear region in the damage profile allows a more

accurate correlation of irradiation damage to material properties. The displacement

damage at this depth was determined to be 100 dpa. Resent work by Stoller et al.

reported that the quick calculation of damage is a more accurate modeling method to

predict the extent of ion irradiation damage [131]. An ion distribution and quick

calculation of damage was performed with 999,999 incident Fe ions at 5 MeV and an

angle of incidence normal to the surface. The target layer consisted of a 2 μm thick

90%Fe and 10%Cr single layer, with each element having a displacement energy of 40

eV, in accordance with the values reported by Was [24]. The density was adjusted to 7.73 g/cm^3 as measured by Auger et al. [18].

The updated quick calculation resulted in the peak damage location, peak ion deposition depth, and thickness of irradiation layer remaining the same at 1.28, 1.38, and 1.92 μm, respectively. The peak dpa was recalculated to be 123, and at the target depth of 600 nm the damage was 52 dpa. The damage and ion range profiles are shown in Figure 4.1.

4.2.2 Neutron Irradiation

4.2.2.1 Sample Preparation

The neutron irradiated sample was cut into 3mm diameter discs that were 150 to 200 μm thick, and mechanically polished through 4000 grit silicon carbide paper. The sample was then electropolished using a 10% Perchloric acid and 90% methanol solution at -30° C to remove residual plastic deformation.

4.2.2.2 Irradiation Parameters

The sample was irradiated at Idaho National Laboratory, INL, in the Advanced Test Reactor (ATR) as part of a Pilot Project for the Advanced Test Reactor National Scientific User Facility in 2008. It was exposed to a fast neutron flux with a dose rate of approximately 10^{-7} dpa/s. An irradiation temperature of 500° ± 50° C was monitored using electrically sensitive silicon carbide samples that were mounted in the same capsules. The irradiation continued until a uniform dose profile of 3 dpa was reached [6], [132].

4.3 Nano-Indentation

Nano-indentation experiments were performed at the Center for Advanced Energy

Studies (CAES) in their Microscopy and Characterization Suite (MaCS) on a Hysitron

TI-950 Triboindenter. Testing was performed on each of the irradiation conditions to

create a depth profile of the nano-hardness and nano-modulus.

4.3.1 Sample Preparation

Nano-indentation is highly sensitive to surface effects. A rule of thumb used in

nano-indentation is that the minimum indentation depth should be 10x the surface

roughness of the sample. In an effort to standardize the samples the as received and

neutron irradiated samples were mechanically and electro-chemically polished to provide

uniform indentation surfaces. Restrictions on nuclear handling prevented the samples

from being polished at the same locations, but every effort was made to prevent deviation

in surface roughness. The ion irradiated samples was not polished to prevent damage to

the irradiated layer.

4.3.1.1 As Received

A 0.25" section of the bulk as received sample was mechanically removed using

an Allied Techcut 4™ diamond saw. The size of the sample was chosen to provide

contact area for the electrical connections that are required for electro-chemical polishing.

Initially the sample was mounted to a glass polishing slide by heating a hot plate to a

temperature that would cause the Crystalbond™ resin wax to melt. Once the wax had

cooled, and the sample bonded to the glass plate, an Allied-M prep B™ polishing wheel

was used to mechanically polished through 1200 grit silicon carbon paper. Buehler

MetaDi™ PolyCrystalline Diamond Suspension was then used to mechanically polish the

sample through 0.05 μm with diamond slurries. Electropolishing was performed to remove the surface damage layer in a 10% Perchloric acid solution at the University of Michigan. Figure 4.2 a) shows the surface of the sample, with an average surface roughness measured to be 58 nm using the Hysitron TI-950 TriboIndenter with a scan rate of 1.00 Hz, a tip velocity of 80.000 μm/s, a set point of 0.5μN, and an integral gain of 240. The peak to valley height was 291 nm.

4.3.1.2 Ion Irradiated

To protect the integrity of the irradiated surface, the ion irradiated sample was not polished prior to nano-indentation. This prevented the loss of the any shallow irradiated material, and allowed for isolation of irradiated hardness from the unirradiated bulk substrate. However, sputtering of the surface during irradiation left the sample with average surface roughness of 100 nm and a peak to valley height of 732 nm, as measured with the Hysitron TI-950 TriboIndenter when using the same setting as previously described. The surface of the sample is shown in Figure 4.2 b).

4.3.1.3 Neutron Irradiated

The sample that underwent neutron irradiation was allowed to cool, and then electropolished at INL in a 5% Perchloric acid solution at -45° C for five seconds using a Southbay Model 550 electropolisher at 80V and 70mA. The average surface roughness was measured to be on the same scale as the as received sample with an average surface roughness of 52 nm, and a peak to valley height of 245 nm, using the Hysitron TI-950 TriboIndenter with previously described settings. The surface is shown in Figure 4.2 c).

4.3.2 Testing

    4.3.2.1 TI-950 TriboIndenter

The Hysitron TI-950 TriboIndenter was used to perform the nano-indentation required for this study. The TI-950 TriboIndenter provides to option of using either a high or a low load transducer. The low load transducer is attached to a Berkovich probe with a contact radius of 20 nm, while the high load transducer is attached to a Berkovich probe with a contact radius of 250 nm. These two transducer options allow for investigating the shallow surface, and the deeper irradiated layers.

The transducer is mounted on a piezo stack, shown in Figure 4.3, containing piezoelectric ceramics in a tube configuration. The top half of the TriboScanner tube contains four piezos that control a single direction: +X, +Y, -X, and –Y. The bottom half is a single piezo used to control motion in the ±Z direction. Energizing a specific X or Y piezo results in the lengthening of that component, causing the stack to bend in the appropriate direction, while if the Z piezo is energized the lower region of the tube extends.

To provide vibration isolation, the system is mounted on top of a Herzan™AVI-350 S/LP active vibration isolation system. A granite base is attached to two control platforms that each contain four piezo-electric accelerometers that monitor vibration. Four electro-dynamic transduces are able to produce offsetting forces that dampen out the external vibrations.

The sample is mounted on a magnetic stage that is capable of moving along the X, Y, and Z-axis, which allows for coarse positioning of the transducer stack, as verified by

an optical system consisting of a 20x objective lens in series with CCD camera. The

optical system, shown in Figure 4.4, provides up to 220x magnification [83].

4.3.2.2 Determining Sample Size

The sample size was determined assuming a normal distribution, with a desired

95% confidence level and a 5% margin of error in nano-hardness, using the following

equation:

$$n = \left(\frac{z_{\alpha/2}\sigma}{E}\right)^2 \qquad\qquad \textbf{Equation 4.1 } [133]$$

where n is the sample size, $z_{\alpha/2} = 1.96$ is the critical z score for a 95% confidence level,

σ is the standard deviation, and E is the desired margin of error. Individual sample sizes

were calculated for each condition based on the standard deviation of the nano-hardness

as determined in a preliminary study. The required sample sizes are: 16, 9, and 9 for the

ion irradiated, neutron irradiated and as received samples respectively, with the higher

sample size of the ion irradiation condition due to its distinct surface roughness. Data

from depths less than 200 nm were not considered due to tip effects skewing the

distribution.

The sample sizes were met or exceeded for most of the indentation depths.

However limitations in the sample area on the neutron irradiated sample provided limited

statistics for the 600 and 900 nm depths after the removal of statistical outliers. The

associated confidence level for these depths exceeds 90%.

4.3.2.3 Calibrations

Prior to indentation a series of calibrations are performed to ensure the accuracy

of the measured parameters.

An indentation axis calibration was used to correct for variations in the electrostatic force within the three-plate capacitive transducer that occur due to changes in temperature or humidity. Also known as an "air calibration," this was done daily to account for current conditions. The load function was adjusted so that the Peak Force was be between 600 and 800 μN, and a displacement was approximately 3-4 μm. These settings provided enough movement to verify the operation of the transducer prior to testing.

A probe calibration was performed prior to testing to account for any changes in probe geometry during normal operation of the equipment. An array of indents of varying applied loads was performed utilizing a load function with a 5 second loading time, 2 second hold time, and a 5 second unloading time, on a fused quartz sample with a known hardness and elastic modulus of 9.25 GPa and 69.6 GPa, respectively. The minimum load used should create a contact depth lower than required for the experiment, and the maximum load should be close to the force limit of the transducer. The contact area was then calculated as described in Section 2.3.4. Probe area calibrations were performed for each mounting method.

The system compliance will vary depending on the probe, transducer, and mounting method that is used. However, the machine compliance can be assumed constant for each probe. This allows for the compliance correction to be accounted for with contact area corrections found in the probe area calibration [83].

4.3.2.4 Sample Mounting

The TI 950 TriboIndenter located at MaCS Lab at the CAES facility is designated for use with irradiated materials. To prevent cross contamination between irradiated and

non-irradiated samples different mounting methods were required. Loctite™ super glue was used to adhere both the ion irradiated bar and the as received sample to a magnetic puck. The magnetic stage then held the puck in location during indentation testing. The neutron irradiated sample was glued to a radiologically controlled SEM stub using Loctite™ super glue. The stub was loaded in a mount with a 1" base, which was glued to the magnetic puck. Diagrams depicting the mounting geometries for each condition are shown in Figure 4.5.

4.3.2.5 Parameters

A series of indents were performed in displacement control mode to depths ranging from 100 to 1100 nm at intervals of 100 nm, with a contact threshold of 250 μN. A three segment loading curve was defined with a 20 second loading period, five second hold period, and 20 second unloading period that was verified, through analysis of the unloading curve, to reduce creep effects. A separation distance of 60 μm was used as a buffer between indents to prevent plastic zone interactions. The nano-hardness and elastic nano-modulus were calculated using the Oliver Pharr method, and the statistical outliers were removed.

4.3.2.6 Data Analysis

Indentation in displacement control is a less consistent method of testing than load control, due the additional feedback loop required to control the displacement. Often the response is too slow to prevent the transducer from overshooting the intended depth. To address this issue each data point was manually zeroed prior to performing any data analysis.

For each irradiation condition, the data was grouped according to indentation depth, and statistical outliers were removed prior to calculating the average nano-hardness, and nano-modulus. Statistical outliers are common in nano-indentation experiments due to low tolerances for surface debris, and imperfections that alter the contact area for an individual indent. Statistical analysis was done by sorting the data from smallest to largest, and calculating the five number summary for each depth: minimum, Q_1, median, Q_3, and maximum values. Q_1 and Q_3 are the first and third quartiles, or the numerical values that are 25% or 75% of the average of the measured parameter, respectively. The difference between Q_3 and Q_1 is known as the interquartile range, IQR, and outliers are calculated from the following relationships:

$$High\ Outlier \geq Q_3 + 1.5 \times IQR \qquad \textbf{Equation 4.2}\ [133]$$

$$Low\ Outlier \leq Q_1 - 1.5 \times IQR \qquad \textbf{Equation 4.3}\ [133]$$

A data point was not used in this study if either its nano-hardness or nano-modulus values were considered statistical outliers, or if the shape of the force displacement curve indicated a flaw occurred during testing [83], [133].

4.4 Plastic Zone Imaging

<u>4.4.1 Sample Prep</u>

TEM samples were created using a FEI Quanta™ 3D FEG Focused Ion Beam (FIB) located in MaCS Lab at CAES. This allowed for precise location control ensuring the center of the indents were contained within the TEM thin films used to image the plastic zone. The steps used to create the cross section lift-outs are as follows:

Initially the indents were located on the surface of the sample, using the electron beam imaging at 10 kV, and .33nA. This prevented damage to the surface of the sample.

The indents selected for imaging, shown in Figure 4.6, have indention depths of 500, 600, and 700 nm for the as received, neutron irradiated, and ion irradiated samples respectively. SEM images demonstrating the steps required to create a TEM lamella in the FIB are shown in Figure 4.7, and presented below. Once the initial location was located, shown in Figure 4.7 a), a 300 nm layer of platinum was deposited using the electron beam at 5.0 kV and 2.0 nA to further protect the indent surface. The ion beam at 30 kV and .50 nA was then used to fill the indent with platinum to provide a flat starting surface to work from. The same settings were then used to deposit a 4 μm sacrificial layer to prevent surface damage during the thinning process, which is shown in Figure 4.7 b). With the surface protected it was then time to remove the TEM lamella from the sample.

All cutting was done using the silicon setting and a voltage of 30 kV. 15 μm deep trenches were done using the ion beam at 15 nA at 53.5° and 50.5° for the bottom and top trenches, respectively. The regular cross section tool was used in multi-scan mode, utilizing four multi-passes and a scan ratio of one to minimize the cutting time, with the resulting trenches shown in Figure 4.7 c) and d). Cleaning cross sections were then used at 7.0 nA and a depth of 7 μm to create smooth bottom and top edges again at 53.5° and 50.5° respectively. The U-cuts were performed at a tilt of 0° and a current setting of 5 nA using the rectangle tool to remove the bottom and sides. The top of one side was excluded to create a bridge securing lamella to the sample, as depicted in Figure 4.7 e). Once all the material was removed, the sample was tilted to 53.5° and a cleaning cross section was used to remove any re-deposited material from the backside. The Omni probe was then inserted and attached to the lamella using platinum welds at 30 kV and

50 pA. Once the probe was welded to the sample the support bridge was cut using a 5 nA rectangle cut, and a platinum weld at 50 pA was used to attach the sample to a TEM grid. The probe was then removed using a 1 nA silicon rectangle. An image of the sample mounted on the TEM grid prior to thinning is presented in Figure 4.7 f).

The final step was to thin the sample until it was approximately 100 nm thick. Cleaning cross sections were used at 30 kV and 3.0 nA at 53.5° and 50.5° for the bottom and top sides respectively. The bottom side was thinned until the curtaining effect was removed, and then an equal number of cycles was performed on the back side to provide uniform thinning. These current and voltage settings were used until the sample was approximately 1000 nm thick. Once that thickness was achieved the current was reduced to 1 nA, and the process was repeated until the sample was 500 nm thick. The current was again reduced to 0.3 nA, and the process repeated until the sample was 250 nm thick. At this point, the current was changed to 0.1 nA, and the process repeated until the sample was 100 nm thick. Final polishing was done at current and the voltage settings of 5.0 kV and 77 pA to remove any residual gallium damage from the surface. The rectangle setting was used in five minute intervals alternating top and bottom sides at 45° and 59° respectively, until a hole formed in the sample. The formation of the hole provided indication that the sample was adequately thin for TEM imaging. The final step was to do a one minute polish at 2.0 kV and 48 pA at both 59° and 45° to further remove any residual gallium damage, with the final thinned sample being shown in Figure 4.7 g). Notice the hole formation on the right side of the lamella.

4.4.2 Transmission Electron Microscopy

Bright field TEM imaging was performed on a FEI Tecnai TF30-FEG STwin STEM located in MaCS Lab at CAES. When operated at 300 kV the point to point resolution of the microscope 0.19 nm. Prior to imaging the sample was mounted into a FEI single tilt holder and plasma-cleaned in a Fischione Model 1020 plasma cleaner to remove any hydrocarbons from the sample. Digital Micrograph was used for image collection and plastic zone analysis bases on defect contrast and grain boundary orientation.

4.4.3 ASTAR Imaging

The diffraction patterns collected with TEM imaging provide information on the orientation and crystal structure of the sample material. NanoMegas has developed an automated crystal orientation mapping tool, known as ASTAR™, that is able map the Bragg spot patterns to chart crystal orientation and phase. The DigiSTAR™ unit uses magnetic coils to precess the electron beam to average the dynamical effects out of the image. A diagram of the system is shown in Figure 4.8. An externally mounted CCD camera records the diffraction patterns which are compared with the Index patterns created by the ASTAR. In this work ASTAR was used to assess the applicability of using orientation mapping to image plastic deformation in nano-grained polycrystalline material [134].

A spot size of 9, which is equivalent of a 5 nm beam diameter, a camera length of 89 mm, and a precession angle of 0.6° was used for imaging. Scans of 600 points in the x-direction and 500 points in the y-direction covered the plastic region, and step widths of 50 nm were used to reduce scanning time. The diffraction patterns collected by the

CCD camera were compared against those created using the indexed data for a 92wt%Fe and 8wt%Cr alloy with the crystal structure described by space group 229, Im$\bar{3}$m, provided in Pearson's Crystal Data. The lattice parameter was modified to be .288 nm as measured using a Bruker AXS D8 Discover X-Ray Diffractometer (XRD), located in the Boise State Center for Materials Characterization.

Table 4.1: The chemical composition of the 9 Cr ODS alloy when received from the Japan Nuclear Cycle Development Institute, from [129]**.**

	Chemical Composition (wt%)														
	C	Si	Mn	P	S	Ni	Cr	W	Ti	Y	O	N	Ar	Y_2O_3	Ex. O
Spec	0.11 - 0.15	≤0.20	≤0.20	≤0.02	≤0.02	≤0.20	8.6 – 9.4	1.8 – 2.2	0.20 – 0.24	0.26 - 0.29	0.15 – 0.25	≤0.07	≤0.007	0.33 – 0.37	0.04 – 0.09
Target	0.13	-	-	-	-	-	9.0	2.0	0.22	0.275	0.20	-	-	0.35	0.06
Analysis	0.14	0.048	0.05	<0.005	0.004	0.06	8.67	1.96	0.23	0.27	0.14	0.017	0.004	0.34	0.07
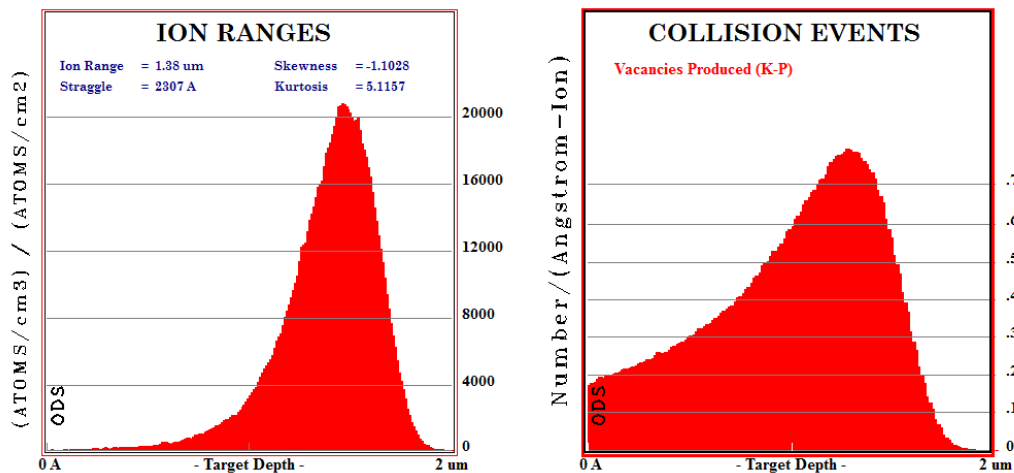
Figure 4.1: The penetration depth and damage profile of the 5.0 MeV Fe^{++} irradiations performed on the 9 Cr ODS alloy at 400° C as calculated with SRIM 2013™ program using the K-P model.

a)

b)

c)
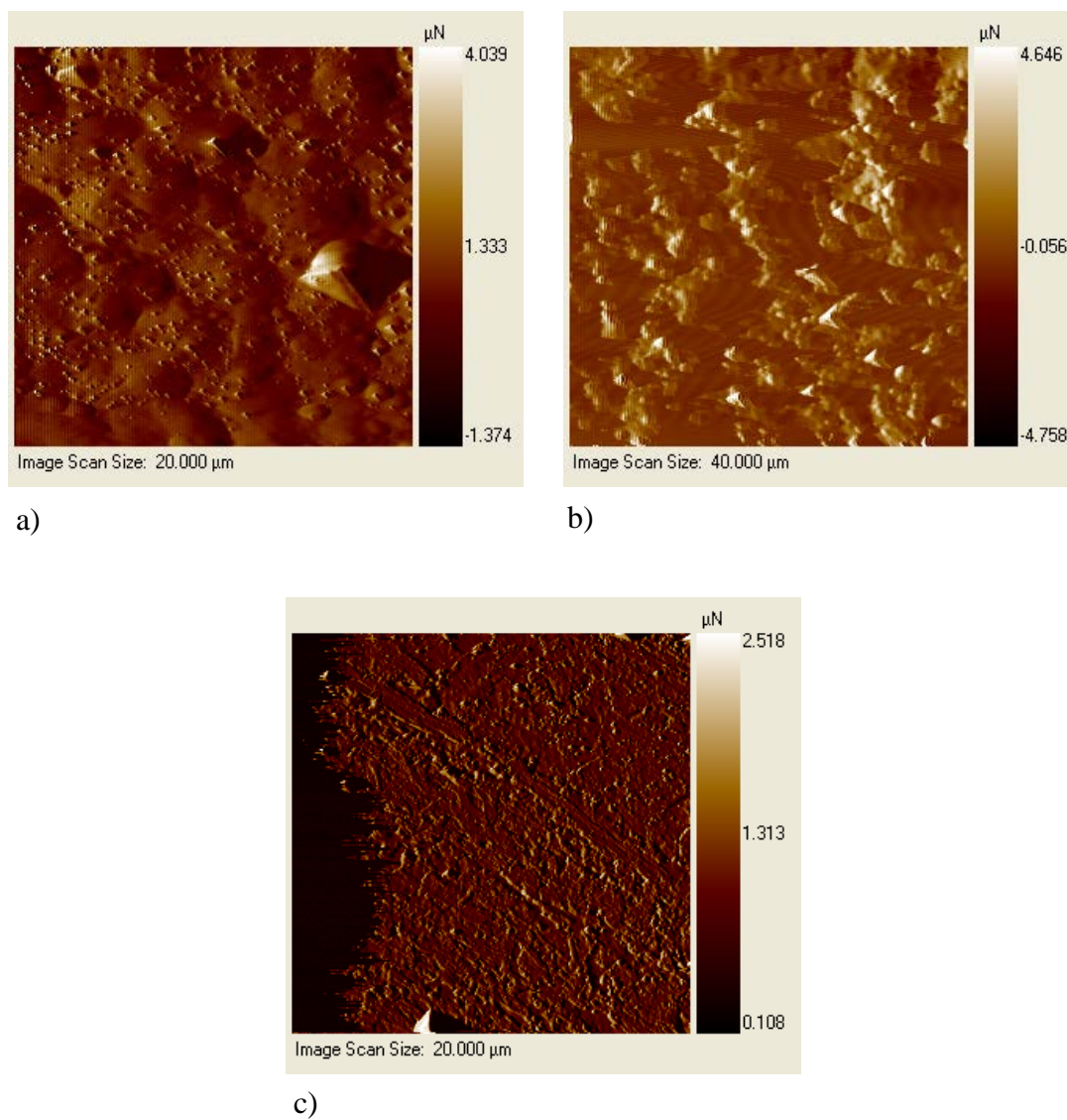
Figure 4.2: The surface area imaged using the atomic force microscopy capabilities of the Hysitron TI-950 TriboIndenter: a) as received, b) ion irradiated, and c) neutron irradiated.
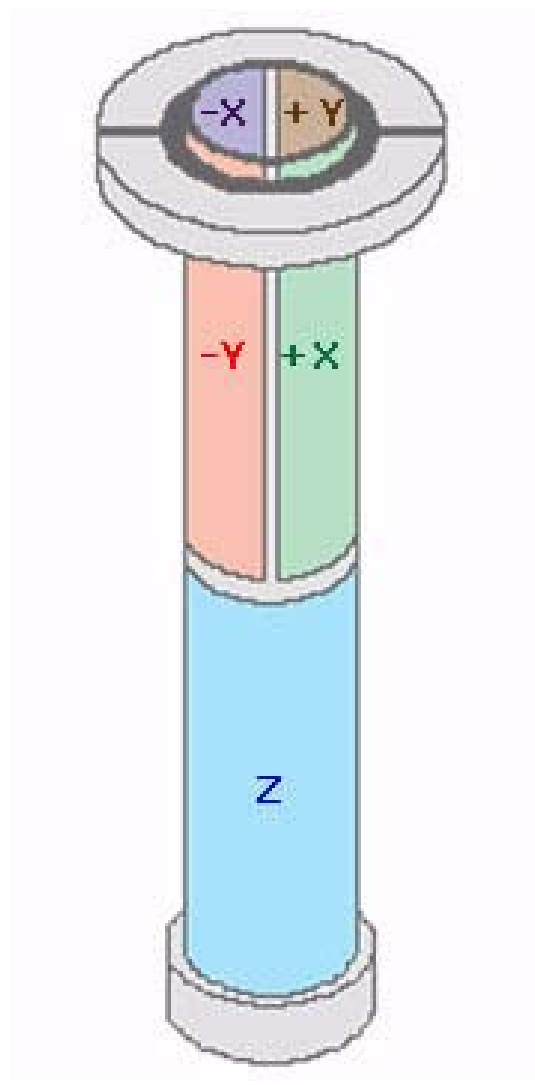
Figure 4.3: The piezo construction found in the TriboScanner piezo stack, from [83]**.**
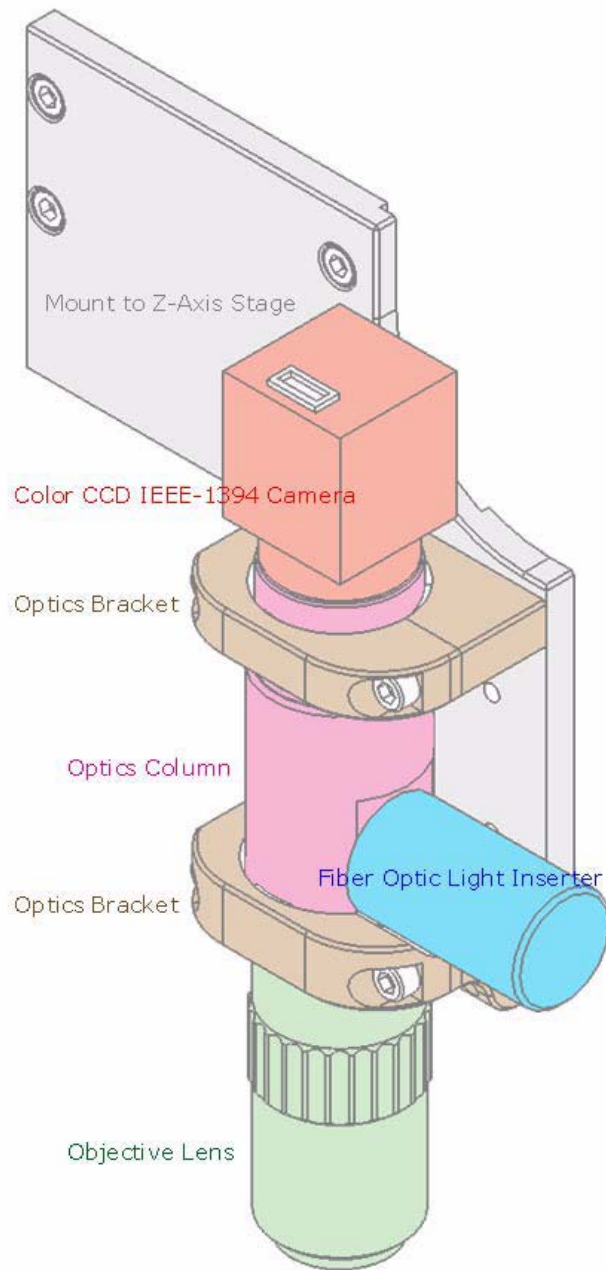
Figure 4.4: A diagram of the optical system used by the TI-950 Hysitron Triboindenter to image the sample surface, and define the sample boundaries that will be used for indentation, from [83]**.**
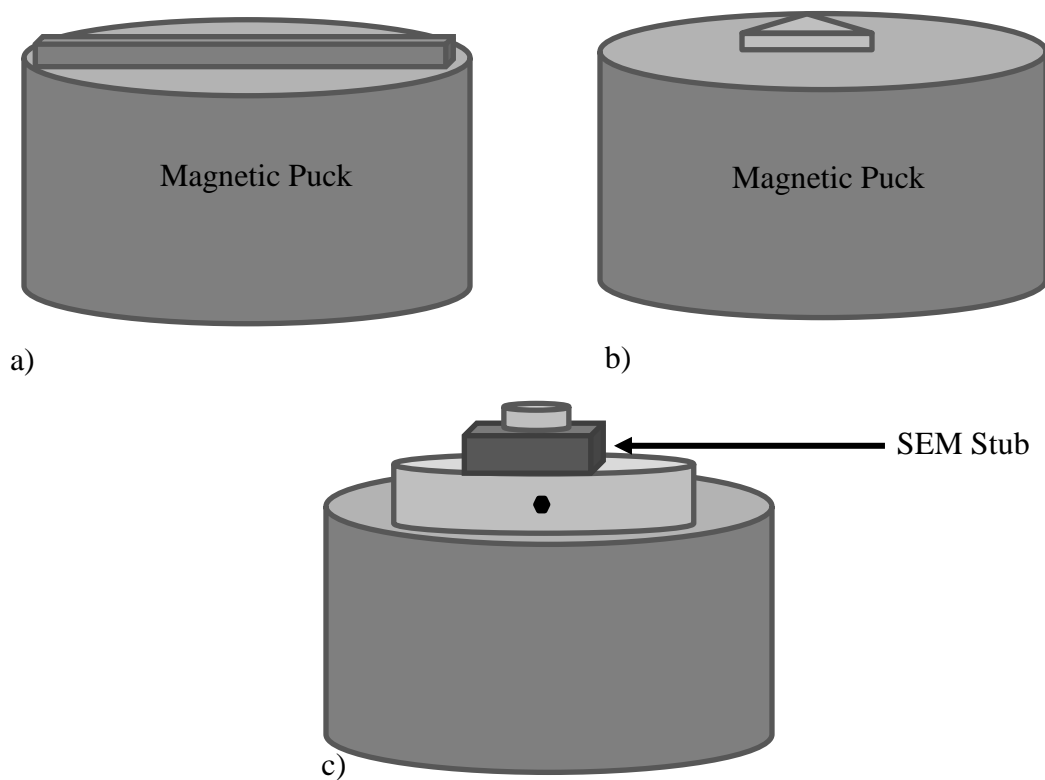
Figure 4.5: A simple diagram depicting the mounting method used for each irradiation condition: a) ion irradiated, b) as received, c) neutron irradiated. A unique probe area calibration was used for each mounting method to address any effect the mounting method had on machine compliance. Image is not to scale.
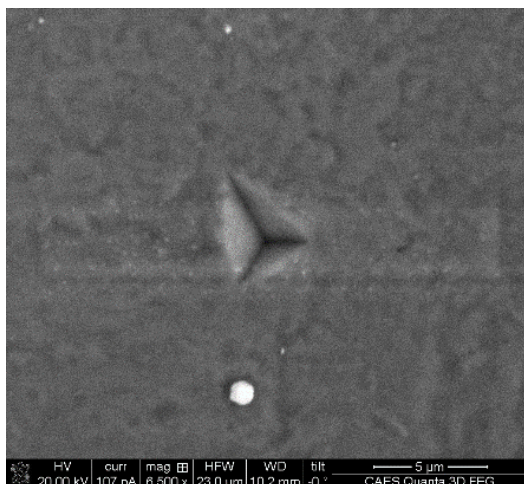
a)
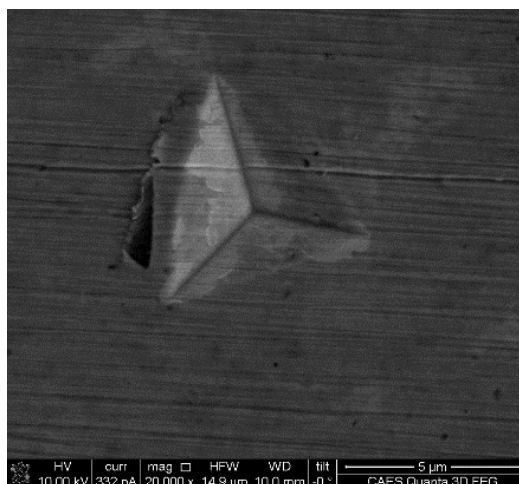
b)
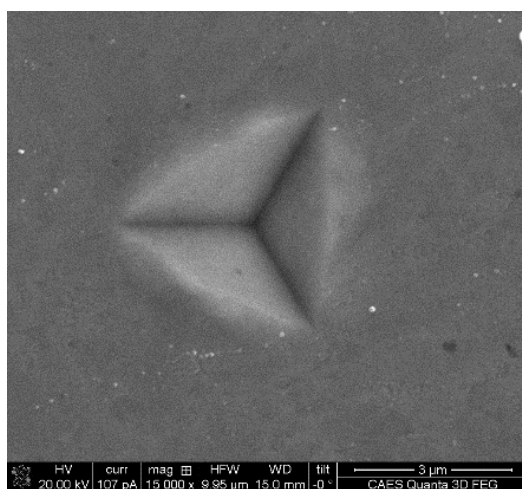
c)

Figure 4.6: SEM images of the indents chosen to create FIB liftouts. a) as received, b) ion irradiated, c) neutron irradiated.
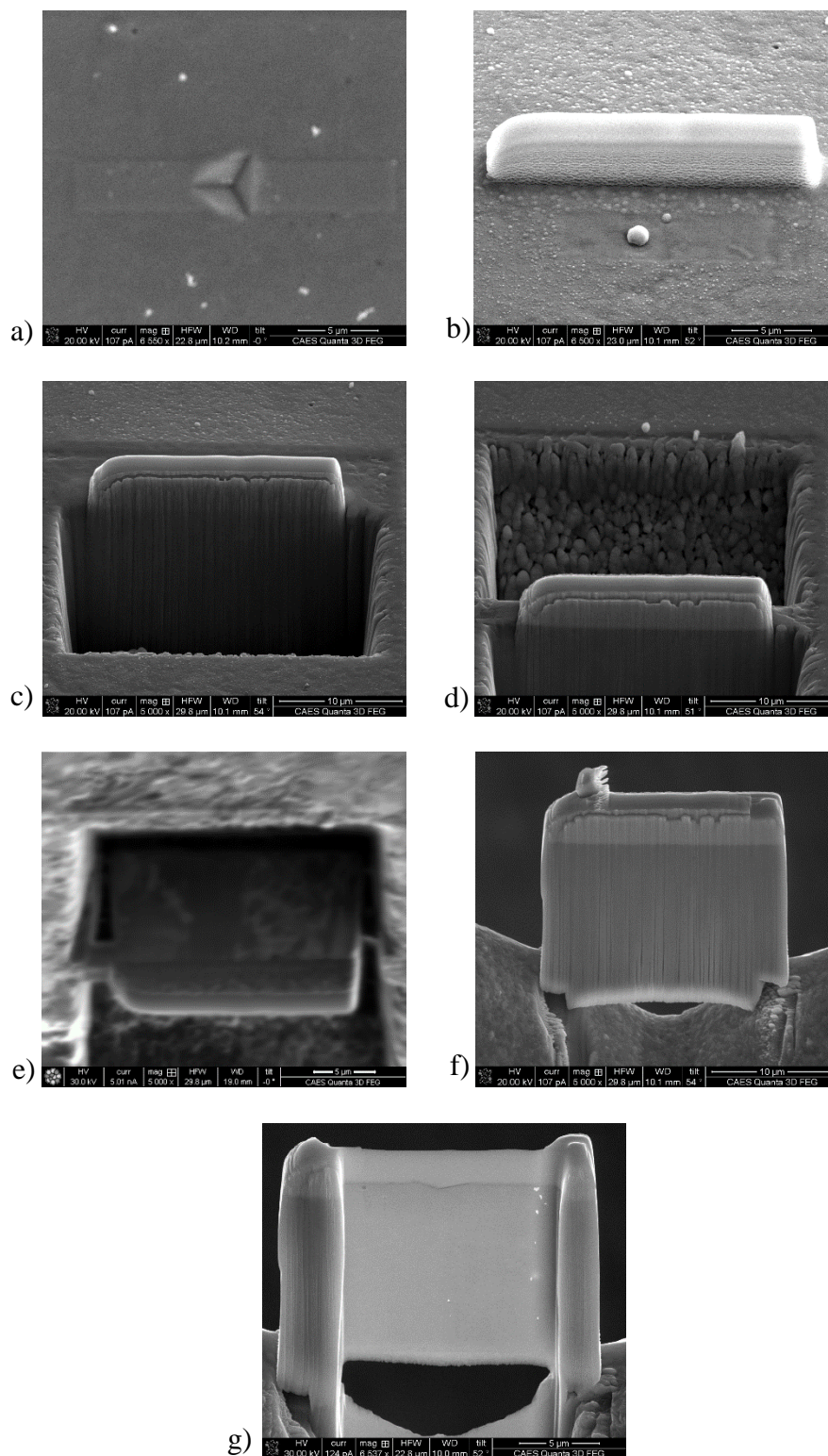
Figure 4.7: SEM images depicting the creation of the TEM lamellas using the Focused Ion Beam.
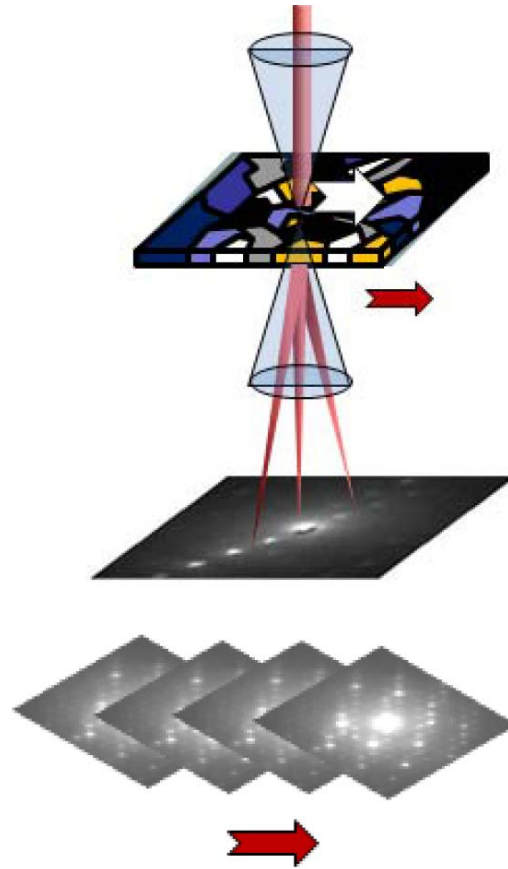
Figure 4.8: A diagram of the ASTAR system showing how a series of diffraction patterns are collected and used to determine grain orientation within a TEM sample, from [135].

CHAPTER FIVE: RESULTS

The experimental work was carried out to measure the irradiation hardening, and determine how the irradiation hardening affected the tensile properties of an ODS alloy. The purpose of this chapter is to report the results of the experiments that were performed, as described in Chapter 4, and to validate those results against those found in literature.

5.1 Nano-Indentation

Characteristic load displacement curves for the as received, ion irradiated and neutron irradiated conditions are presented in Figure 5.1, Figure 5.2, and Figure 5.3. Examination of theses curves provides one of the most powerful indications that the chosen testing parameters provided valid results. The flat region prior to indentation verifies that the probe started the test out of contact with the surface. Each plot was corrected to set the location where the load was seen to increase away from the static flat region as the zero point for displacement. The shifts were on the order of tens of nanometers, which indicates that the load set point used to determine surface contact was adequate. Initially the load increases with the indentation depth, giving good indication that the sample and probe are clean and properly mounted. An adequate hold period is confirmed by the absence of a negative displacement occurring prior to unloading, and by the absence of the characteristic bow shape that is associated with thermal drift or creep effects during testing. The tail at the end of the unloading curve, observed on the as received 100 nm curve and the ion irradiated 100 and 200 nm curves, is associated with indents where the surface prevents uniform contact between the indenter probe and the

sample. There are no indications of surface affects in the neutron irradiated sample [83]. These images agree with the surface roughness measurements, with the increased influence of the surface for the as received sample, when compared to the neutron irradiated sample, attributed to the sampled region deviating from being perfectly perpendicular to the direction of indentation by a few degrees.

The measured nano-hardness data for all irradiation conditions is shown in Figure 5.4, and reported in Table 5.1 through Table 5.3. The hardness values calculated from 100 nm and 200 nm indents were not included in future analysis to limit tip radius effects.

A nano-hardness ranging between 4.43 and 4.99 GPa was calculated for the as received sample, with the hardest value reported at an indentation depth of 400 nm depth and the softest value reported at a depths of 300 and 1000 nm. The value calculated in this study compares to those reported by Huang et al. [136], and Chen et al. on a 19Cr-5.5Al PM2000 ODS alloys, which reported nano-hardness values of ~3.8, and 4.89 GPa respectively.

The softer nano-hardness values reported at depths less than 300 nm are attributed to the surface roughness and deviations from the contact mechanics that are described in Section 2.3.3. The surface roughness causes less of the sample to be in contact with the probe, which results in overestimating the contact area, and less load being required to extend the probe to the desired contact depth. Both of these effects contribute to underestimating the nano-hardness at shallow depths.

Neutron irradiation increased the nano-hardness, with a range between 4.67 and 5.14 GPa. These values were measured at depth of 500 and 900 nm, respectively. A

study by Hosemann et al [137], [138], reported a nano-hardness of 5-5.25 GPa for a neutron irradiated 8wt%Cr ODS alloy irradiated to 20.3 dpa at 400° C. While Hosemann's study does not report the amount of hardening that occurred, a range of -314.70 to 567.92 MPa was observed in this work. However, the standard error of the mean for the irradiation induced hardening is on the same order of magnitude, creating a layer of ambiguity to the calculated values, and is thought to contribute to the irradiation softening that is observed at an indentation depth of 400 nm. The limitations in the sensitivity of the equipment required for deep indentation contributed to the large uncertainties.

For the ion irradiated condition, irradiation induced softening was observed through a depth of 500 nm, while deeper depths provided a range of hardening between 24.91 to 507.57 MPa. At distances greater than 500 nm, the nano-hardness was between 4.46 and 5.19 GPa. These depths compare to a study by Chen et al. on dual beam irradiation of an ODS FeCrAl alloy using 2.5 MeV Fe+ and 350 keV He ions to 31 dpa, calculated using the full cascade of radiation damage in the SRIM™ software, which reported nano-hardness values of 5.86, 5.36, and 5.58 GPa, and average irradiation induced hardening of 970, 280, and 10 MPa for 0%, 50%, and 70% cold rolled conditions [116].

5.2 Plastic Zone Imagining

5.2.1 ASTAR Mapping

Reliability, orientation, index, and virtual bright field maps are shown in Figure 5.7 through Figure 5.9. The reliability map provides visual indication of the measure of fit between the recorded diffraction pattern and the index pattern that was used to

determine grain orientation. Regions that are white in color have a high degree of correlation, while black regions are associated with greater mismatch. Orientation maps depict the crystallographic directions associated with each imaged grain. Index maps section the image according to crystal index, creating distinct boundary regions which helps locate individual grains. Virtual bright field maps recreate the bright field image responsible for the recorded diffraction patterns, but because the precession of the beam averages out dynamical effects, dislocation contrast is greatly reduced [134].

The reliability maps for the as received and neutron irradiated samples indicate that they were accurately described using the experimental parameters. However, the ion irradiated sample contains large areas of mismatch. A common reason for poorly fit images is sample thickness leading to measurements recorded from multiple crystal orientations. This is not thought to be the case, because of the well distinguished grain boundaries that are portrayed. Instead, this region of misfit is attributed to a high defect density in the irradiated layer, and a scan size that is too large for the grain structure. The poor result from the ion irradiated sample are such that specific orientations are not able to be determined.

5.2.2 TEM Images

The bright field TEM images, shown in Figure 5.10 and 5.11, depict a post indentation microstructure that contains the semi-spherical plastic deformation characteristic of indentation experiments. The defect contrast used to characterize the shape of this deformation is attributed to the residual strain of the material. Grain boundary contrast was also used when grains fell on the boundary between regions of plastic and elastic deformation. However, determining the outline of plastic deformation

in a polycrystalline material is not a trivial task. When the grain boundary effects are combined with a well-developed dislocation network resulting from irradiation exposure, determining what mechanism is responsible for image contrast becomes increasingly difficult. The plastic zone measurements presented in this study come from best efforts to combine the observed grain deformation available from both ASTAR and TEM imaging, and the strain contrast observed in TEM images. When outlining the deformation, contrast within grains was preferred over grain boundary contrast to minimize confusion between the boundaries arising from elastically and plastically stress regions, and the contrast arising from misorientation along grain boundaries. Image analysis was done using Digital Micrograph software that has been calibrated to be accurate to the hundredths of a micron.

5.2.2.1 Determination of Indentation Depth

The final residual depth measured from the initial surface of the sample, h_f, defined in Figure 2.24 and measured in Figure 5.10, was determined to be 0.61, 0.50, and 0.43 μm for the ion irradiated, neutron irradiated, and as received samples, respectively. The Oliver and Pharr fitting method utilized h_f as one of the parameters used to describe the power law fit for the unloading curve and is calculated by the TriboIndenter software using Equation 2.13. The experimentally measured value was compared with the average calculated final residual depth to determine the indentation depth for each condition. It was found that the images depicted a 700 nm ion irradiated indent where the calculated $h_{f,avg} = 0.615$ μm. The neutron irradiated lift out is a 600 nm indent with the calculated $h_{f,avg} = 0.518$ μm, and the as received sample is a 500 nm indent with a calculated $h_{f,avg} = 0.448$ μm. That is a difference of 0.8%, 3.5%, and 4.1% respectively.

The final residual depth measured for the neutron irradiated sample was equally distant from the calculated values for both the 500 nm and 600 nm indents, but determined to be a 600 nm indent because none of the calculated residual depths exceeded 0.43 μm. The error is attributed to the sample not being mounted parallel to the TEM grid leading to a slight optical parallax.

5.2.2.2 Determination of Plastic Zone

In each case the plastic zone extends past the contact radius of the indenter, which is characteristic of plastically dominated deformation. In the case of the as received and neutron irradiated conditions this result is predicted based on condition described in Section 2.3.5, where elastic strain is negligible when $E/\sigma_r < 110$. The modulus to uniaxial stress ratios, at the depths at which plastic zones were imaged, are 108, 121, and 133 for the ion irradiated, neutron irradiated, and as received conditions, respectively. The ion irradiated sample deviates from this relationship, due to effects that the thin damage layer has on the uniaxial stresses in the sample.

The extent of the plastic deformation measured directly below the indenter probe is shown in Figure 5.11, and determined to be 4.18 μm, 3.68 μm, and 3.30 μm for the ion irradiated, neutron irradiated, and as received samples respectively. The TEM measurements where compared to two different models to determine the appropriateness of their magnitudes.

A simple solution to Johnson's model developed by Harvey, Equation 2.28, provides an estimate of the radius of the plastic zone by incorporating the yield strength of the material, which is related to the nano-hardness of F-M alloys as:

$$\sigma_{ys}(MPa)=3.06\left(\frac{H(GPa)}{.009807}\right) \qquad \textbf{Equation 5.1 } [24]$$

This approximation has been shown to be a reasonable first order approximation when

$E\tan\beta/\sigma_{ys}$ is between 50 and 500 [98], where β ,the angle between the surface of the

sample and the edge of the indenter, is equal to 24.7° for a Berkovich indenter. This ratio

is 59 for the ion irradiated condition, 66 for the neutron irradiated condition, and 84 for

the as received condition. Harvey's simple solution results in plastic radii of 4.33 μm for

the ion irradiated sample, 3.79 μm for the neutron irradiated sample, and 3.17 μm for the

as received sample. The parameters used for the calculation are listed in Table 5.4.

Experimentally, the radius of plastic zone can be measure by combining the

measured plastic zone and the residual depth measurements, resulting in plastic radii of

4.79 μm, 4.18 μm, and 3.73μm for the ion irradiated, neutron irradiated, and as received

conditions, which correspond to percent errors of 10.1%, 9.8%, and 16.2%, respectively.

These errors are attributed to deviations from the elastic perfectly plastic assumption used

to derive Johnson's model, and are on the same order as the errors reported by Robertson,

Poissonnet, and Boulanger when using Johnson's model to predict plastic deformation in

ion irradiated 316LN austenitic stainless steel of 28.9% and 24.6% on indents of 100nm

and 250 nm respectively [139].

A two-dimensional finite element analysis (FEA) study is underway to support

the plastic zone measurements of this work, and to examine the stress and strain fields

that are experienced under nano-indentation. The student version of ABAQUS™ 6.12-2

was used to model the stress field for each condition based on the modulus and yield

strength measured via nano-indentation, with a mesh size that was limited to 1000 nodes

under frictionless conditions. A thin film approach was used to model the ion irradiated

condition, with a 1.5μm film representing the damage layer. Preliminary results of the plastic zone, as determined by the Von Mises criteria, are shown in Figure 5.12, with plastic zones of 4.38 μm, 3.76 μm, and 3.13 μm for the ion irradiated, neutron irradiated, and as received conditions, respectively. The FEA results have a percent difference of 4.7%, 2.2%, and 5.3% when compared to the TEM measurements of the ion irradiated, neutron irradiated, and as received conditions. Future work will expand this study by increasing the number of nodes to enhance the precision of the model.

The support of the two modeling methods provide assurances that the contrast characterized via TEM techniques is indeed the plastically deformed volume induced by indentation. Examination of how the plastic deformation is altered by irradiation requires the plastic zones are normalized by the indentation depth. The normalized plastic zones are 5.97 for the ion irradiated condition, 6.24 for the neutron irradiated condition, and 6.59 for the as received condition, all of which fall into the range of 5 – 10 that is expected for metals [84], [93], [98], [111], [140]. The simple solution to the Johnson model predicts that the extent of plastic deformation will decrease as the yield strength increases. This is seen as a reductions in the normalized plastic zone of 9.9% and 5.5% for the ion and neutron irradiated conditions.

Table 5.1: **Nano-hardness measurements of the as received sample.**

Indentation Depth (nm)	Number of Indents	Average Hardness (GPa)	Standard Error of the Mean (GPa)
100	11	3.44	0.20
200	10	4.37	0.20
300	12	4.43	0.07
400	11	4.99	0.16
500	7	4.43	0.19
600	9	4.44	0.12
700	11	4.60	0.22
800	12	4.50	0.15
900	12	4.88	0.12
1000	9	4.61	0.15

Table 5.2: Nano-hardness and irradiation induced hardening of the neutron irradiated sample measured from nano-indentation, and the associated change in yield strength calculated with Equation 5.1. Limited statistics are due to size restraints of the sample.

Indentation Depth (nm)	Number of Indents	Average Hardness (GPa)	Standard Error of the Mean (GPa)	Irradiation Hardening (MPa)	Standard Error of the Mean (MPa)	Δ Yield Strength (MPa)
100	7	9.72	0.29	6287.40	352.61	1961.81
200	8	4.66	0.11	293.00	228.31	91.42
300	8	5.00	0.14	567.92	161.79	177.2
400	12	4.67	0.08	-314.70	176.26	-98.19
500	12	4.84	0.05	402.38	201.46	125.55
600	7	4.97	0.11	537.62	155.90	167.75
700	6	4.90	0.04	295.76	220.67	92.28
800	10	5.02	0.06	525.00	165.34	163.81
900	7	5.14	0.01	263.93	125.45	82.35
1000	10	4.96	0.05	346.00	160.36	107.96

Table 5.3: Nano-hardness and irradiation induced hardening of the ion irradiated sample measured from nano-indentation, and the associated change in yield stress calculated with Equation 5.1.

Indentation Depth (nm)	Number of Indents	Average Hardness (GPa)	Standard Error of the Mean (GPa)	Irradiation Hardening (MPa)	Standard Error of the Mean (MPa)	Δ Yield Strength (MPa)
100	22	3.73	0.32	297.33	6287.40	92.77
200	22	4.26	0.14	-111.88	293.00	-34.91
300	19	4.31	0.09	-120.48	597.92	-37.59
400	20	4.70	0.10	-285.51	-314.70	-89.09
500	24	4.46	0.10	24.91	402.38	7.77
600	22	4.51	0.06	76.33	537.62	23.82
700	23	4.83	0.07	227.12	295.76	70.87
800	19	5.00	0.09	507.57	525.00	158.37
900	19	5.19	0.07	315.83	263.93	98.55
1000	25	4.90	0.07	294.63	346.00	91.93

Table 5.4: Parameters used to calculate the plastic zone using Harvey's simple solution to the Johnson model for the 700 nm ion irradiated liftout, 600 nm neutron irradiated liftout, and the 500 nm as received liftout.

	Ion Irradiated	Neutron Irradiated	As Received
P (µN)	55491.7	46681.6	29027.5
σ_{ys} (MPa)	1413.48	1550.75	1382.3
E (GPa)	194	223	218
β (°)	24.7	24.7	24.7
$(E\tan\beta)/\sigma_{ys}$	59	66	84
c (µm)	4.33	3.79	3.17
z_{ys}/h	5.97	6.24	6.59
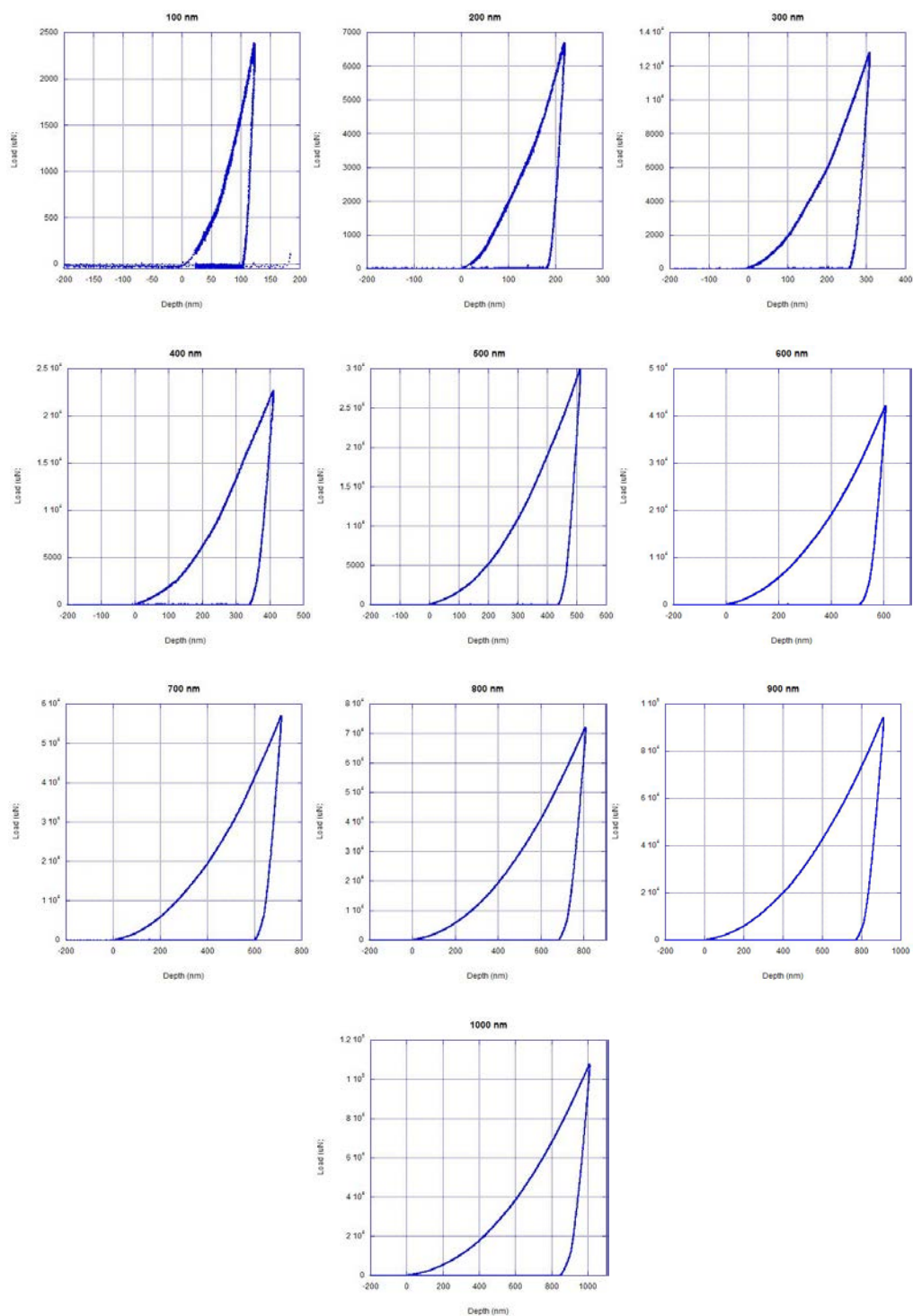
Figure 5.1: Typical load displacement curves for the 9wt%Cr as received ODS alloy.
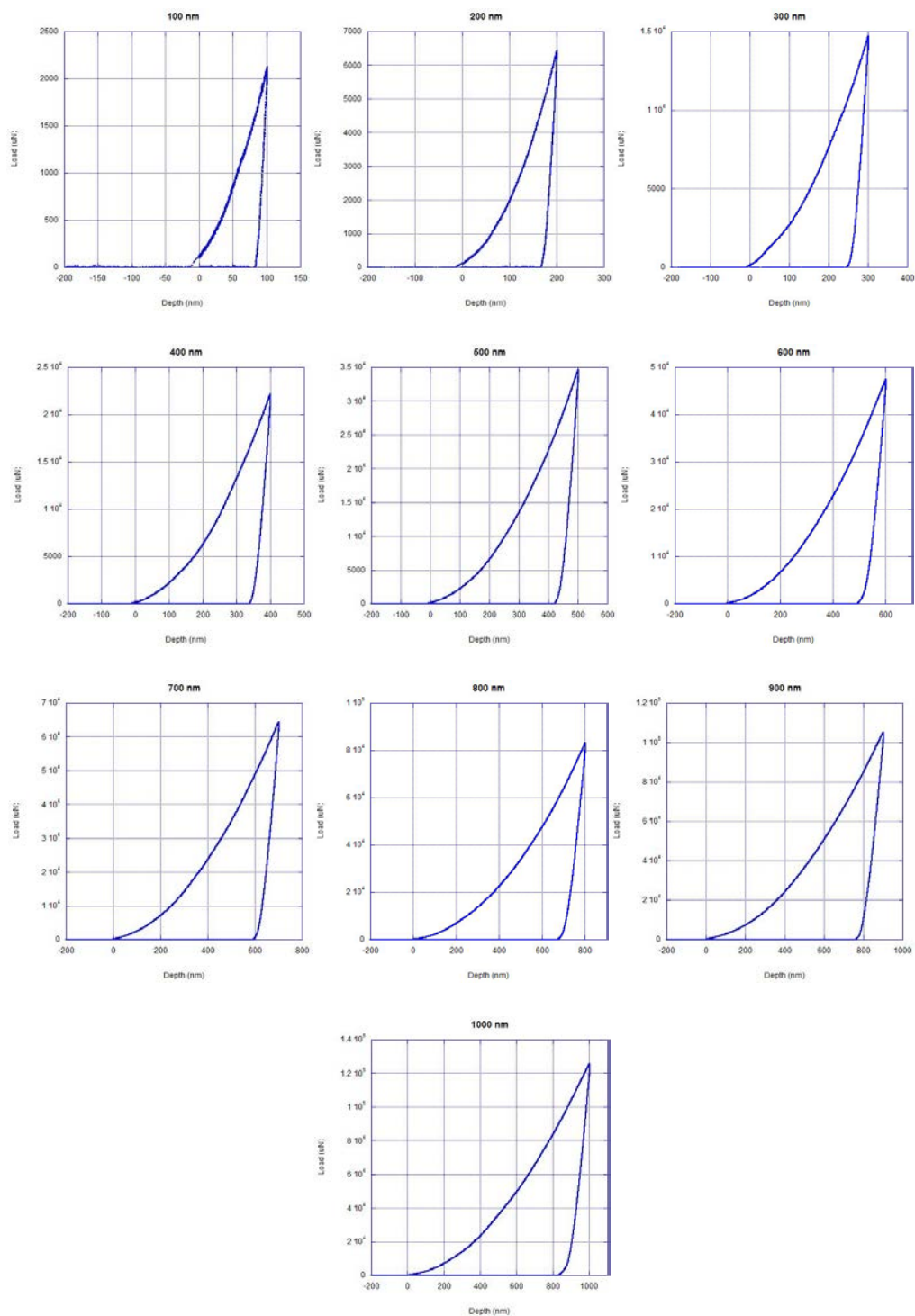
Figure 5.2: Typical load displacement curves for the 9wt%Cr ODS neutron irradiated alloy.
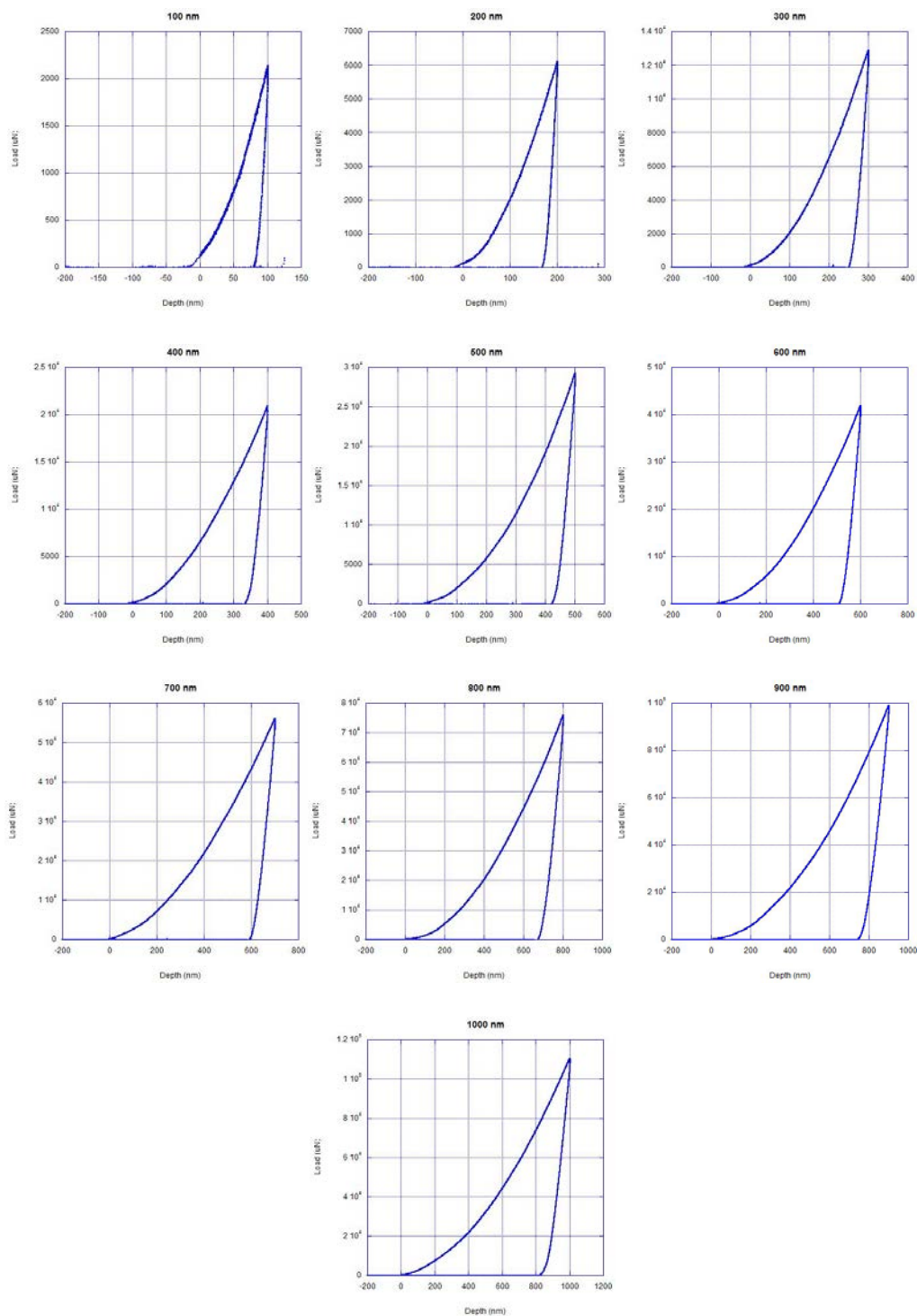
Figure 5.3: Typical load displacement curves for the 9wt%Cr ODS ion irradiated alloy.
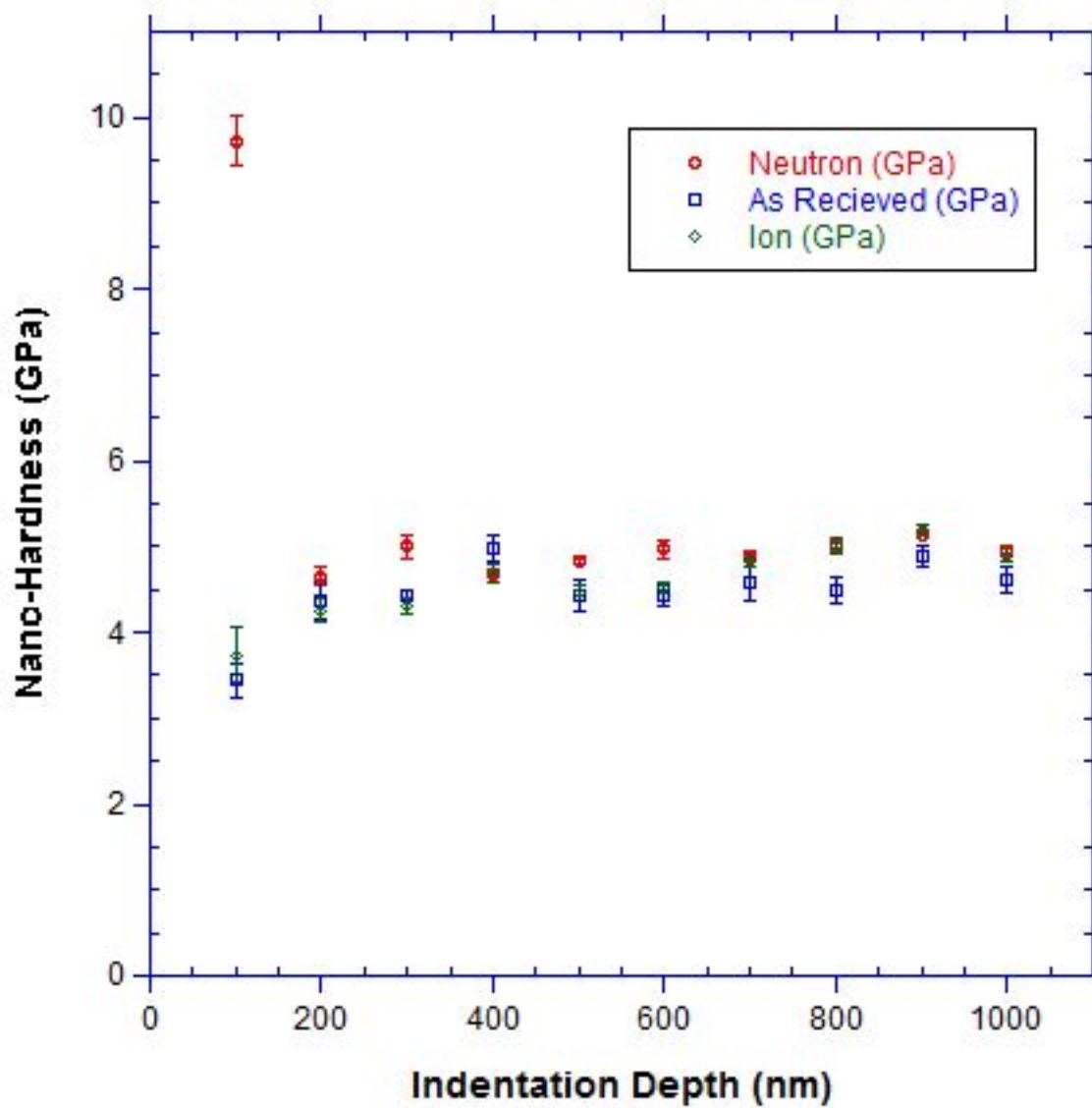
Figure 5.4: A comparison of the nano-hardness data collected using a TI-950 TriboIndenter.
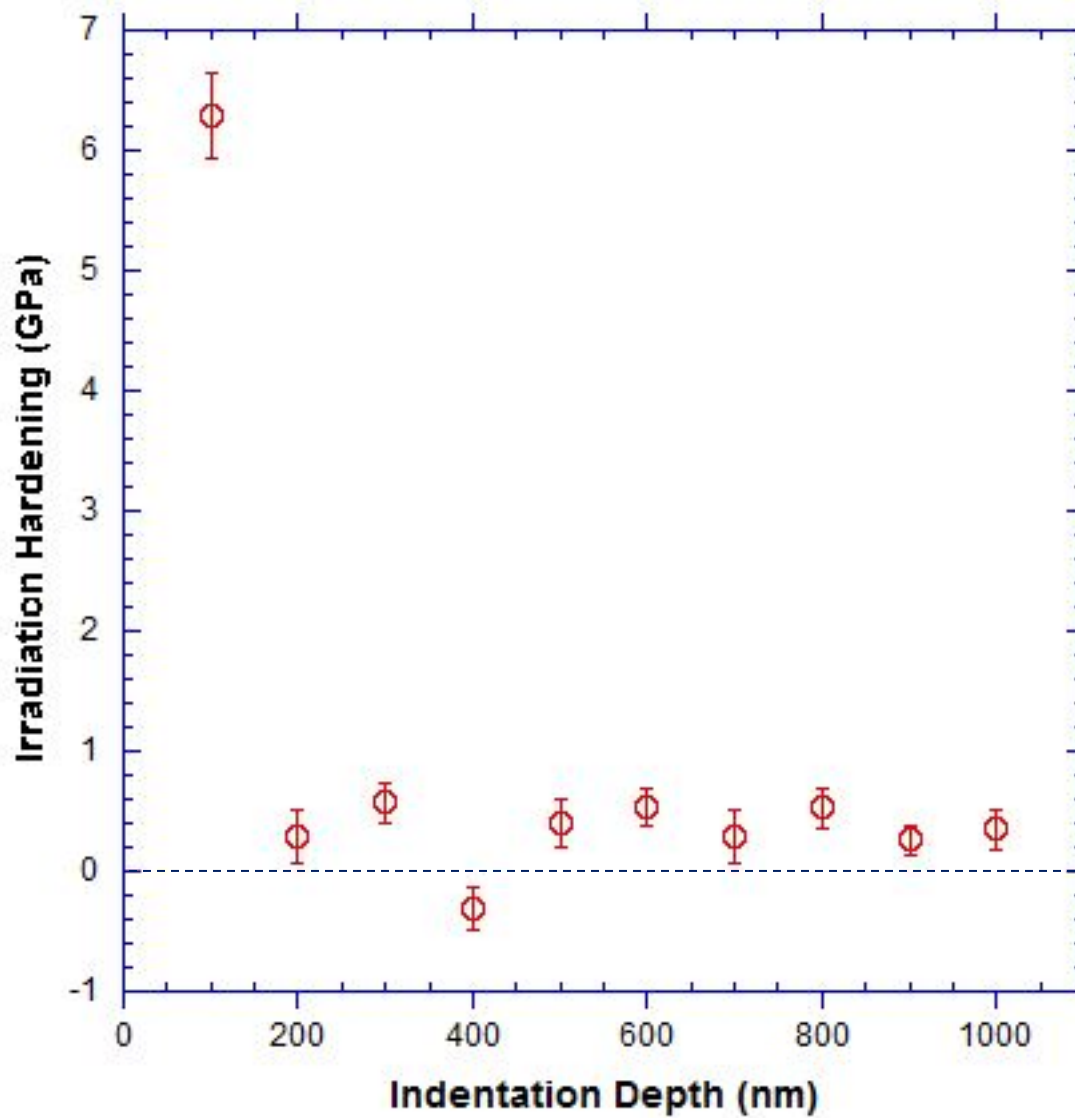
Figure 5.5: Irradiation induced hardening due to neutron irradiation to 3 dpa at 500° C.
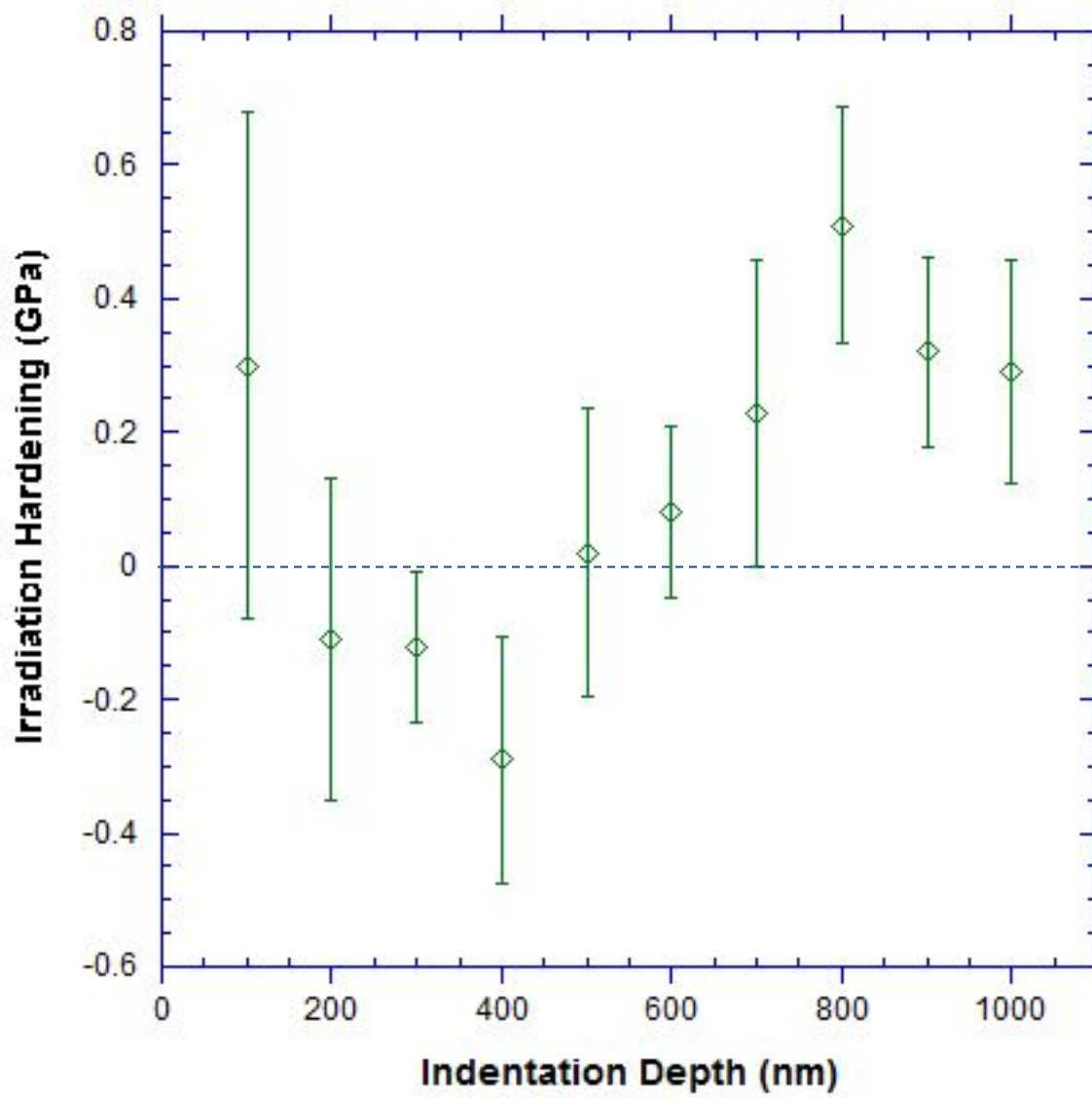
Figure 5.6: Irradiation induced hardening due to ion irradiation to 100 dpa at 400° C.
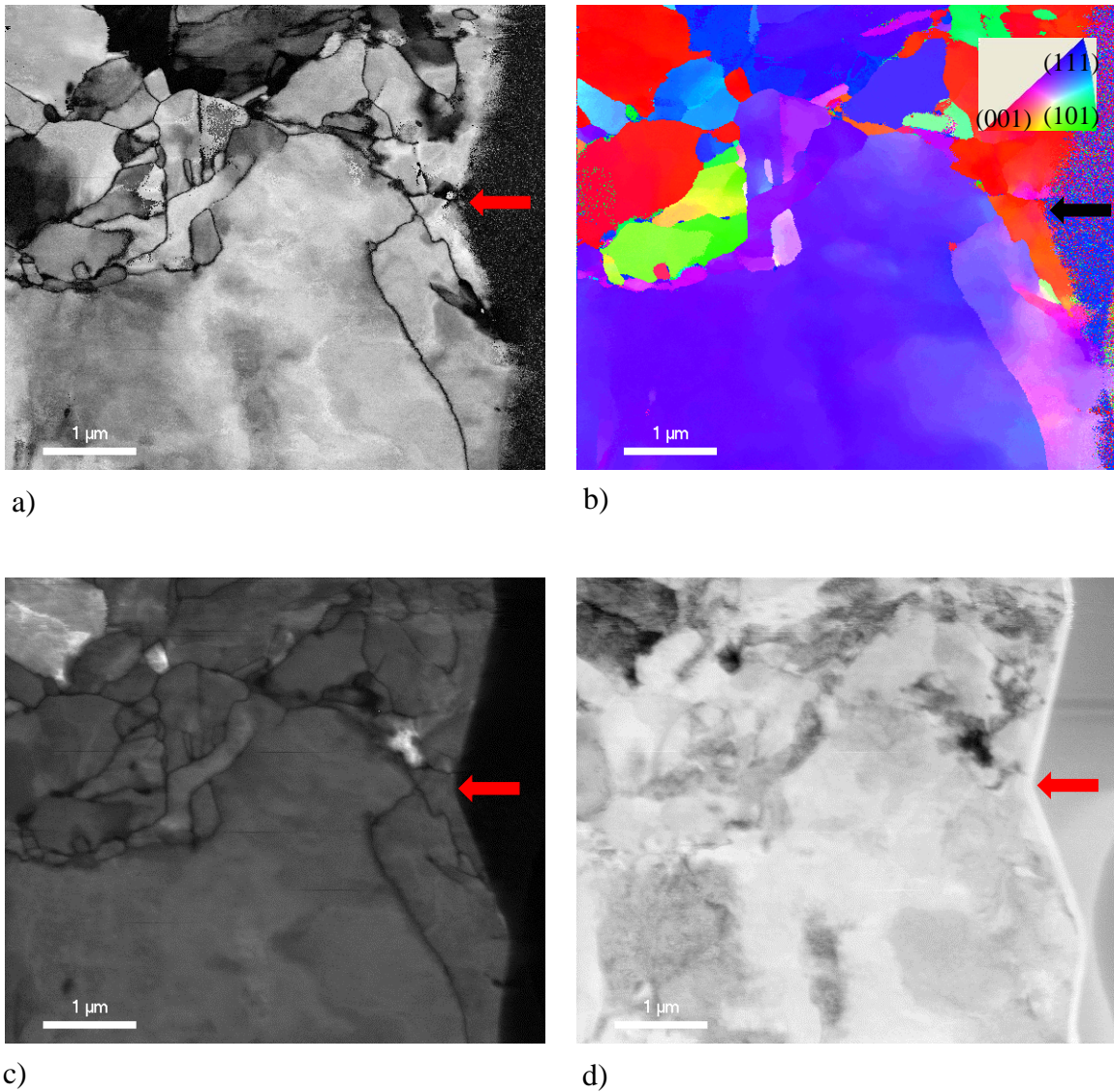
Figure 5.7: ASTAR images for the as received sample: a) The reliability map depicts a strong agreement between the measured diffraction pattern and those corresponding to the index file. b) The orientation map shows that this image is located on an unusually large grain, and does not demonstrate an orientation direction that is consistent between grains. c) The index map clearly shows the grain structure of the sample. d) The virtual bright field image shows an image of the crystal structure with dislocations removed. The arrow represents the center of the indent.
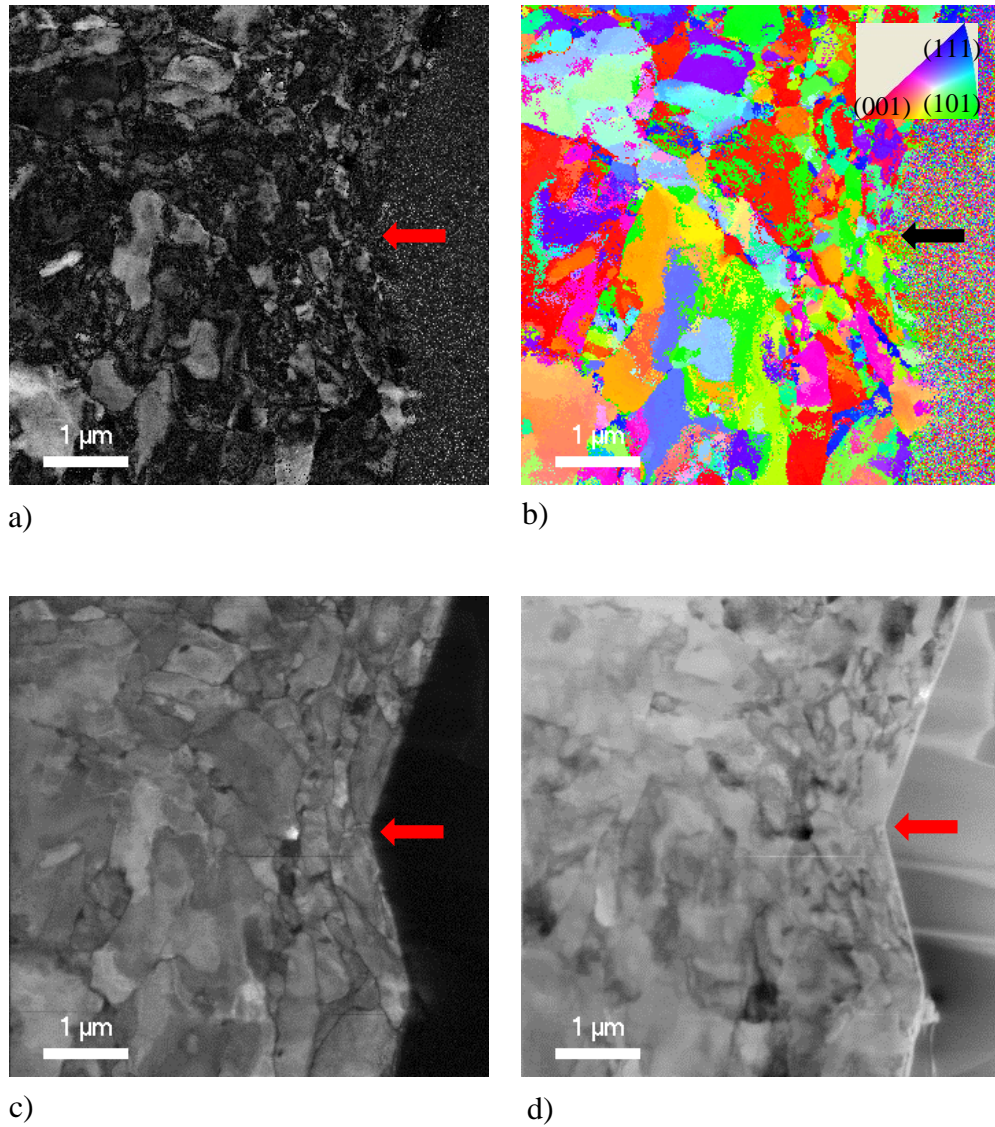
Figure 5.8: ASTAR images for the ion irradiated sample: a) The reliability map shows a lack of agreement between the measured diffraction pattern and those corresponding to the index file, which causes a lack of resolution in the b) orientation map, and the c) index map. This limits the application of this scan in terms of determining orientation, but the d) virtual bright field image is consistent with traditional TEM images, and shows the curving of grains exposed to the plastic strain field. The arrow represents the center of the indent.
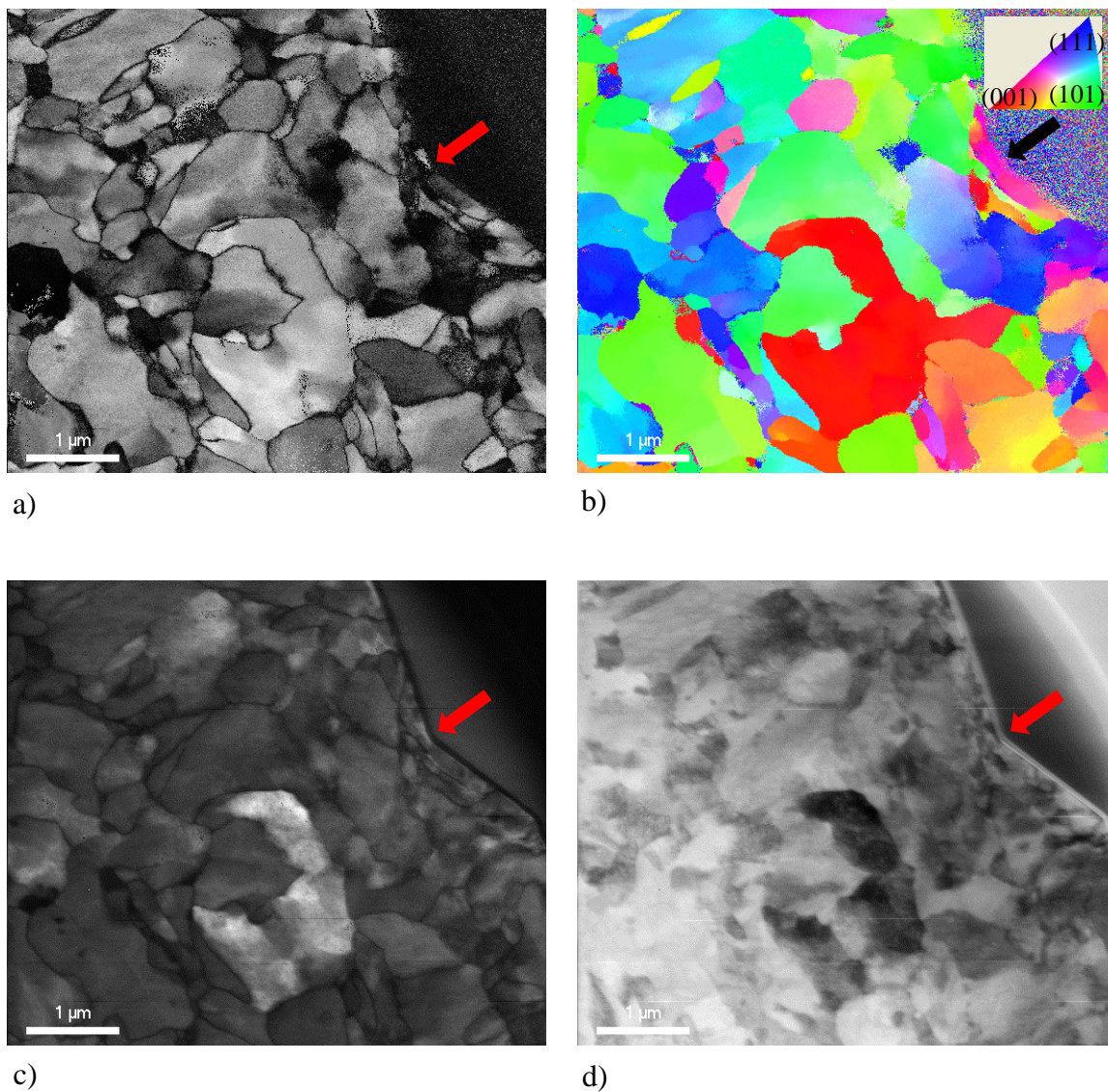
Figure 5.9: ASTAR images for the neutron irradiated sample: a) The reliability map depicts a strong agreement between the measured diffraction pattern and those corresponding to the index file. b) The orientation map does not demonstrate an orientation direction that is consistent between grains. c) The index map clearly shows the grain structure of the sample. d) The virtual bright field image shows an image of the crystal structure with dislocations removed. The arrow represents the center of the indent.
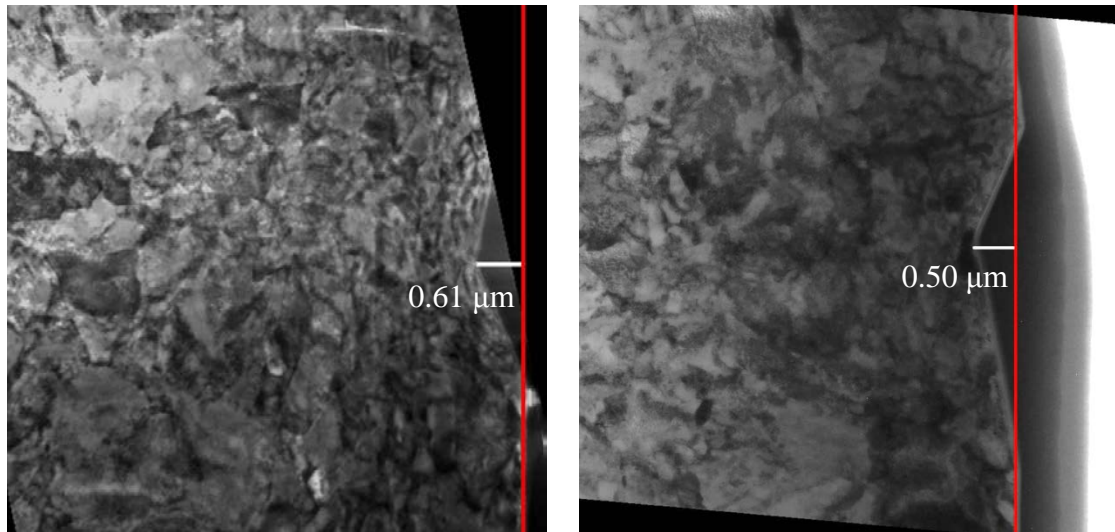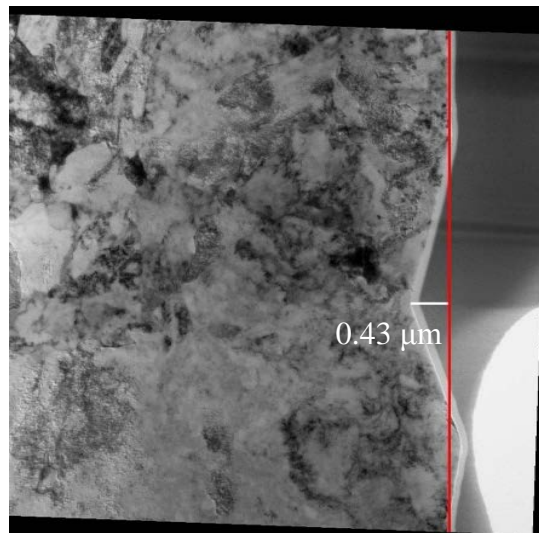
Figure 5.10: TEM images used to measure the residual depth of the nano-indent in a) ion irradiated, b) neutron irradiated, and c) as received samples. The images have been rotated so the original indentation surface is vertical.
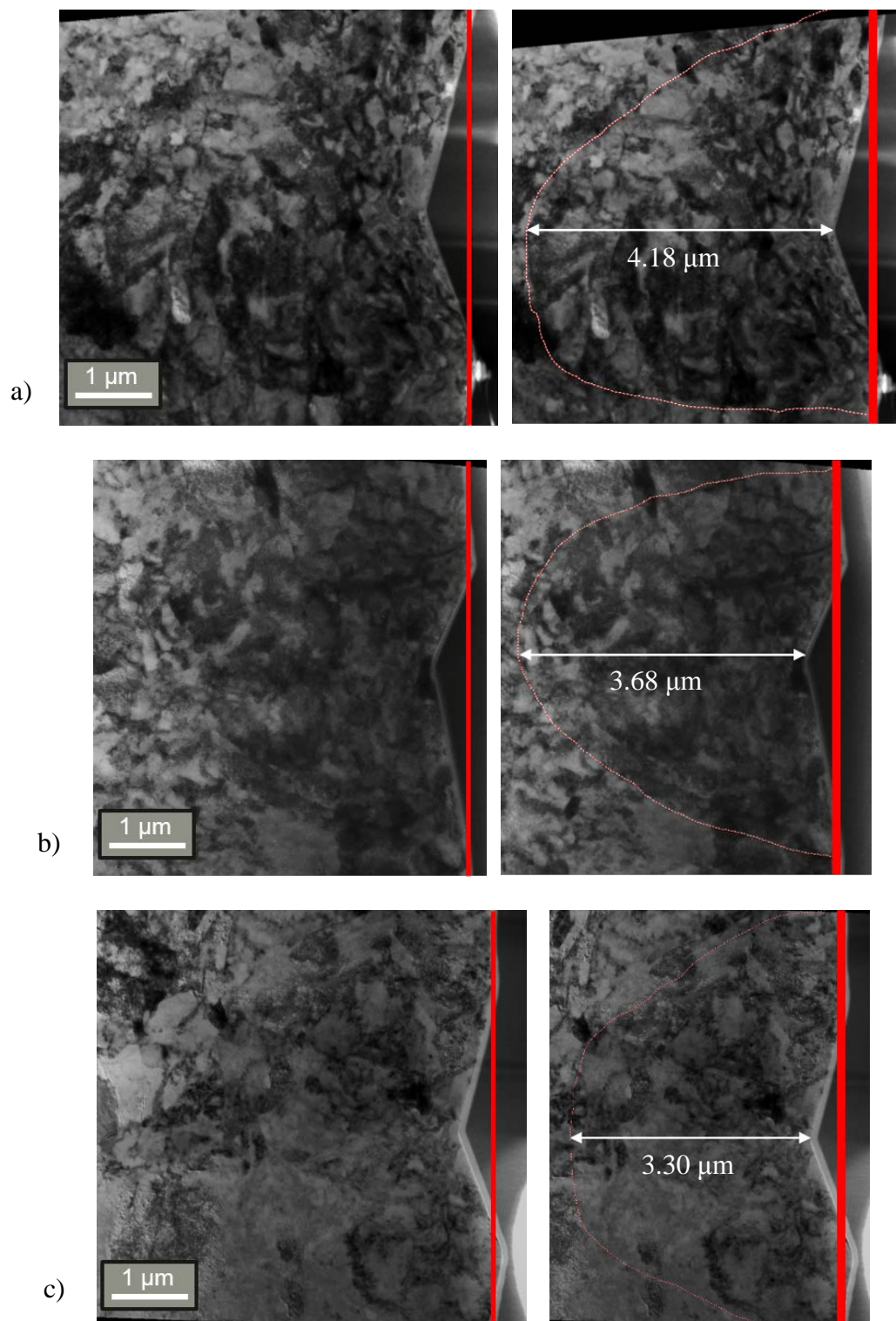
Figure 5.11: TEM images depicting the defect contrast used to measure the depth of the plastic deformation that occurs below a nano-indent in a) ion irradiated, b) neutron irradiated, and c) as received samples.
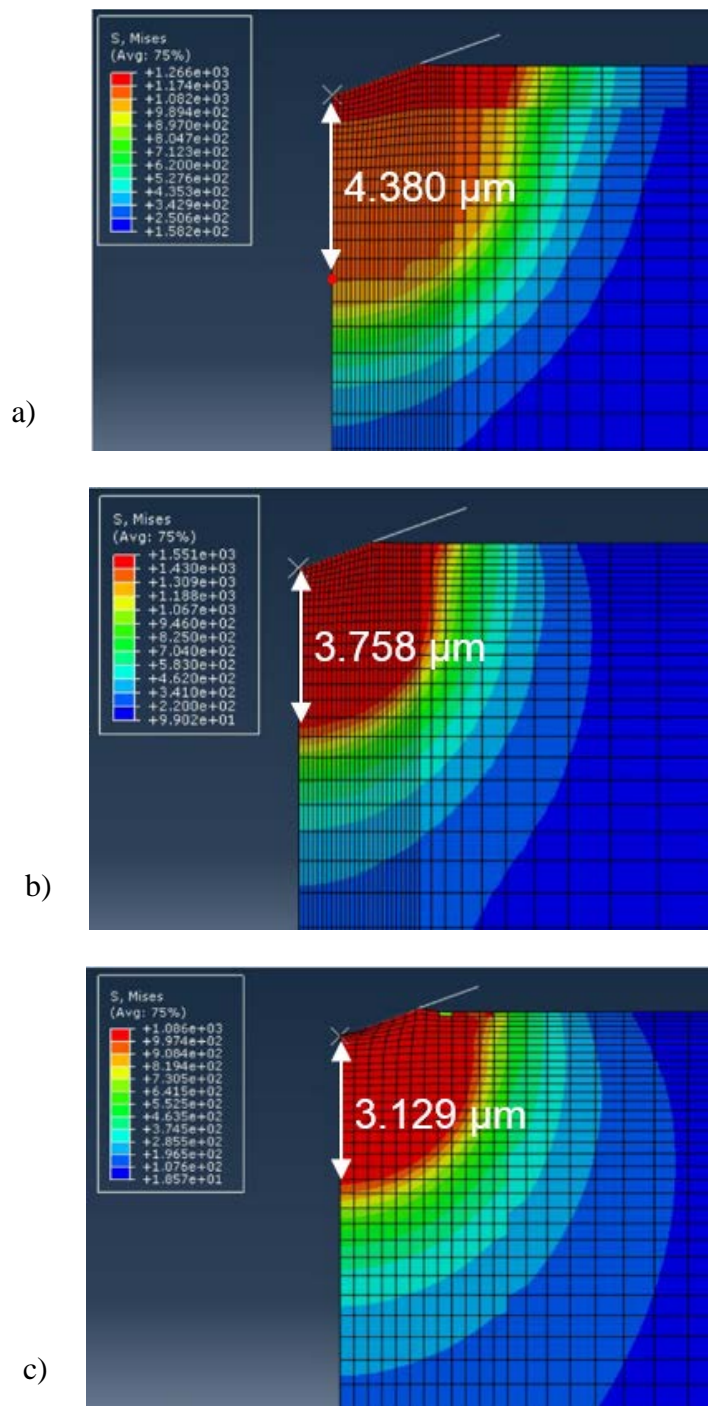
Figure 5.12: Finite Element Analysis modeling of the stress field due to nano-indentation for the a) ion irradiated, b) neutron irradiated, and c) as received samples. The plastic zone is isolated by determining the region that satisfies the Von Misses stress criteria, depicted in red in the neutron and as received samples, and the red and orange in the ion irradiated sample.

CHAPTER SIX: DISCUSSION

Previous sections provide insight into the theory and accuracy of experimental

work designed to measure the influence of irradiation on the nano-hardness, and

deformation of iron ODS alloys. This chapter will address the limitations of this

approach, and use the experimental results to estimate the true stress true stain

relationship that can offer insight into the nature of plastic deformation under irradiation.

6.1 Nano-Indentation

The nano-indentation measurements in this work were performed using a probe

tip with a radius of approximately 200 nm. A probe can be considered dull when the

plastic depth is within 20% of the radius of curvature of the probe, as the contact

geometry becomes a combination of the spherical and pyramidal probes [83]. This is the

case for indents of less than 240 nm for this study, where the conical contact

approximation utilized by the software no longer is accurate. When combined with

surface roughness effects, described in Figure 6.1, larger deviations in nano-hardness

occur when an indent is performed on a sloped region. These deviations occur, because

the estimated contact area, used by the software, remains the same while the actual

contact area is lower and less load is required to embed the probe into the sample. In an

effort to avoid these affects the results presented in this discussion exclude indents less

than 300 nm.

6.1.2 Thin Film Approximation for Ion Irradiation

SRIM™ calculations predict the thickness of irradiated damage layer, t, to be

1.94 μm. FEA has shown that the damage layer can be modeled as a thin film mounted

on a softer substrate, and work by Robertson [105], on ion irradiated austenitic steels showed that the mechanical properties of the thin film can be isolated a from the substrate if the indention depth is less than 0.33t. That study also reported that the measured mechanical properties of the layered sample approached those of the substrate when indentation depths are greater or equal to $0.55t$ [97]. When applied to the current study, these two approximations correlate to indentation depths of 650 nm and 1070 nm, respectively.

The change in yield strength due to irradiation, and transitively the change in nano-hardness, is attributed to the creation of defects and precipitates during exposure, and can be estimated from micrographs using the dispersed barrier hardening model:

$$\Delta\sigma_{ys} \propto \sqrt{Nd}$$
<div align="right">**Equation 6.1** [24]</div>

where N is the number density of a particular defect, and d is the average defect diameter. The total change in yield strength is the sum of all the contributions due to the specific types of defects such as loops, voids, precipitates,…, etc. Characterization of the microstructure for the ion and neutron irradiated conditions was performed by M. Swenson, and are presented in Table 6.1. It was seen that the number density and diameter of the different defects in the microstructures are on the same scale as one another. This predicts that the change in yield stress, and in turn nano-hardness, is expected to be similar between the two environments, and allows for an examination of when the ion irradiated nano-hardness values are truly representative of the shallow damage layer.

Figure 6.2 depicts the ratio of ion irradiated to neutron irradiated nano-hardness values. It is proposed, based on characterization of the microstructure, that when the

ratio approaches a value of one, the nano-hardness values are independent from the surface or substrate effects. The gradual irradiation induced hardening observed at depths greater than 500 nm, culminating in the equating of nano-hardness measurements between the ion and neutron irradiated samples at 700 nm, indicate that the surface effects begin to depreciate at 500 nm and are nominal by 700nm.

When compared to the thin film effects calculated by Robertson, it is seen that the nano-hardness of the shallow damage layer can be determined beyond the predicted 650nm. In fact this layer cannot be determined prior depths of 700 nm. In the same way, the nano-hardness of the substrate is not dominate by 1000 nm, and the depths probed in this work do not indicate at what depth the ion irradiated nano-hardness approaches that of the as received bulk. Further study is required to determine this location.

In general it is recommended that nano-indentation depths be exceed 10x the average surface roughness of the sample minimize surface effects. This approach dictates that the minimum depth of indentation required for the ion irradiated sample, based on the measured surface roughness to be approximately 1000 nm, and as predicted by Robinson et al would sample into the unirradiated substrate. However, examination of Figure 5.6 and 6.2 indicates that approach to be conservative in the ion irradiated case. The agreement between the nano-indentation and defect structure offers verification that the nano-hardness measured at depths greater than 700 nm are representative of the irradiated damage layer, even though FEA and TEM imaging has shown the plastic zone extends into the bulk substrate. This hints that the nano-hardness measurement has little to do with the volume of the created plastic zone, but is more dependent on the

mechanical properties of the materials in close proximity to the indenter probe. Further study is required to investigate this hypothesis.

6.2 Crystal Orientation Imaging

The low reliability achieved in the ion irradiated sample prevents the use of those images in this discussion. However, the quality of the as received and neutron irradiated scans offer insight into the applicability of imaging plastic deformation through orientation mapping in sub-micron grained polycrystalline materials.

The as received image is dominated by an abnormally large grain, adjacent to many grains with an average grain size of approximately 230 nm in diameter. The large grain shows the same orientation throughout, while the smaller grains have a random crystal direction. There is no evidence of grain boundary sliding, or a characteristic orientation that would allow for plastic zone measurement. The neutron irradiated scan depicts a structure of randomly oriented grains with the same average grain size. Again there is no indication of grain boundary sliding, or re-orientation that occurs under indentation.

While this result prevents the application of a powerful tool for plastic zone imaging, it is not unexpected. Grain boundary sliding occurs either at high temperatures, or in materials with grain sizes smaller than approximately 100 nm [5], [141]. The high temperature case allow for atomic diffusion of atoms to respond to the applied stress through Nabarro-Herring or Coble creep mechanisms, and prevent trans-granular fracture by altering the grain shape. This mechanism is not applicable to this study due to the nano-indentation testing being performed at room temperature. In the case of nano-crystalline materials, a larger percent of the volume consists of grain boundaries which

act as barriers to dislocation movement. This prevents intergranular plasticity, forcing grain boundary sliding to occur in order to minimize the induced stress. In this work the grain size exceeds the nano-scale, and allows for plastic deformation through defect interactions to occur prior to the build-up of the required stresses for low temperature grain boundary sliding.

The ASTAR scans were not without benefit though, as the virtual bright field and index maps elucidated the grain boundaries within the structure. The removal of dislocation contrast, in the prior, and emphasis of grain boundaries, in the latter, provided a guide during examination of the bright field TEM images, which made it easier to determine if the contrast was caused by plastic zone defects, or due to the existing dislocation and grain structure of the material. By comparing these scans side by side to the TEM images the subjectivity of this method was reduced.

6.3 Plastic Zone Measurements

Although the volume of the plastic zone was found to have little effect on the measured nano-hardness, in this study, an understanding of this region is still required to make conclusions on the nature of the plastic deformation. As will be shown in Section 6.4, it is possible to determine the effective strain hardening coefficient, and create true stress and true strain relationships for the material under different irradiation conditions.

As predicted by Johnson and Hill, the size of the plastic zone decreases as the yield strength increases, but the normalized plastic zones do not demonstrate this. In fact, the normalized plastic zone for the ion irradiated condition varies from the neutron irradiated condition by 4.4% even though the calculated yield strength predicts that they should be similar. This value is comparable to the 7.1% reduction in normalized plastic

zone between the as received sample and the neutron irradiated sample. This reduction in plastic zone is attributed to the thin film characteristic of the ion damage profile.

Previous work by Kramer et al. demonstrated that thin films alter the onset of plastic deformation [98] during nano-indentation, while work by Chen, Liu and Wang describe how presence of a thin film induces spatial restraints that limit the geometrically necessary dislocation interactions and locally increase the yield strength at the boundary [142]. It is proposed that the dislocation interactions at the interface between the irradiated and non-irradiated regions reduced the normalized plastic zone for the ion irradiated condition, through dislocation interactions that restrict the area of plastically deformed material. The preliminary FEA work, shown in Figure 5.12, demonstrate the effect the boundary has on the size of the plastic zone, as noted by reduction in the exposed stresses below the boundary, and the reduction of the plastic zone depth to one smaller than what is expected due to the microstructure. Further FEA work is underway to better understand this interaction.

6.4 Effective Strain Hardening Coefficient

Mata provided a path to estimate the effective strain hardening that occurs as a result of irradiation exposure, through nano-indentation, when he developed his relationship for spherical approximations of pyramidal indents. This work is described in Section 2.3.5. Of particular importance is Equation 2.33, which relates the experimental parameters of uniaxial stress, contact radius, and probe geometry, to the calculated parameters of plastic zone depth, nano-hardness, and yield strain. Setting the measured depth of plastic deformation from Figure 5.10 equal to z_{ys}, defining the contact radius, a_s, as depicted in Figure 2.29 and measured off of Figure 4.6, and using of nano-

hardness, and nano-modulus measured through nano-indentation, allows for isolation of the effective strain hardening coefficient, n. The remaining variables are defined as using the following relationships: Tabor's relation between indentation stress and hardness, Equation 2.34, is used to determine σ_r, and Hooke's law where the yield stress is calculated from Equation 5.1. is used to determine yield strain. The values for calculation are summarized in Table 6.2, and lead to strain hardening values of 0.205, 0.305, and 0.340 for the as received, ion irradiated, and neutron irradiated conditions respectively.

These values shows strong agreement with the strain hardening values previously measured on ion irradiated ODS alloys via nano-indentation alone, where the as received condition produced an alloy with σ_{ys} = 1300 MPa, and n = 0.26. Ion irradiated alloys irradiated at 600° C to 100 dpa produced a yield strength of 1510 MPa and a strain hardening coefficient of 0.32, respectively [97].

True stress and true strain curves for each condition are presented in Figure 6.3, and are visual representations of the affect irradiation has on the 9wt%Cr-Fe ODS alloy examined in in this study. The damage cascade created during irradiation creates localized departure from chemical equilibrium, which in turn drives the development of a complex damage profile consisting of void and defect clusters, dislocation loops, and precipitates that arise from localized chemical segregation. While at low densities the creation of glissile voids and loops lower the energy required for plastic deformation by elevating the number of active slip planes, a large density of point defects, loops, and precipitates oppose plastic deformation by pinning mobile defects. As the microstructure evolves a balance is reached between the mobile and stationary defects that determines

the amount of irradiation induced strengthening a material undergoes. The equivalent strain hardening coefficient combines all of these hardening effects into one parameter and summarizes the changes in mechanical properties due to exposure to harsh reactor environments. Two recent studies provide a path to explain the effective strain hardening coefficients measured in this work.

Robertson investigated oxide stability by determining the effective strain hardening coefficients for multiple irradiation condition. In his discussion he developed an argument where oxide stability results in lower measures of work hardening due to the activation of multiple slip planes by dislocation debris forming from Orowan loops being required for the dislocations to overcome the oxides under strain. If the oxides dissolve there is less scattering of dislocations, which leads to plastic deformation being confined to a fewer number of slip planes that experience large pile-ups of dislocations, and increasing values of strain hardening [97]. Swenson determined, through atom probe tomography, that this neutron irradiated condition results in dissolution of the oxides in this exact ODS material. He also determined that the nature of the damage cascade plays a key role in the stability of the particles under irradiation [6].

Combining these two results explains why the effective strain hardening coefficients for the two irradiation conditions offers an difference of 10.9%, while there exists difference of 39.2% and 49.5% between the as received and the ion or neutron irradiated sample, respectively. The two irradiation conditions are similar enough that that produce similar defect microstructures that result in similar hardening, and it is proposed that the conditions both promote the dissolution of oxides that is associated with the increased effective strain hardening coefficients. The difference between the

two irradiated conditions is hypothesized to be a result from the slight differences in cascade formation between neutron and ion irradiations. Further study is required to confirm this theory.

6.5 Applicability of Tabor's approximation

The ability to accurately model pyramidal indentation requires understanding between the applied stress and the measured hardness. The applicability of Tabor's relation, Equation 2.34, has become to be questioned as the strain characteristics developed by Tabor have failed to describe some metals [102]. The agreement between the effective strain hardening coefficients measured in this work to those found in literature offers validation for the use of this relation in ODS alloys. This is thought to be attributed to the significant work hardening these materials experience during processing, and during exposure to irradiation environments.

Table 6.1: The defect densities and correlating diameters for the irradiation induced obstacles that contribute to the dispersed barrier hardening model for both the ion and neutron irradiated conditions, from data collected by Swenson using TEM and APT imaging.

	Ion Irradiated		Neutron Irradiated	
	Density (m^{-2})	Diameter (nm)	Density (m^{-2})	Diameter (nm)
Dislocation Lines	2.04×10^{15}	-	1.85×10^{15}	-
Carbides	1.7×10^{19}	90	4.7×10^{19}	100
Nano-Clusters	3.85×10^{23}	2.20	4.35×10^{23}	1.91
Voids	4.6×10^{20}	7.46	2.4×10^{20}	3.64
Dislocation Loops	3.1×10^{21}	21.5	27×10^{21}	9.5

Table 6.2: List of the variables used to solve Equation 2.30 for each irradiation condition.

	As Received	Ion Irradiated	Neutron Irradiated
H (GPa)	4.43	4.83	4.97
E(GPa)	218.46	193.60	223.01
σ_{ys} (MPa)	1382.3	1507.1	1550.75
ϵ_{ys} (%)	0.63	0.78	0.70
σ_r (MPa)	1642.2	1788.2	1840.7
z_{ys} (µm)	3.297	4.181	3.679
a_s (µm)	1.469	2.157	1.950
N	0.205	0.305	0.340
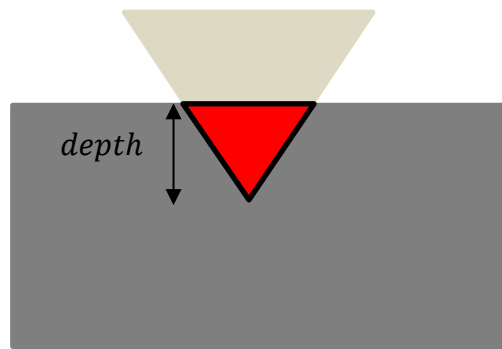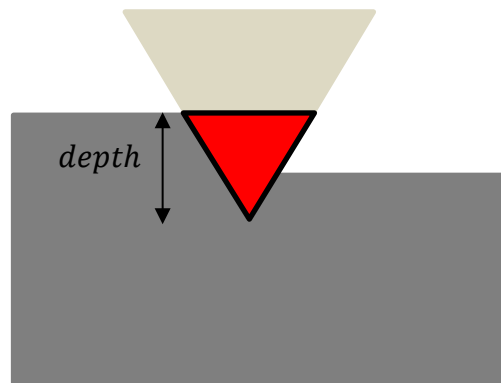
Figure 6.1: A diagram depicting the contact area for an area with a) low surface roughness, and b) high surface roughness. In both conditions the indenter contacts the surface and an indent of a certain depth from the initial surface is performed. In the case of low surface roughness the calculated contact area, the red region, matches the actual contact area of the probe. In the case of high surface roughness, the calculated contact area remains the same, but less of the probe is actually in contact with the sample. This lowers the nano-hardness in two ways: less load is required force to embed the probe into the sample, and over estimates the contact area for the hardness calculation.
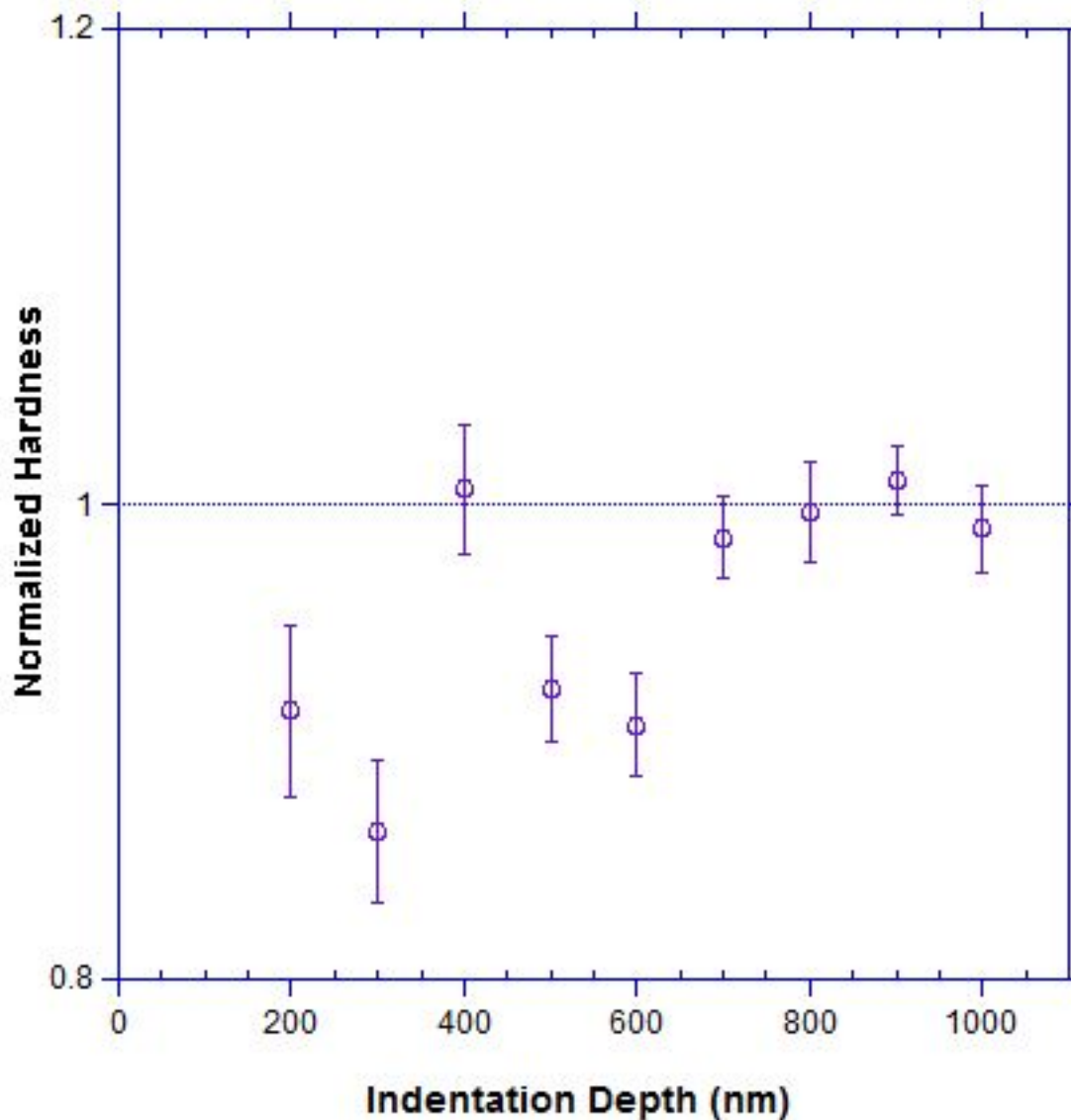
Figure 6.2: The ion irradiated nano-hardness normalized by the neutron irradiated nano-hardness. At indentation depths of 400 nm and of 700 nm and greater the normalized hardness approaches one, indicating depths where the surface and substrate effects are negligible.
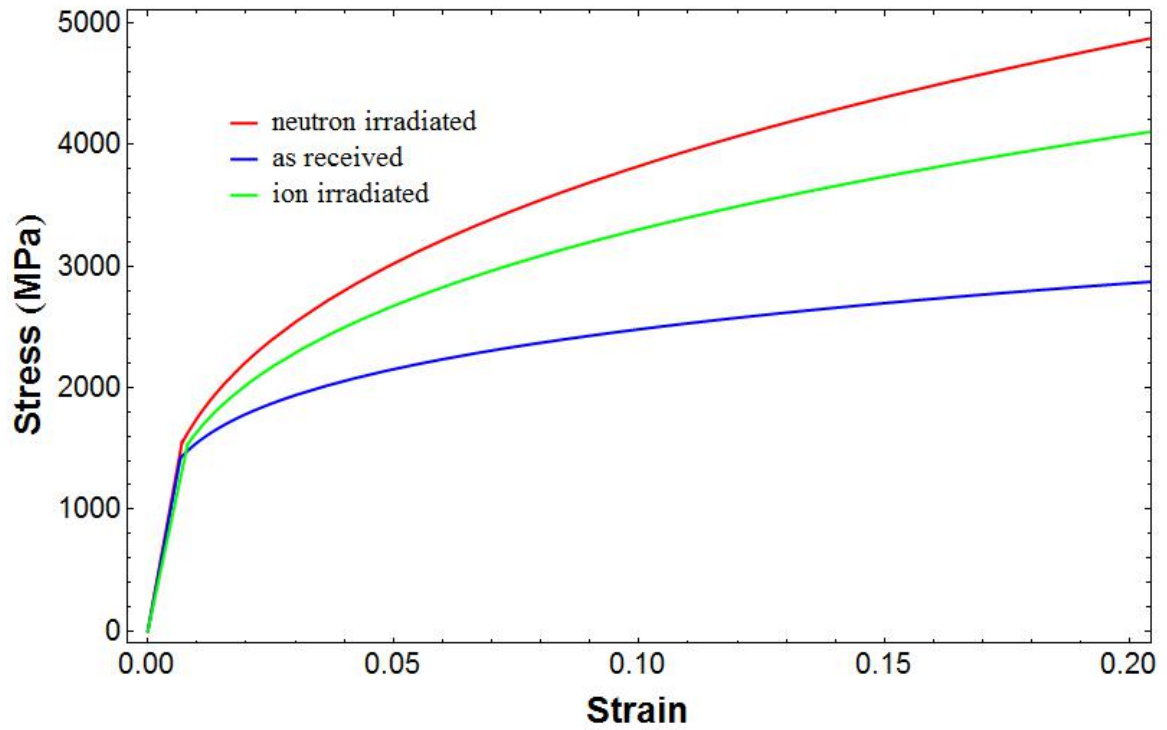
Figure 6.3: True stress and true strain curves developed from the parameters in Table 6.2 and average σ_{ys} of 1422.8, 1535.2, and 1541.4 MPa for the as received, ion irradiated, and neutron irradiated conditions, respectively.

CHAPTER SEVEN: CONCLUSIONS AND FUTURE WORK

The objective of this thesis was to quantify the extent of irradiation damage in a Fe-9wt%Cr ODS alloy through examination of its mechanical properties. Increases in nano-hardness were measured, and the equivalent strain hardening coefficients were calculated via the spherical indenter approximation. Increases in the effective strain hardening coefficient of 39.2% and 44.1% demonstrate the amount of work hardening that was done on the alloys during exposure to the respective ion and neutron fluxes, with the majority of the strengthening being attributed to the dissolution of the oxides back into the matrix.

It is worth noting that the method used in this work utilized Tabor's relationship to calculate the effective strain hardening coefficients under irradiation, which were found to have good agreement to those reported in literature through experimentation alone. This agreement provides insight into the applicability of Tabor's relationship in ODS alloys, and provides support for its use in modeling pyramidal indentation on this and similar materials.

When performed perpendicular to the incident surface, application of nano-indentation as a tool to measure irradiation induced hardening in ion irradiated samples was determined to be inadequate for indentations shallower than approximately 600 nm, due to the surface roughness. Indents between 700 nm and 1000nm in depth provided nano-hardness measurements consistent with those expected from microstructural characterization. This indicates that these depths are the target regions for performing top

down nano-indentation on ion irradiated materials. Indentation was not performed deep enough to determine when the bulk layer dominated nano-hardness measurements.

Measurement of the plastic zone on a nano-grained alloy was attempted via orientation mapping and bright field TEM imaging. No changes in preferred grain alignment was observed during orientation mapping, due to the heterogeneous distribution of grains prior to indentation. Defect contrast, and grain distortion provided insight into the extent of plastic deformation. The measurement technique was shown to provide plastic zone sizes consistent with Johnson's theory for elastic perfectly plastic materials, and those calculated through FEA.

Though the size of plastic deformation has been adequately characterized, the associated stress and strain fields have not been described. Future work into determining these parameters will provide a powerful tool that can be used to examine the ability of the nano-oxides and irradiation induced precipitates to obstruct dislocation motion based on composition, size, and coherency. Understanding this phenomenon will allow for accurate prediction of the induced hardening based on the evolution the microstructure. FEA has been shown to adequately model the stress strain relationship for nano-indentation and modeling work is currently underway.

REFERENCES

[1]   M. Roser, "World Population Growth," *OurWorldINData.org*, 2015. [Online].
       Available: http://ourworldindata.org/data/population-growth-vital-statistics/world-
       population-growth/. [Accessed: 28-Jul-2015].

[2]   K. L. Murty and I. Charit, "Structural materials for Gen-IV nuclear reactors:
       Challenges and opportunities," *J. Nucl. Mater.*, vol. 383, no. 1–2, pp. 189–195,
       2008.

[3]   R. L. Klueh and D. R. Harries, *High-Chromium Ferritic and Martensitic Steels for
       Nuclear Applications*. ASTM Int'l, 2011.

[4]   W. D. J. Callister and D. G. Rethwisch, *Materials Science and Engineering an
       Introduction*, 7th ed. John Wiley and Sons, Inc, 2007.

[5]   R. W. Hertzberg, R. P. Vinci, and J. L. Hertzberg, *Deformation and Fracture
       Mechanics of Engineering Materials*, 5th ed. John Wiley and Sons, Inc, 2013.

[6]   M. J. Swenson and J. P. Wharry, "The comparison of microstructure and
       nanocluster evolution in proton and neutron irradiated Fe-9%Cr ODs steel to 3 dpa
       at 500C," 2015.

[7]   J. Hollomon, "Tensile Deformation," *Trans. Am. Inst. Min. Metall. Eng.*, vol. 162,
       pp. 268–290, 1945.

[8]   A. Bowen and P. Partridge, "Limitations of the Hollomon strain-hardening
       equationt," *J. Appl. Phys.*, vol. 7, pp. 969–978, 1974.

[9]   T. Tanno, S. Ohtsuka, Y. Yano, T. Kaito, Y. Oba, M. Ohnuma, S. Koyama, and K.
       Tanaka, "Evaluation of mechanical properties and nano-meso structures of 9–
       11%Cr ODS steels," *J. Nucl. Mater.*, vol. 440, no. 1–3, pp. 568–574, Sep. 2013.

[10]   K. Hashimoto, M. Yamanaka, Y. Otogura, T. Zaizen, M. Onoyama, and T. Fujita, "Newly Developed 9Cr-2Mo-Nb-V(NSCR9) Steel," in *Ferritic Alloys for use in Nuclear Energy Technologies*, 1983, p. 307.

[11]   F. Abe, H. Araki, and T. Noda, "The Effect of Tungsten on Dislocation Recovery and Precipitation Behavior of Low-Activation Martensitic 9Cr Steels," *Metall. Trans. A*, vol. 22A, p. 2225, 1991.

[12]   S. Shikakura, S. Nomura, S. Ukai, I. Seshimo, Y. Kano, Y. Kuwajima, T. Ito, K. Tataki, and T. Fujita, "Development of High-Strength Ferritic/Martensitic Steel for FBR Core Materials," *J. At. Energy Soc. Japan*, vol. 33, p. 1157, 1991.

[13]   S. H. Kim, W. S. Ryu, and I. Kuk, Hiun, "Microstructure and Mechanical Properties of Cr-Mo Steels for Nuclear Industry Applications," *J. Korean Nucl. Soc.*, vol. 31, no. 6, pp. 561–571, 1999.

[14]   R. L. Klueh, N. Hashimoto, M. . Sokolov, K. Shiba, and S. Jitsukawa, "Mechanical properties of neutron-irradiated nickel-containing martensitic steels: I. Experimental study," *J. Nucl. Mater.*, vol. 357, pp. 156–168, Oct. 2006.

[15]   Y. Li, T. Nagasaka, T. Muroga, A. Kimura, and S. Ukai, "High-temperature mechanical properties and microstructure of 9Cr oxide dispersion strengthened steel compared with RAFMs," *Fusion Eng. Des.*, vol. 86, no. 9–11, pp. 2495–2499, Oct. 2011.

[16]   T. S. Byun, J. H. Yoon, D. T. Hoelzer, Y. B. Lee, S. H. Kang, and S. A. Maloy, "Process development for 9Cr nanostructured ferritic alloy (NFA) with high fracture toughness," *J. Nucl. Mater.*, vol. 449, no. 1–3, pp. 290–299, Jun. 2014.

[17]   Z. Oksiuta, P. Hosemann, S. C. Vogel, and N. Baluc, "Microstructure examination of Fe – 14Cr ODS ferritic steels produced through different processing routes," *J. Nucl. Mater.*, vol. 451, no. 1–3, pp. 320–327, 2014.

[18]   M. A. Auger, V. de Castro, T. Leguey, M. A. Monge, A. Muñoz, and R. Pareja, "Microstructure and tensile properties of oxide dispersion strengthened Fe–14Cr–0.3Y2O3 and Fe–14Cr–2W–0.3Ti–0.3Y2O3," *J. Nucl. Mater.*, vol. 442, no. 1–3, pp. S142–S147, Nov. 2013.

[19]   T. Muroga, T. Nagasaka, Y. Li, H. Abe, S. Ukai, A. Kimura, and T. Okuda, "Fabrication and characterization of reference 9Cr and 12Cr-ODS low activation

ferritic/martensitic steels," *Fusion Eng. Des.*, vol. 89, no. 7–8, pp. 1717–1722, Oct. 2014.

[20]   S. Ukai, S. Mizuta, M. Fujiwara, T. Okuda, and T. Kobayashi, "Development of 9Cr-ODS Martensitic Steel Claddings for Fuel Pins by means of Ferrite to Austenite Phase Transformation," *J. Nucl. Sci. Technol.*, vol. 39, no. 7, pp. 778–788, Jul. 2002.

[21]   H. Sakasegawa, L. Chaffron, F. Legendre, L. Boulanger, T. Cozzika, M. Brocq, and Y. de Carlan, "Correlation between chemical composition and size of very small oxide particles in the MA957 ODS ferritic alloy," *J. Nucl. Mater.*, vol. 384, no. 2, pp. 115–118, Feb. 2009.

[22]   L. Toualbi, C. Cayron, P. Olier, J. Malaplate, M. Praud, M.-H. Mathon, D. Bossu, E. Rouesne, A. Montani, R. Logé, and Y. de Carlan, "Assessment of a new fabrication route for Fe–9Cr–1W ODS cladding tubes," *J. Nucl. Mater.*, vol. 428, no. 1–3, pp. 47–53, Sep. 2012.

[23]   L. Toualbi, C. Cayron, P. Olier, R. Logé, and Y. de Carlan, "Relationships between mechanical behavior and microstructural evolutions in Fe 9Cr–ODS during the fabrication route of SFR cladding tubes," *J. Nucl. Mater.*, vol. 442, no. 1–3, pp. 410–416, Nov. 2013.

[24]   G. S. Was, *Fundamentals of Radiation Materials Science: Metals and Alloys*, 1st ed. Springer-Verlag Berlin Heidelberg, 2007.

[25]   D. A. Terentyev, L. Malerba, R. Chakarova, K. Nordlund, P. Olsson, M. Rieth, and J. Wallenius, "Displacement cascades in Fe-Cr: A molecular dynamics study," *J. Nucl. Mater.*, vol. 349, no. 1–2, pp. 119–132, 2006.

[26]   L. K. Mansur, "Theory and experimental background on dimensional changes in irradiated alloys," *J. Nucl. Mater.*, vol. 216, no. 1994, pp. 97–123, 1994.

[27]   T. R. Allen, "On the mechanism of radiation-induced segregation in austenitic Fe – Cr – Ni alloys," *J. Nucl. Mater.*, vol. 255, pp. 44–58, 1998.

[28]   T. R. Allen and G. S. Was, "Modeling Radiation Induced Segregation in Austenitic Fe-Cr-Ni Alloys," *Acta Mater.*, vol. 46, no. 10, pp. 3679–3691, 1998.

[29]   A. D. Marwick, "Segregation in irradiated alloys: The inverse Kirkendall effect and the effect of constitution on void swelling," *J. Phys. F Met. Phys.*, vol. 8, no. 9, pp. 1849–1861, 2001.

[30]   Z. Lu, R. G. Faulkner, G. Was, and B. D. Wirth, "Irradiation-induced grain boundary chromium microchemistry in high alloy ferritic steels," *Scr. Mater.*, vol. 58, no. 10, pp. 878–881, May 2008.

[31]   G. Gupta, Z. Jiao, A. N. Ham, J. T. Busby, and G. S. Was, "Microstructural evolution of proton irradiated T91," *J. Nucl. Mater.*, vol. 351, pp. 162–173, Jun. 2006.

[32]   J. P. Wharry and G. S. Was, "A systematic study of radiation-induced segregation in ferritic–martensitic alloys," *J. Nucl. Mater.*, vol. 442, no. 1–3, pp. 7–16, Nov. 2013.

[33]   R. E. Clausing, L. Heatherly, R. G. Faulkner, A. F. Rowcliffe, and K. Farrell, "Radiation-Induced Segregation in HT-9 Martensitic Steel," *J. Nucl. Mater.*, no. 141–143, pp. 978–981, 1986.

[34]   R. G. Faulkner, E. A. Little, and T. S. Morgan, "Irradiation-induced grain and lath boundary segregation in ferritic-martensitic steels," *J. Nucl. Mater.*, no. 191–194, pp. 858–861, 1992.

[35]   Y. Hamaguchi, H. Kuwano, H. Kamide, R. Miura, and T. Yamada, "Effects of proton irradiation on the hardening behavior of HT-9 steel," *J. Nucl. Mater.*, vol. 133–134, pp. 636–639, 1985.

[36]   S. Ohnuki, H. Takahashi, and T. Takeyama, "Void Swelling and Segregation of Solute in Ion-Irradiated Ferritic Steels," *J. Nucl. Mater.*, no. 103–104, pp. 1121–1126, 1981.

[37]   E. A. Marquis, S. Lozano-Perez, and V. De Castro, "Effects of heavy-ion irradiation on the grain boundary chemistry of an oxide-dispersion strengthened Fe–12wt.% Cr alloy," *J. Nucl. Mater.*, vol. 417, no. 1–3, pp. 257–261, Oct. 2011.

[38]   I. M. Neklyudov and V. N. Voyevodin, "Features of structure-phase transformations and segregation processes under irradiation of austenitic and ferritic-martensitic steels," *J. Nucl. Mater.*, vol. 212–215, pp. 39–44, Sep. 1994.

[39]   R. Schäublin, P. Spätig, and M. Victoria, "Chemical segregation behavior of the low activation ferritic/martensitic steel F82H," *J. Nucl. Mater.*, vol. 258–263, pp. 1350–1355, 1998.

[40]   T. R. Allen, D. Kaoumi, J. P. Wharry, Z. Jiao, C. Topbasi, A. Kohnert, L. M. Barnard, A. G. Certain, K. G. Field, G. S. Was, D. Morgan, A. T. Motta, B. D. Wirth, and Y. Yang, "Characterizatin of Microstructue and Property Evolution in Advanced Cladding and Duct: Materials Exposed to High Dose and Elevated Temperature," *J. Mater. Res.*, vol. 30, no. 9, pp. 1246–1274, 2015.

[41]   S. Choudhury, L. Barnard, J. D. Tucker, T. R. Allen, B. D. Wirth, M. Asta, and D. Morgan, "Ab-initio based modeling of diffusion in dilute bcc Fe–Ni and Fe–Cr alloys and implications for radiation induced segregation," *J. Nucl. Mater.*, vol. 411, pp. 1–14, Apr. 2011.

[42]   P. Olsson, "Ab initio study of interstitial migration in Fe-Cr alloys," *J. Nucl. Mater.*, vol. 386–388, no. C, pp. 86–89, 2009.

[43]   K. L. Wong, H. J. Lee, J. H. Shim, B. Sadigh, and B. D. Wirth, "Multiscale modeling of point defect interactions in Fe-Cr alloys," *J. Nucl. Mater.*, vol. 386–388, no. C, pp. 227–230, 2009.

[44]   J. P. Wharry and G. S. Was, "The mechanism of radiation-induced segregation in ferritic–martensitic alloys," *Acta Mater.*, vol. 65, pp. 42–55, Feb. 2014.

[45]   Z. Lu, R. G. Faulkner, N. Sakaguchi, H. Kinoshita, H. Takahashi, and P. E. J. Flewitt, "Effect of hafnium on radiation-induced inter-granular segregation in ferritic steel," *J. Nucl. Mater.*, vol. 351, no. 1–3, pp. 155–161, Jun. 2006.

[46]   K. G. Field, L. M. Barnard, C. M. Parish, J. T. Busby, D. Morgan, and T. R. Allen, "Dependence on grain boundary structure of radiation induced segregation in a 9 wt .% Cr model ferritic / martensitic steel," vol. 435, pp. 172–180, 2013.

[47]   R. Hu, G. D. W. Smith, and E. A. Marquis, "Effect of grain boundary orientation on radiation-induced segregation in a Fe-15.2 at.% Cr alloy," *Acta Mater.*, vol. 61, no. 9, pp. 3490–3498, 2013.

[48]   C. C. Wei, A. Aitkaliyeva, M. S. Martin, D. Chen, and L. Shao, "Microstructural changes of T-91 alloy irradiated by Fe self ions to ultrahigh displacement ratios," *Nucl. Instruments Methods Phys. Res. Sect. B Beam Interact. with Mater. Atoms*,

vol. 307, pp. 181–184, 2013.

[49]   W. Chen, Y. Miao, Y. Wu, C. A. Tomchik, K. Mo, J. Gan, M. A. Okuniewski, S. A. Maloy, and J. F. Stubbins, "Atom probe study of irradiation-enhanced α′ precipitation in neutron-irradiated Fe–Cr model alloys," *J. Nucl. Mater.*, vol. 462, pp. 242–249, Jul. 2015.

[50]   V. Kuksenko, C. Pareige, and P. Pareige, "Cr precipitation in neutron irradiated industrial purity Fe–Cr model alloys," *J. Nucl. Mater.*, vol. 432, no. 1–3, pp. 160–165, Jan. 2013.

[51]   V. Kuksenko, C. Pareige, and P. Pareige, "Intra granular precipitation and grain boundary segregation under neutron irradiation in a low purity Fe–Cr based alloy," *J. Nucl. Mater.*, vol. 425, pp. 125–129, Jun. 2012.

[52]   E. A. Little, T. S. Morgan, and R. G. Faulkner, "Microchemistry of Neutron Irradiated 12%CrMoVNb Martensitic Steel," *Mater. Sci. Forum*, vol. 97–99, pp. 323–328, 1992.

[53]   Y. N. Osetsky, A. Serra, B. N. Singh, "Structure and properties of clusters of self-interstitial atoms in fcc copper and bcc iron," *Philos. Mag. A*, vol. 80, no. 9, pp. 2131–2157, 2000.

[54]   B. D. Wirth, G. R. Odette, D. Maroudas, and G. E. Lucas, "Dislocation loop structure, energy and mobility of self-interstitial atom clusters in bcc iron," *J. Nucl. Mater.*, vol. 276, no. 1, pp. 33–40, 2000.

[55]   S. L. Dudarev, K. Arakawa, X. Yi, Z. Yao, M. L. Jenkins, M. R. Gilbert, and P. M. Derlet, "Spatial ordering of nano-dislocation loops in ion-irradiated materials," *J. Nucl. Mater.*, vol. 455, no. 1–3, pp. 16–20, 2014.

[56]   Y. Huang, J. P. Wharry, Z. Jiao, C. M. Parish, S. Ukai, and T. R. Allen, "Microstructural evolution in proton irradiated NF616 at 773K to 3dpa," *J. Nucl. Mater.*, vol. 442, no. 1–3, pp. S800–4, 2013.

[57]   A. A. Semenov and C. H. Woo, "Theory of Frank loop nucleation at elevated temperatures," *Philos. Mag.*, vol. 83, no. 31–34, pp. 3765–3782, 2003.

[58]   B. Yao, D. J. Edwards, and R. J. Kurtz, "TEM characterization of dislocation loops

in irradiated bcc Fe-based steels," *J. Nucl. Mater.*, vol. 434, no. 1–3, pp. 402–410, Mar. 2013.

[59] J. Chen, P. Jung, W. Hoffelner, and H. Ullmaier, "Dislocation loops and bubbles in oxide dispersion strengthened ferritic steel after helium implantation under stress," *Acta Mater.*, vol. 56, no. 2, pp. 250–258, 2008.

[60] D. S. Gelles, "Microstructural examination of commercial ferritic alloys at 200 dpa," *J. Nucl. Mater.*, vol. 233–237, no. PART 1, pp. 293–298, 1996.

[61] D. S. Gelles, S. Ohnuki, H. Takahashi, H. Matsui, and Y. Kohno, "Electron irradiatin experiments in support of fusion materials development," *Jounal Nucl. Mater.*, vol. 191–194, pp. 1336–1341, 1992.

[62] J. Marian, B. D. Wirth, and J. M. Perlado, "Mechanism of formation and growth of <100> interstitial loops in ferritic materials.," *Phys. Rev. Lett.*, vol. 88, no. 25 Pt 1, p. 255507, 2002.

[63] R. Bullough and R. C. Perrin, "The Morphology of Interstitial Aggregates in Iron," *Proc. R. Soc. A Math. Phys. Eng. Sci.*, vol. 305, no. 1483, pp. 541–552, 1968.

[64] J. Marian, B. D. Wirth, R. Schäublin, J. M. Perlado, and T. Díaz de la Rubia, "<100>-Loop characterization in α-Fe: comparison between experiments and modeling," *J. Nucl. Mater.*, vol. 307–311, pp. 871–875, 2002.

[65] D. Terentyev, G. Bonny, C. Domain, G. Monnet, and L. Malerba, "Mechanisms of radiation strengthening in Fe-Cr alloys as revealed by atomistic studies," *J. Nucl. Mater.*, vol. 442, no. 1–3, pp. 470–485, 2013.

[66] E. A. Little and D. A. Stow, "Void-Swelling in Irons and Ferritic Steels," *J. Nucl. Mater.*, vol. 87, pp. 25–39, 1979.

[67] P. Pareige, M. K. Miller, R. E. Stoller, D. T. Hoelzer, E. Cadel, and B. Radiguet, "Stability of nanometer-sized oxide clusters in mechanically-alloyed steel under ion-induced displacement cascade damage conditions," *J. Nucl. Mater.*, vol. 360, no. 2, pp. 136–142, 2007.

[68] A. G. Certain, S. Kuchibhatla, V. Shutthanandan, D. T. Hoelzer, and T. R. Allen, "Radiation stability of nanoclusters in nano-structured oxide dispersion

strengthened (ODS) steels," *J. Nucl. Mater.*, vol. 434, no. 1–3, pp. 311–321, 2013.

[69] I. Monnet, P. Dubuisson, Y. Serruys, M. O. Ruault, O. Kaïtasov, and B. Jouffrey, "Microstructural investigation of the stability under irradiation of oxide dispersion strengthened ferritic steels," *J. Nucl. Mater.*, vol. 335, no. 3, pp. 311–321, 2004.

[70] T. R. Allen, J. Gan, J. I. Cole, M. K. Miller, J. T. Busby, S. Shutthanandan, and S. Thevuthasan, "Radiation response of a 9 chromium oxide dispersion strengthened steel to heavy ion irradiation," *J. Nucl. Mater.*, vol. 375, no. 1, pp. 26–37, Mar. 2008.

[71] M. L. Lescoat, J. Ribis, a. Gentils, O. Kaïtasov, Y. De Carlan, and a. Legris, "In situ TEM study of the stability of nano-oxides in ODS steels under ion-irradiation," *J. Nucl. Mater.*, vol. 428, no. 1–3, pp. 176–182, 2012.

[72] M. L. Lescoat, J. Ribis, Y. Chen, E. A. Marquis, E. Bordas, P. Trocellier, Y. Serruys, A. Gentils, O. Kaïtasov, Y. de Carlan, and A. Legris, "Radiation-induced Ostwald ripening in oxide dispersion strengthened ferritic steels irradiated at high ion dose," *Acta Mater.*, vol. 78, pp. 328–340, 2014.

[73] A. G. Certain, K. G. Field, T. R. Allen, M. K. Miller, J. Bentley, and J. T. Busby, "Response of nanoclusters in a 9Cr ODS steel to 1dpa, 525°C proton irradiation," *J. Nucl. Mater.*, vol. 407, no. 1, pp. 2–9, Dec. 2010.

[74] H. Kishimoto, K. Yutani, R. Kasada, O. Hashitomi, and a. Kimura, "Heavy-ion irradiation effects on the morphology of complex oxide particles in oxide dispersion strengthened ferritic steels," *J. Nucl. Mater.*, vol. 367–370 A, no. SPEC. ISS., pp. 179–184, 2007.

[75] H. Kishimoto, R. Kasada, O. Hashitomi, and a. Kimura, "Stability of Y-Ti complex oxides in Fe-16Cr-0.1Ti ODS ferritic steel before and after heavy-ion irradiation," *J. Nucl. Mater.*, vol. 386–388, no. C, pp. 533–536, 2009.

[76] A. G. Certain, H. J. Lee Voigt, T. R. Allen, and B. D. Wirth, "Investigation of cascade-induced re-solution from nanometer sized coherent precipitates in dilute Fe-Cu alloys," *J. Nucl. Mater.*, vol. 432, no. 1–3, pp. 281–286, 2013.

[77] "Iron-Chromium (Fe0Cr) Phase Diagram," *Computational Thermodynamics INc*, 2011. [Online]. Available: http://www.calphad.com/iron-chromium.html.

[78] T. R. Allen, L. Tan, J. Gan, G. Gupta, G. S. Was, E. A. Kenik, S. Shutthanandan, and S. Thevuthasan, "Microstructural development in advanced ferritic-martensitic steel HCM12A," *Jounal Nucl. Mater.*, vol. 351, pp. 174–186, 2006.

[79] E. Materna-Morris, A. Möslang, and H.-C. Schneider, "Tensile and low cycle fatigue properties of EUROFER97-steel after 16.3dpa neutron irradiation at 523, 623 and 723K," *J. Nucl. Mater.*, vol. 442, no. 1–3, pp. S62–S66, 2013.

[80] J. L. Seran, A. Alamo, A. Maillard, H. Touron, J. C. Brachet, P. Dubuisson, and O. Rabouille, "Pre and post irradiation mechanical properties of ferritic-martensitic steels for fusion applications: EM10 base metal amd EM10/EM10 wleds," *Jounal Nucl. Mater.*, vol. 212–215, pp. 588–593, 1994.

[81] T. Kuwabara, H. Kurishita, S. Ukai, M. Narui, S. Mizuta, M. Yamazaki, and H. Kayano, "Superior Charpy impact properties of ODS ferritic steel irradiated in JOYO," *J. Nucl. Mater.*, vol. 258–263, pp. 1236–1241, 1998.

[82] M. Song, Y. D. Wu, D. Chen, X. M. Wang, C. Sun, Y. Chen, L. Shao, Y. Yang, K. T. Hartwig, and X. Zhang, "Response of equal channel angular extrusin precessed ultrafine-grained T91 steel subjected to high temperature heavy ion irradiation," *Acta Mater.*, vol. 74, pp. 285–295, 2014.

[83] *TI 950 TriboIndenter User Manual*, 9.3.0314 ed. Hysitron, 2014.

[84] P. Hosemann, D. Kiener, Y. Wang, and S. a. Maloy, "Issues to consider using nano indentation on shallow ion beam irradiated materials," *J. Nucl. Mater.*, vol. 425, no. 1–3, pp. 136–139, Jun. 2012.

[85] A. C. Fischer-Cripps, "Critical review of analysis and interpretation of nanoindentation test data," *Surf. Coatings Technol.*, vol. 200, no. 14–15, pp. 4153–4165, Apr. 2006.

[86] "Standard Practice for Insturmented Indentation Testing," *ASTM Standard E2546*. ASTM Int'l, 2007.

[87] "How to Select the Correct Indenter Tip," Agilent Technologies, 2009.

[88] E. S. Berkovich, "Three-Faceted Daimond Pyramid for Micro-Hardness Testing," *Ind. Diam. Rev.*, vol. 11, no. 127, pp. 129–131, 1951.

[89] W. C. Oliver and G. M. Pharr, "An improved technique for determining hardness and elastic modulus using load and displacement sensing indentation experiments," *Mater. Res. Soc.*, vol. 7, no. 6, pp. 1564–1583, 1992.

[90] A. C. Fischer-Cripps, *Introduction to Contact Mechanics*, 2nd ed. New York: Springer Science+Business Media, LLC, 2007.

[91] A. C. Fischer-Cripps, "A review of analysis methods for sub-micron indentation testing," *Vacuum*, vol. 58, no. 4, pp. 569–585, 2000.

[92] R. Hill, *The Mathematical Theory of Plasticity*. Oxford: Oxford University Press, 1950.

[93] E. H. Yoffe, "Elastic stress fields caused by indenting brittle materials," *Philosocphical Mag. A*, vol. 46, no. 4, pp. 617–628, 1982.

[94] M. Mata, O. Casals, and J. Alcalá, "The plastic zone size in indentation experiments: The analogy with the expansion of a spherical cavity," *Int. J. Solids Struct.*, vol. 43, no. 20, pp. 5994–6013, Oct. 2006.

[95] J. Lubliner, *Plasticity Theory*. New York: Macmillan Publishing Company, 1990.

[96] K. L. Johnson, *Contact Mechanics*. Cambridge, UK: Cambridge University Press, 1985.

[97] C. Robertson, B. K. Panigrahi, S. Kataria, Y. Serruys, M. H. Mathon, and C. S. Sundar, "Particle stability in model ODS steels irradiated up to 100 dpa at 600C: TEM and nano-indentatin investigation," *J. Nucl. Mater.*, vol. 426, pp. 240–246, 2012.

[98] D. E. Kramer, H. Huang, M. Kriese, J. Robach, J. Nelson, A. Wright, D. Bahr, and W. W. Gerberich, "Yield strength predictions from the plastic zone around nanocontacts," *Acta Mater.*, vol. 47, no. 1, pp. 333–343, 1998.

[99] W. Zielinski, H. Huang, and W. W. Gerberich, "Microscopy and microindentation mechanics of single crystal Fe−3 wt. % Si: Part II. TEM of the indentation plastic zone," *J. Mater. Res.*, vol. 8, no. 06, pp. 1300–1310, 1993.

[100] M. Mata, M. Anglada, and J. Alcalá, "Contact Deformation Regimes Around Sharp Indentations and the Concept of the Characteristic Strain," *J. Mater. Res.*, vol. 17, no. 05, pp. 964–976, 2002.

[101] M. Mata and J. Alcalá, "Mechanical property evaluation through sharp indentations in elastoplastic and fully plastic contact regimes," *J. Mater. Res.*, vol. 18, no. 07, pp. 1705–1709, 2003.

[102] J. L. Bucaille, S. Stauss, E. Felder, and J. Michler, "Determination of plastic properties of metals by instrumented indentation using different sharp indenters," *Acta Mater.*, vol. 51, no. 6, pp. 1663–1678, 2003.

[103] M. Dao, N. Chollacoop, K. J. Van Vliet, T. A. Venkatesh, and S. Suresh, "Computational modeling of the forward and reverse problems," *instrumented sharp indentation, Acta Mater.*, vol. 49, pp. 3899–3918, 2001.

[104] D. E. Kramer, M. F. Savage, A. Lin, and T. Foecke, "Novel method for TEM characterization of deformation under nanoindents in nanolayered materials," *Scr. Mater.*, vol. 50, no. 6, pp. 745–749, 2004.

[105] C. Robertson and M. C. Fivel, "A study of the submicron indent-induced plastic deformation," *J. Mater. Res.*, vol. 14, no. 6, pp. 2251–2258, 1996.

[106] W. Zielinski, H. Huang, S. Venkataraman, and W. W. Gerberich, "Dislocation distribution under a microindentation into an iron silicon single crystal," *Philos. Mag. A*, vol. 72, no. 5, pp. 1221–1237, 1995.

[107] M. Rester, C. Motz, and R. Pippan, "The deformation-induced zone below large and shallow nanoindentations: A comparative study using EBSD and TEM," *Philos. Mag. Lett.*, vol. 88, no. 12, pp. 879–887, 2008.

[108] K. A. Nibur and D. F. Bahr, "Identifying slip systems around indentations in FCC metals," *Scr. Mater.*, vol. 49, no. 11, pp. 1055–1060, 2003.

[109] D. Kiener, R. Pippan, C. Motz, and H. Kreuzer, "Microstructural evolution of the deformed volume beneath microindents in tungsten and copper," *Acta Mater.*, vol. 54, no. 10, pp. 2801–2811, 2006.

[110] B. Bose and R. J. Klassen, "Effect of ion irradiation and indentation depth on the

kinetics of deformation during micro-indentation of Zr-2.5%Nb pressure tube material at 25 ??C," *J. Nucl. Mater.*, vol. 399, no. 1, pp. 32–37, 2010.

[111] S. S. Chiang, D. B. Marshall, and A. G. Evans, "The response fo solids to elastic/plastic indentation. I. Stresses adn residual stresses," *J. Appl. Phys.*, vol. 53, no. 1, pp. 298–311, 1982.

[112] K. S. Chen, T. C. Chen, and K. S. Ou, "Development of semi-empirical formulation for extracting materials properties from nanoindentation measurements: Residual stresses, substrate effect, and creep," *Thin Solid Films*, vol. 516, no. 8, pp. 1931–1940, 2008.

[113] Y.-T. Cheng and C.-M. Cheng, "Scaling Relationships in Conical Indentation in Elastic-Plastic Solids with Work-Hardening," *J. Appl. Phys.*, vol. 84, no. 3, pp. 1284–1291, 1998.

[114] Z. Hu, K. J. Lynne, S. P. Markondapatnaikuni, and F. Delfanian, "Material elastic-plastic property characterization by nanoindentation testing coupled with computer modeling," *Mater. Sci. Eng. A*, vol. 587, pp. 268–282, 2013.

[115] W. D. Nix and H. Gao, "Indentation size effects in crystalline materials: A law for strain gradient plasticity," *J. Mech. Pysics Solids*, vol. 46, no. 3, pp. 411–425, 1998.

[116] C. L. Chen, A. Richter, R. Kögler, and G. Talut, "Dual beam irradiation of nanostructured FeCrAl oxide dispersion strengthened steel," *J. Nucl. Mater.*, vol. 412, no. 3, pp. 350–358, 2011.

[117] H. Gao and Y. Huang, "Geometrically necessary dislocation and size-dependent plasticity," *Scr. Mater.*, vol. 48, no. 2, pp. 113–118, 2003.

[118] "Metastable Iron Carbon (Fe-C) Phase Diagram," *Calphad*, 2006. [Online]. Available: http://www.calphad.com/iron-carbon.html.

[119] K. Ballentine, "Examples of Iron-Iron Carbide Phase Trasformations on the T-T-T Diagram," 1996. [Online]. Available: http://www.sv.vt.edu/classes/MSE2094_NoteBook/96ClassProj/examples/kimttt.html.

[120] G. Marshall, P. Evans, and A. Green, "Aluminium Alloys: Strengthening," *University of Liverpool*, 2000. [Online]. Available: http://www.matter.org.uk/matscicdrom/manual/as.html. [Accessed: 04-Feb-2014].

[121] "Linear Defects: Dislocations." [Online]. Available: http://www.ndt-ed.org/EducationResources/CommunityCollege/Materials/Structure/linear_defects.htm.

[122] A. Beaber and W. Gerberich, "Alloys: Strength from Modellling," *Nature Materials*, 2010. [Online]. Available: http://www.nature.com/nmat/journal/v9/n9/full/nmat2840.html. [Accessed: 04-Feb-2014].

[123] R. R. Ambriz and D. Jaramillo, "Precipitation adn mechanical properties of aluminum alloys," in *Mechanical Behavior of Precipitation Hardened Aluminum Alloys Welds, Light Metal Alloys Applications*, Intech, 2014.

[124] H. Helong, Z. Zhangjian, L. Lu, W. Man, and L. Shaofu, "Fabrication and Mechanical Properties of a 14 Cr-ODS steel," *J. Phys.*, vol. 419, 2013.

[125] K. Knowles, D. Holmes, A. Bridges, and H. Scott, "Slip in Single Crystals," *University of Cambridge*. [Online]. Available: http://www.doitpoms.ac.uk/tlplib/slip/printall.php. [Accessed: 04-Sep-2014].

[126] F. Masuyama, *Advanced Heat Resistant Steels for Power Generation*. London, 1999.

[127] C. Race, *The Modelling of Radiation Damage in Metals Using Ehrenfest Dynamics*, 2011th ed. Berlin, Heidelberg: Springer Berlin Heidelberg, 2010.

[128] S. Ohtsuka, S. Ukai, M. Fujiwara, T. Kaito, and T. Narita, "Improvement of Creep Strength of 9CrODS Martensitic Steel by Controlling Excess Oxygen and Titanium Concentrations," *Mater. Trans.*, vol. 46, no. 3, pp. 487–492, 2005.

[129] S. Ohtsuka, "Lot M16 9 Cr ODS Chemical Composition," 2004.

[130] J. P. Wharry, "The mechanism of radiation-induced segregation in ferritic-martensitic steels," University of Michigan, 2012.

[131] R. E. Stoller, M. B. Toloczko, G. S. Was, A. G. Certain, S. Dwaraknath, and F. A. Garner, "On the use of SRIM for computing radiation damage exposure," *Nucl. Instruments Methods Phys. Res. Sect. B Beam Interact. with Mater. Atoms*, vol. 310, pp. 75–80, 2013.

[132] T. R. Allen, M. C. Thelen, and J. Ulrich, "ATR National Scientific User Facility," 2012.

[133] M. F. Triola, *Essentials of Statistics*, Third. Boston: Pearson Education, 2008.

[134] E. F. Rauch and M. Véron, "Automated Crystal Orientation and Phase Mapping in TEM," *Mater. Charact.*, vol. 98, pp. 1–9, 2014.

[135] "Automatic Tem Orientation/Phase Mapping Precession Mapping: How it Works." Nano-Megas.

[136] Z. Huang, A. Harris, S. A. Maloy, and P. Hosemann, "Nanoindentation creep study on an ion beam irradiated oxide dispersion strengthened alloy," *J. Nucl. Mater.*, vol. 451, no. 1–3, pp. 162–167, 2014.

[137] P. Hosemann, E. Stergar, L. Peng, Y. Dai, S. A. Maloy, M. A. Pouchon, K. Shiba, D. Hamaguchi, and H. Leitner, "Macro and microscale mechanical testing and local electrode atom probe measurements of STIP irradiated F82H, Fe-8Cr ODS and Fe-8Cr-2W ODS," *J. Nucl. Mater.*, vol. 417, no. 1–3, pp. 274–278, 2011.

[138] X. Jia and Y. Dai, "Microstructure of the F82H martensitic steel irradiated in STIP-II up to 20 dpa," *J. Nucl. Mater.*, vol. 356, no. 1–3, pp. 105–111, 2006.

[139] C. Robertson, S. Poissonnet, and L. Boulanger, "Plasticity in ion-irradiated austenitic stainless steels," *J. Mater. Res.*, vol. 13, no. 8, pp. 2123–2131, 1997.

[140] M. Yoshioka, "Plastically deformed region around indentations on Si single crystal," *J. Appl. Phys.*, vol. 76, no. 12, pp. 7790–7796, 1994.

[141] Y. J. Wei and L. Anand, "Grain-boundary sliding and separation in polycrystalline metals: Application to nanocrystalline fcc metals," *J. Mech. Phys. Solids*, vol. 52, no. 11, pp. 2587–2616, 2004.

[142] S. H. Chen, L. Liu, and T. C. Wang, "Small scale, grain size and substrate effects

in nano-indentation experiment of film-substrate systems," *Int. J. Solids Struct.*, vol. 44, no. 13, pp. 4492–4504, 2007.